Localization, Disorder, and Polarization Fields in Wide-Gap Semiconductor Quantum Wells

DISSERTATION

zur Erlangung des akademischen Grades
doctor rerum naturalium
(dr. rer. nat.)
im Fach Physik

eingereicht an der
Mathematisch-Naturwissenschaftlichen Fakultät I
Humboldt-Universität zu Berlin

von
Herrn Oliver Mayrock
geboren am 2.9.1970 in Regensburg

Präsident der Humboldt-Universität zu Berlin:
Prof. Dr. J. Mlynek

Dekan der Mathematisch-Naturwissenschaftlichen Fakultät I:
Prof. Dr. B. Ronacher

Gutachter:

1. Priv.-Doz. Dr. Hans-Jürgen Wünsche
2. Prof. Dr. Roland Zimmermann
3. Prof. Dr. Detlef Hommel

eingereicht am:	14. August 2000
Tag der mündlichen Prüfung:	18. Januar 2001

Abstract

In this thesis, various aspects of the influence of localization, disorder, and polarization fields on electron-hole states in wide-gap semiconductor quantum wells (QWs) are investigated theoretically.

A theoretical treatment of quantum well exciton and biexciton states in the limit of weak localization is presented, using a center-of-mass separation ansatz. It shows that the localization energy of the biexciton is more than twice as large as that of the exciton due to the universal behaviour of localization in weak two-dimensional potentials which is ruled only by the potential "volume" $\int d^2r|V(\mathbf{r})|$ and the mass of the localized particle. A useful simple model of the QW biexciton wavefunction is developed which provides good agreement with the results obtained with an extensive numerical solution.

The limit of strong localization of QW excitons and higher exciton complexes $X_{n\geq 2}$ is investigated with a density functional calculation. It is demonstrated that states at least up to X_4 may localize in nm-scale potential boxes caused by indium phase separation in (In,Ga)N/GaN QWs. The transition spectrum of the successive recombination of a localized X_4 is calculated.

A systematic investigation of the influence of the sample design of (In,Ga)N/GaN QW structures on optical transition energy and oscillator strength reveals the importance of space charge layers with regard to screening of polarization fields along the QW-axis. Based on a self-consistent solution of the Schrödinger-Poisson equations, the overall situation of the macroscopic spontaneous and piezoelectric polarization fields is discussed in dependence on various substantial sample parameters. It is found that the position of a QW in the sample with respect to an extended surface depletion layer—which is shown to exist in n-type Ga-face grown material—severely affects transition energy and electron-hole overlap. Due to the spatial variation of the field strength in this surface depletion layer, the optical transition spectrum of a Ga-face grown multiple-QW can display shoulders or even a multiple-peak structure.

Indium surface segregation results in a blueshift of the transition energy compensating up to one third of the quantum confined Stark shift produced by the polarization field. This blueshift is accompanied by a decrease of the electron-hole overlap.

Polarization fields in (In,Ga)N/GaN multiple-QWs result in a smoothing of the step-like single-particle absorption spectrum. Apart from the contribution of compositional fluctuations, the fields have significant influence on the shape of the spectrum via the abrogation of the nearly diagonality of inter-subband transitions and via the mini-band dispersion of higher coupled states in case of a periodic structure.

A line broadening-mechanism due to polarization fields in (In,Ga)N/GaN QWs, as sometimes discussed in literature, could not be confirmed. Assuming uncorrelated (In,Ga)N alloy and in-plane-correlated interface roughness of one monolayer in each interface, the calculation of the spectral width of the QW exciton center-of-mass potential yields a narrowing with increasing average field. This is a result of the penetration of the carriers into the barriers and of an increasing exciton volume. In case of a long-range interface roughness, a splitting of the spectrum into individual lines can be predicted.

Keywords:
Indium Gallium Nitride, Quantum Wells, Polarization Fields, Exciton Localization

Zusammenfassung

In der vorliegenden Arbeit werden verschiedene Aspekte des Einflusses von Lokalisation, Unordnung und Polarisationsfeldern auf Elektron-Loch Zustände in Quantengräben (QWs von engl. *quantum wells*) aus Halbleitern mit großer Bandlücke theoretisch untersucht.

Unter Verwendung eines Schwerpunktseparationsansatzes wird das Verhalten von QW Exzitonen und Biexzitonen im Grenzfall schwacher Lokalisation beschrieben. Es zeigt sich, daß die Lokalisationsenergie des Biexzitons mehr als doppelt so groß ist wie die des Exzitons. Dies wird verursacht durch ein universelles Gesetz der Lokalisation in schwachen zwei-dimensionalen Potentialen, welches lediglich durch das "Potentialvolumen" $\int d^2r|V(\mathbf{r})|$ und die Masse des lokalisierten Teilchens bestimmt wird. Ein einfaches Modell des QW Biexzitons wird entwickelt, dessen Ergebnisse gut mit jenen übereinstimmen, die man mit Hilfe eines aufwendigeren numerischen Modells erhält.

Der Grenzfall starker Lokalisation von QW Exzitonen und höheren Exzitonenkomplexen $X_{n\geq 2}$ wird mittels einer Dichtefunktionalrechnung untersucht. Es wird gezeigt, daß Zustände bis mindestens zum X_4 in den nm-großen Potentialminima lokalisieren können, die durch Phasenseparation in (In,Ga)N/GaN QWs enstehen. Es wird das Übergangsspektrum des sukzessiven Zerfalls eines lokalisierten X_4 berechnet.

Auf Grundlage der selbstkonsistenten Lösung von Poisson- und Schrödinger-Gleichung wird der Einfluß des Probendesigns von (In,Ga)N/GaN QW-Strukturen auf den makroskopischen Verlauf des Polarisationsfeldes in Wachstumsrichtung und somit auf optische Übergangsenergie und Oszillatorstärke systematisch untersucht. Besondere Bedeutung kommt dabei der Abschirmung der Felder durch Raumladungszonen zu. Es wird gezeigt, daß die Position des QW bezüglich einer ausgedehnten Oberflächen-Verarmungszone — die in n-dotierten, Ga-polarisierten Proben auftritt — erheblichen Einfluß auf Übergangsenergie und Oszillatorstärke hat. Durch die räumliche Variation der Polarisationsfeldstärke in dieser Verarmungszone kann das optische Übergangsspektrum eines Mehrfach-QW Schultern oder mehrere Maxima aufweisen.

Indium Oberflächen-Segregation ruft eine Blauverschiebung der Übergangsenergie hervor, die bis zu einem Drittel der vom Polarisationsfeld verursachten *quantum confined Stark*-Verschiebung kompensiert. Diese Blauverschiebung wird von einer Verringerung des Elektron-Loch Überlapps begleitet.

Die Polarisationsfelder in (In,Ga)N/GaN Mehrfach-QWs verschmieren das stufenförmige Einteilchen-Absorptionsspektrum. Durch die Aufhebung der näherungsweisen Diagonalität von Inter-Subband Übergängen und durch die Miniband-Dispersion in höheren, gekoppelten Zuständen haben diese Felder, neben dem Beitrag von Potentialfluktuationen, einen entscheidenden Einfluß auf die Form des Absorptionsspektrums.

Ein in der Literatur diskutierter Mechanismus, der allein durch Polarisationsfelder eine Verbreiterung optischer Spektren hervorruft, kann nicht bestätigt werden. Unter Annahme einer unkorrelierten Zusammensetzung von (In,Ga)N und einer lateral korrelierten Grenzflächenrauhigkeit von einer Monolage in jeder Grenzfläche zeigt die spektrale Breite des Exzitonen-Schwerpunktpotentials eine Verschmälerung mit zunehmendem Feld. Diese wird verursacht durch das Eindringen der Teilchen in die binären Barrieren und durch ein vergrößertes Exzitonenvolumen. Im Fall einer langreichweitigen Grenzfächenrauhigkeit findet man eine Aufspaltung des Spektrums in einzelne Linien.

Sclagwörter:
Indium Gallium Nitrid, Quantengräben, Polarisationsfelder, Lokalisation von Exzitonen

Contents

Introduction

Motivation

Research and development of light emitters have always been major tasks in science. Not only for lighting but also for communication purposes highly efficient light emitters with specially designed spectral properties are desired. The field of applications comprises displays, advertisements, indicator and traffic lights, optical fiber network, optical data storage (e.g. on compact discs), high-resolution and high-speed printers, medical applications, and, of course, all kinds of lighting. Because of the huge size of market existing for certain kinds of emitters an improvement in efficiency of a device can be crucial for saving a lot of power and for making a lot of money. For example, the red, amber, and green radiation of common traffic lights contains only about 15%, 70%, and 70%, respectively, of the power produced by the white emitting incandescent bulb behind the filter [136]. Therefore, the development of light sources which emit only the desired part of the spectrum and which have a higher efficiency and a longer lifetime than incandescent bulbs is a very lucrative venture.

Compound semiconductor spontaneous and stimulated emitters on the basis of arsenides and phosphides are famous for their smallness, efficiency and lifetime in comparison to coloured light from filtered incandescent lamps and to other laser systems, respectively. Their major disadvantage is the restriction to the long-wavelength part of the optical spectrum (red-to-yellow). The availability of efficient blue semiconductor emitters would raise two major applications. The first is the ability to produce sources of all three primary colours on the common basis of semiconductor technology and thus also a white emitter which has a much higher efficiency and a longer lifetime than an incandescent lamp. The second application is the possibility of increasing the density of data on optical data carriers. The latter is a consequence of

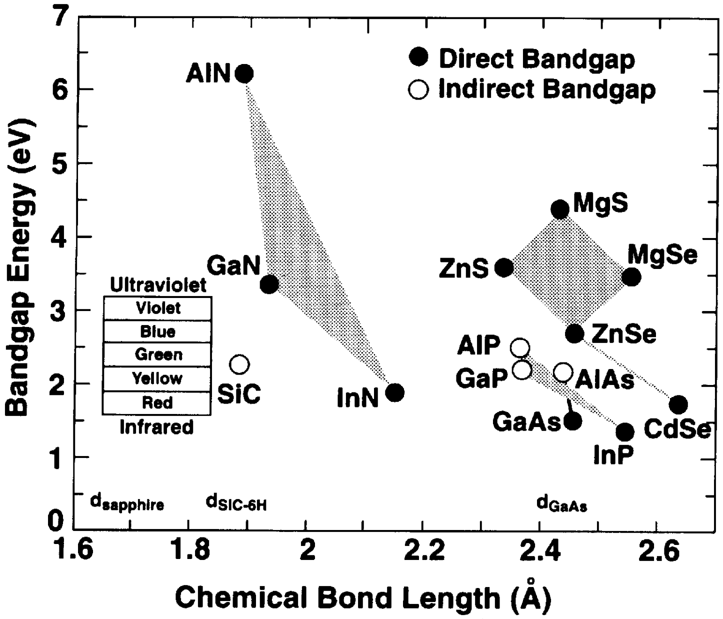

Figure 1: *Bandgap energy and chemical bond length of semiconductor compounds that emit in the visible range of the electromagnetic spectrum. The chemical bond length or interatomical separation is shown here, instead of the lattice parameter, to allow proper comparison of the hexagonal (wurtzite) nitrides with the cubic (zincblende) arsenides, phosphides, selenides, and sulphides. The figure is taken from Ref. [135]*

the proportionality between the diameter of a focused spot and the wavelength of the light. Furthermore, short-wavelength semiconductor emitters in combination with existing red ones could be used for achieving any desired colour tone in the chromaticity diagram by appropriately mixing the colours.

This is where wide-gap semiconductors like II-VI compounds and group-III-nitrides (in the following described by III-nitrides or nitrides) come into play. They have large band gap energies necessary for emitting in the short-wavelength range of the optical spectrum (green-to-ultraviolet). This is illustrated by the position of the nitrides, selenides, and sulphides in the upper region of Fig. 1, which gives an overview of bandgap energy versus chemical bond length for various semiconductor compounds. Although even lasing has already been demonstrated in (Zn,Cd)Se/ZnSe structures [123, 63, 169], the nitride devices are superior at present due to much higher efficiency and longer lifetime. One reason for the latter are their stronger chemical bonds (illustrated by the position of the nitrides in the left region of Fig. 1) which make them stable and resistant to degradation under conditions of high electric currents and intense light illumination. Today, there are at least seven companies which commercially offer (In,Ga)N-based light emitting diodes (LEDs), and the Nichia violet (In,Ga)N-based continuous wave laser diode (LD) with a lifetime of 10.000 hours at room temperature [4] may be regarded as the present climax of the nitride semiconductor research.

However, despite of the great commercial success the III-nitride devices meanwhile have, research and development of nitride emitters was and still is not as straight forward as one may hope due to some fundamental differences to the well established III-V compound material systems based on arsenides and phosphides. It took several years of intensive investigations to overcome major obstacles like e.g. production of p-type material, reduction of defect density, and growth of ternary alloys for tuning the emission wavelength. (For a more detailed review of the history of research and development of the III-nitrides see Refs. [136, 135, 112, 5, 117].) Unfortunately, the commercial breakthrough was not accompanied by a thorough understanding of the physical processes taking place during the performance of the devices. Strongly dependent on growth process, sample structure and experiment, various different phenomena have been reported in literature. Some of these findings can be explained by different mechanisms. In the next section, the main optical properties of (In,Ga)N-based quantum structures and possible explanations will be introduced.

Optical Properties of (In,Ga)N-based Quantum Structures

Before turning to the III-nitrides, it should be pointed out that they are not the only possible materials to emit green-to-ultraviolet radiation. There were predecessors like the indirect semiconductor SiC, from which a blue LED with very low efficiency has been fabricated [20], and there are competitors like organic emitters [158] and the already mentioned II-VI semiconductor compounds based on ZnSe. However, the material instability of the latter under device operation conditions diminishes the potential usefulness for commercial applications at present. Nevertheless, the selenides are of great interest from the physical point of view for optical experiments due to a smaller inhomogeneous broadening of optical features and due to just as strong excitonic effects as observed in nitrides. For example, it has been observed that localized biexcitons provide stimulated emission in (Zn,Cd)Se/ZnSe quantum wells (QWs) below a temperature of 150 K [84, 85, 86]. The stability of the QW biexcitons is significantly enhanced by in-plane localization in potential fluctuations due to compositional inhomogeneity and interface roughness. In this work, the limit of weak localization of biexcitons in (Zn,Cd)Se/ZnSe QWs is investigated theoretically. However, concerning the realization of long-lifetime devices, the III-nitrides seem to have come out on top. The rest of this section is devoted to the optical properties of (In,Ga)N-based quantum structures reported in literature.

Photoluminescence (PL) spectra of (In,Ga)N/GaN single- and multiple-QWs (SQWs and MQWs, respectively) exhibit a very broad peak with a full width at half maximum (FWHM) of 50–200 meV (see Fig. 2). The spectra often exhibit a low- or high-energetic shoulder or even a side maximum. The energetic position of the peak can not be described as a universal function of indium content and well width only, but seems to depend on further sample properties. A shift of the PL line of up to several hundred meV is observed when doping density [110, 35, 30, 31, 108, 41, 76, 37], excitation density [110, 172, 76, 165, 173], injection current density [29, 131], or width of the QW [33, 15, 172, 165, 64, 74, 142] is changed. The emission line peak shows various kinds of s-shaped temperature dependencies at low temperatures [172, 142, 36, 109, 176, 168].

Photoluminescence excitation (PLE) spectra show a very smoothly increasing signal with increasing excitation energy characterized by a low-energetic tail which may extend up to several hundred meV (see again Fig. 2). The onset of the PLE signal lies in the high-energetic tail of the PL curve or even higher. The distance between the PL maximum and the flank of the PLE signal, commonly referred to as Stokes shift, is very large in comparison to other material systems. These experimentally observed main features of optical spectra of (In,Ga)N/GaN QW structures are discussed in terms of

- strong excitonic correlation in III-nitrides (the exciton in pure bulk GaN has a binding energy of about 25 meV and an exciton Bohr radius of about 3 nm)
- strong localization effects in band edge fluctuations due to marked compositional inhomogeneities in connection with a large difference be-

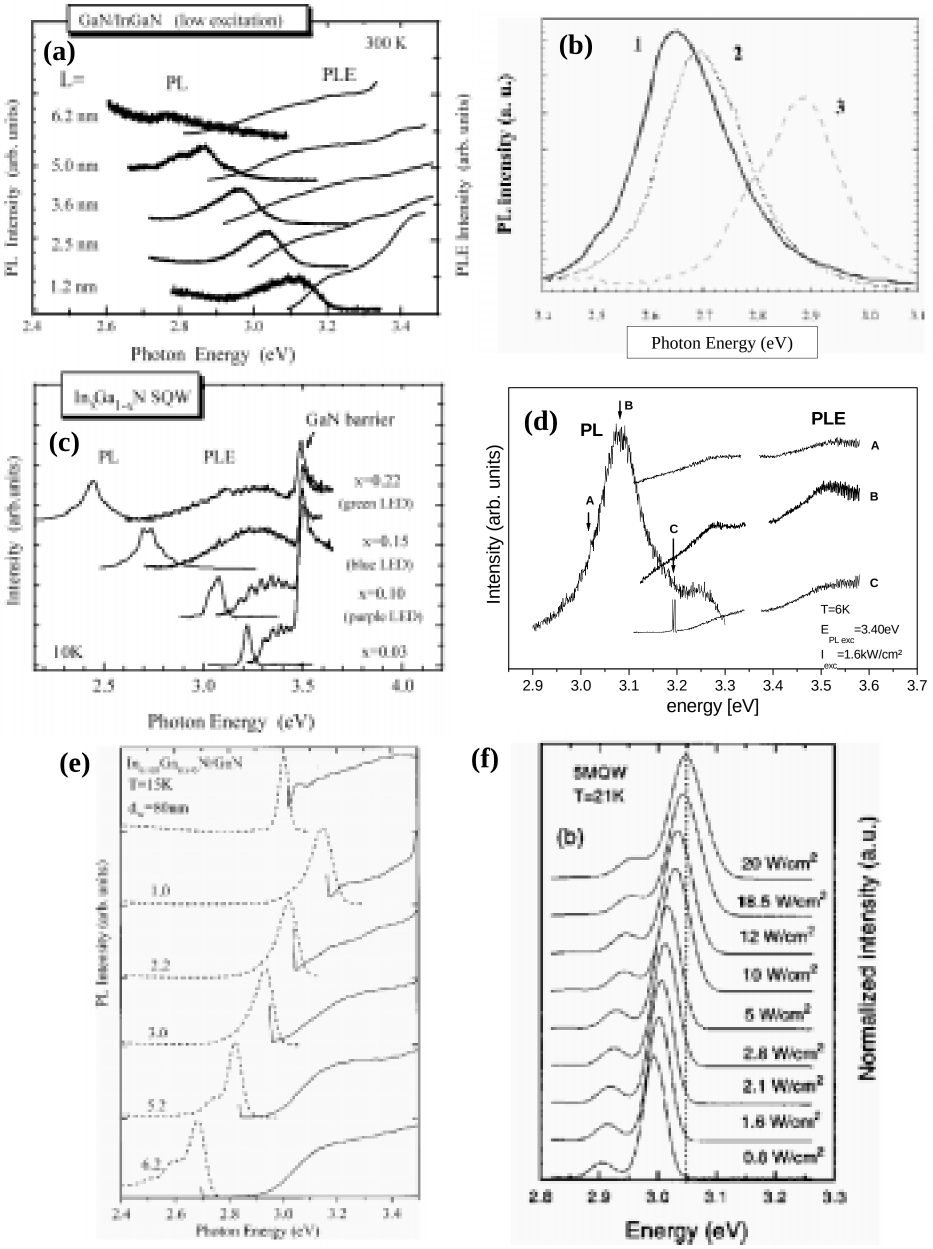

Figure 2: *Photoluminescence (PL) and photoluminescence excitation (PLE) spectra of (In,Ga)N/GaN QW structures. (a): $In_{0.1}Ga_{0.9}N/GaN$ MQWs with various well thicknesses (Chichibu et al. [33, 35]). (b): 3 nm thick $In_{0.15}Ga_{0.85}N/GaN$ MQWs at $T = 2\,K$ with different Si-background doping concentrations (Monemar et al. [110]). (c): 3 nm thick $In_xGa_{1-x}N/GaN$ SQWs with various indium concentrations in the well (Chichibu et al. [35]). (d): 3 nm thick $In_{0.05}Ga_{0.95}N/GaN$ MQW with various detection energies for the PLE (Rau et al. [1]). (e): $In_{0.105}Ga_{0.895}N/GaN$ MQWs with various well thicknesses (Berkowicz et al. [15]). (f): 7.5 nm thick $In_{0.13}Ga_{0.87}N/GaN$ MQW for various excitation power densities (Wang et al. [172]).*

tween the band gap energies of InN and GaN ($\Delta E_{\mathrm{g}} = 1.6\,\mathrm{eV}$) and a large bowing parameter ($b = 2 - 3\,\mathrm{eV}$)

- the quantum confined Stark effect (QCSE) due to large spontaneous polarizations and large piezoelectric coefficients of the wurtzite[1] III-nitrides.

The question, which effect dominates the processes in optical experiments, is one of the most frequently discussed problems in nitride literature. Meanwhile, it seems to be accepted that both polarization fields as well as localization effects play important roles in carrier dynamics and recombination processes. It seems to strongly depend on growth process, sample structure and experiment, which effect appears to be dominant and thus which model better describes the observations.

Clear evidence for the impact of polarization fields along the wurtzite c-axis (which coincides with the growth- or QW-axis in all structures discussed in this work) on the optical properties of III-nitride QW structures was provided by the experimental observation that the emission energy of a GaN/(Al,Ga)N QW lies below the gap energy of the GaN well material for certain values of the well width [64, 74, 95, 92, 156, 39]. In these cases, the redshift of the QCSE—which is approximately proportional to the well width in this regime—overcompensates the blueshift of the QW single-particle confinement. This effect can not be understood in terms of localization in potential fluctuations. The same holds for the characteristic redshift of the transition energy and the concomitant increase of the decay time in (In,Ga)N/GaN QWs when increasing the well width [33, 15, 165, 64, 142]. These findings can be explained with a polarization field inside the QW along the QW-axis of the order of 1 MV/cm. Furthermore, it has been observed that the transition energy exhibits a large time dependent redshift after intense pulsed excitation. This can be attributed to the polarization field screening by photoexcited carriers [110, 15, 41, 64, 74, 26].

Ab-initio calculations confirm the existence of strong spontaneous and strain-induced polarization fields in wurtzite III-nitride QW structures [17, 155]. The spontaneous polarization is a result of the singular polar axis (the c-axis) of the wurtzite crystal structure and the strong polarity of the III-N

---

[1] Besides the wurtzite phase, there is a metastable cubic phase of the III-nitrides without a spontaneous polarization axis and with somewhat smaller band gap energies [21, 8, 7, 71]. However, this work deals only with wurtzite III-nitrides.

binding. However, the appearance of fields in heterostructures is connected to only the difference in total polarization between the materials. The abrupt variation of the polarization at surfaces and interfaces gives rise to large polarization sheet charges that in turn create internal electric fields. In this work, various consequences of these polarization fields on optical spectra of (In,Ga)N/GaN QW structures are investigated theoretically.

Experiments which observe a line shift when changing doping level or excitation density (see Figs. 2 b and f, respectively) can basically be explained by the screening of both polarization fields and/or in-plane potential fluctuations. Due to the lack of knowledge about actual structure and statistics of the localization sites, an exact quantification of both contributions is hardly possible [110, 76]. Therefore, to be able to investigate theoretically the effects of polarization field screening, the homogeneous alloy model for (In,Ga)N is usually assumed in such calculations [110, 76, 165, 131, 64, 74, 150, 54, 149].

There are several spatially resolved investigations of compositional inhomogeneities in (In,Ga)N QWs which come to different conclusions concerning the size of the indium-rich regions attracting carriers due to a smaller band gap energy [119, 32, 106, 171, 48, 162, 55, 81]. This may be an indication that the compositional fluctuation occurs with more than one characteristic length scale. The formation of fluctuations is confirmed by thermodynamical considerations, which predict a broad solid-phase miscibility gap for (In,Ga)N alloy [72, 147]. The important role of these localization sites for the device performance seems to be that they keep carriers away from nonradiative recombination centers like e.g. the omnipresent threading dislocations. The localization sites result in an extended low-energetic tail of the density of states, reflected in the large linewidth of the PL emission line and in the smooth shape of the PLE signal. Whether the large linewidth of the PL, which is commonly related to only the potential fluctuations, can also be explained by a broadening due to the polarization field, as also discussed in literature [124, 65], is one subject of this work. Furthermore, it is investigated whether higher exciton complexes can localize in the compositional inhomogeneities and how they contribute to the transition spectrum. There are further experimental findings which are not explainable with polarization fields only but which can be related to potential fluctuations like the mobility-edge behaviour and the anomalous temperature dependence of the transition energy.

The occurrence of a high-energetic shoulder or a side maximum in the PL spectrum has been attributed to a bimodal distribution of localized states on the one hand (main peak) and extended actual QW states on the other hand (high-energetic feature) [118]. Low-energetic shoulders have been correlated to recombination from side-wall QWs with an enhanced indium content at so called V-defects [180]. In this work, a further mechanism is suggested which produces high-energetic shoulders and side maxima.

Compositional fluctuations and resulting inhomogeneous strain fields in conjunction with the large piezoelectric coefficients presumably give rise to new effects in the interplay of localization and fields. This may explain the difficulty to experimentally determine optical properties of (In,Ga)N alloy like the dependence of the band gap energy on the indium content. A large scattering of the values for the bowing parameter can be found in literature, concerning both experimental [132, 153, 116, 126, 154, 175, 145, 105, 166, 129] as well as theoretical [179, 89, 14, 13] investigations. To estimate the magnitude of influence of only the polarization fields along the QW-axis on the transition energy, a systematic investigation of the overall situation of the polarization field in dependence on the sample design of (In,Ga)N/GaN SQWs and MQWs is presented in this work.

Content and Organization of this Work

Chapter 1 provides the general theoretical framework for the following investigations. Useful approximations for the treatment of many interacting particles in a QW with disorder and polarization fields are introduced. Formulae for the description of band gap energy and polarization in QW structures are given.

In chapter 2, a theoretical treatment of QW exciton and biexciton states in the limit of weak in-plane localization is presented, using a center-of-mass separation ansatz. This approach, which has been developed and successfully applied before to excitons in disordered systems [188, 189, 10, 11], is extended to biexcitons. Three models for the QW biexciton wavefunction are used. An advanced approach based on an extensive numerical solution provided by a co-working group [152, 143] is compared with two more simple models. The results are related to the correspondingly treated single exciton localization. Not only the weak localization behaviour of the biexciton is clarified, but the assessment of the different models reveals a useful simple approach to the QW biexciton wavefunction with clearly less numerical expenditure than the extensive solution. It is based on an adiabatic-like hole-hole separation ansatz and an interpolation for the interaction between 2D and 3D controlled by the measure of the QW exciton.

All further subjects deal with optical properties of (In,Ga)N/GaN QW structures. In chapter 3, it is investigated whether the experimentally observed clusters with enhanced indium content are capable of localizing higher exciton complexes with more than two electrons and holes. Since the above described procedure of separations is not applicable in this case, a two-component density functional formalism in local density approximation is used to solve this problem. The spectral width of the successive recombination of localized multi-excitons with up to four electrons and holes is considered to estimate the contribution to the total emission linewidth.

The following chapters deal with effects in connection with polarization fields along the QW-axis in (In,Ga)N/GaN QW structures. In chapter 4, a systematic investigation of the influence of the polarization fields on optical transition energy and oscillator strength in dependence on the sample design of (In,Ga)N/GaN SQWs and MQWs with thin cap layers is presented. Based on a self-consistent solution of the Schrödinger-Poisson system of equations, the overall situation of the macroscopic spontaneous and piezoelectric polarization field is discussed in dependence of various substantial sample parameters: Background doping density, indium content, thickness of the cap layer, number of the QWs, and polarity of the structure. A mechanism for the occurrence of asymmetric lineshapes or side maxima in optical transition spectra of MQWs is discussed. The time dependence of decay and transition energy shift due to an excitation-induced screening of the polarization fields under pulsed high photoexcitation is calculated. Furthermore, the combined impact of polarization fields and indium surface segregation in a heterostructure interface is investigated.

The single-particle absorption spectrum of an (In,Ga)N/GaN superlattice is calculated in chapter 5 under consideration of polarization fields. It is investigated, if the fields provide a further explanation (apart from compositional fluctuations) for the smooth increase of PLE spectra found in experiments with (In,Ga)N/GaN MQWs.

It has been discussed in literature whether polarization fields can be the origin of an emission line broadening-mechanism [124, 65]. Therefore, the impact of a polarization field on the disorder broadening of excitons in (In,Ga)N/GaN QWs is investigated theoretically in chapter 6. Both uncorrelated alloy fluctuation and in-plane-correlated interface roughness of one monolayer in each interface are considered in the framework of a center-of-mass separation approach. Not only the fluctuation of the band edges, but also the fluctuation of the long-range polarization field of spontaneous and strain-induced dipole moments is taken into account. As a measure for the spectral width of the optical density of states, the spectral width of the QW exciton center-of-mass potential in terms of its standard deviation is calculated in dependence on an average polarization field in the well. Furthermore, the dependence of the results on the interface roughness correlation length is investigated.

Chapter 1

General Theoretical Considerations

To treat the problem of many interacting particles in a QW with disorder and polarization fields theoretically, it is helpful to make approximations. The method followed here is to weigh the magnitude of energetic contributions in the Hamiltonian to the relevant states. Large contributions are considered by solving the Schrödinger equation neglecting smaller contributions, small contributions are treated perturbatively.

The standard model for the treatment of excited semiconductors is adopted, which describes the interaction between an excited electron and the Fermi sea of valence band electrons in terms of the interaction between a conduction band electron and a hole in the valence band. Since we want to investigate effects which are dominated by the variation of external potentials, the kinetic energy and the Coulomb interaction are treated in simple approximations. The kinetic energy is considered in effective mass approximation in a two-band model and the interaction neglects electron-hole exchange, frequency-dependent screening, and charge image effects. Thus, the base multi-particle Schrödinger equation reads

$$\left[\sum_i -\frac{\hbar^2}{2m_{a(i)}}\Delta_{\vec{\mathrm{r}}_i} + V_{a(i)}(\vec{\mathrm{r}}_i) + \frac{1}{2}\sum_{j\neq i}\frac{\mathrm{q}_{a(i)}\,\mathrm{q}_{a(j)}}{4\pi\varepsilon\varepsilon_o|\vec{\mathrm{r}}_i-\vec{\mathrm{r}}_j|}\right]\Phi = E\,\Phi \tag{1.1}$$

where $i, j = e1, e2, ..., h1, h2, ...$ run over all particles (electrons and holes) and $a(i) = e$ or h denotes the particle sort. m_a are the effective masses, $V_a(\vec{\mathrm{r}}_i)$ are the single-particle potentials, ε is the static dielectric constant of the semiconductor, $q_e = -e$ and $q_h = +e$ is the charge of an electron and a hole, respectively, and E is the total energy. Since electrons and holes are Fermions, the total wavefunction Φ must fulfil an antisymmetric exchange relation with respect to the exchange of two conduction band electrons or two holes in the valence band (intraband-exchange).

All systems considered in the following are QW structures where the single-particle confinement in terms of the energetic separation of subsequent subband levels can be considered to be large compared to all other contributions. Therefore, the first approach is to extract QW terms $V_a^{\mathrm{QW}}(z)$, which depend only on the z-coordinate, from the single-particle potentials

$$V_a(\vec{\mathrm{r}}) = V_a^{\mathrm{QW}}(z) + \delta V_a(\vec{\mathrm{r}}) \quad (a = e, h)\,, \tag{1.2}$$

and solve the one-dimensional subband equations

$$\left[-\frac{\hbar^2}{2m_a}\Delta_z + V_a^{\mathrm{QW}}(z)\right]\varphi_a(z) = E_a^{\mathrm{QW}}\varphi_a(z) \quad (a = e, h) \tag{1.3}$$

neglecting particle-particle interactions and further potential variations for the moment. The QW terms $V_a^{\mathrm{QW}}(z)$ describe the band edge discontinuities at well-barrier interfaces and optionally an average polarization field. The remaining terms $\delta V_a(\vec{\mathrm{r}})$ include all further potential variations which do not depend only on z like an additional localization site or disorder. $\varphi_a(z)$ and E_a^{QW} are the subband envelope functions and the subband energy levels, respectively.

If the energetic contributions resulting from $\delta V_a(\vec{\mathrm{r}})$ can be considered to be small compared to the QW exciton binding energy, the next step in the energetic hierarchy in the Schrödinger equation (1.1) is the QW exciton formation due to the Coulomb attraction between electrons and holes. In this limit the internal motion of the QW exciton is almost not affected by the potential variations described by the remaining term $\delta V_a(\vec{\mathrm{r}})$ so that its influence can be treated perturbatively. This can be realized by a separation of the relative coordinates from the center-of-mass (CM) coordinate, an approach which has been developed for the treatment of excitons in disordered systems [188, 189, 10, 11]. It has been successfully applied to calculate exciton absorption and luminescence lineshapes as well as the non-monotonic temperature dependence of the Stokes shift in disordered arsenide-based QWs using a kinetic approach with acoustic phonon scattering [189]. Since the center-of-mass separation ansatz is adopted here not only for the exciton but also for the investigation of weak biexciton localization, the following formulae are given for an arbitrary number of electrons and holes in the considered complex. The problem of the internal motion and the center-of-mass problem are solved separately by factorizing the wave function

$$\Phi = \Psi(\mathbf{R})\, \psi(\{\mathbf{q}\}, \{z\}) \tag{1.4}$$

where ψ includes the in-plane relative wavefunction depending on an appropriate set of in-plane relative coordinates $\{\mathbf{q}\}$ and the single-particle subband functions $\varphi_a(z)$. Ψ and $\mathbf{R}$ are the in-plane center-of-mass wavefunction and coordinate, respectively.

To derive a center-of-mass Schrödinger equation from (1.1), we multiply it from the left side with ψ^*, integrate with respect to the sets of coordinates $\{\mathbf{q}\}$ and $\{z\}$, and get

$$\left[-\frac{\hbar^2}{2M}\Delta_{\mathbf{R}} + V_{\mathrm{CM}}(\mathbf{R})\right] \Psi(\mathbf{R}) = (E - E_\psi)\, \Psi(\mathbf{R})\,, \tag{1.5}$$

where M is the total mass of the considered complex, and

$$V_{\mathrm{CM}}(\mathbf{R}) = \int d\{z\}\, d\{\mathbf{q}\}\, \psi^2(\{\mathbf{q}\}, \{z\}) \sum_i \delta V_a \left[\vec{\mathrm{r}}_i(\mathbf{R}, \{\mathbf{q}\}, \{z\})\right] \tag{1.6}$$

is the center-of-mass potential. The energy E_ψ is given by

$$\left[\sum_i -\frac{\hbar^2}{2m_a}\Delta_{z_i} + T_{\{\mathbf{q}\}} + V_a^{\mathrm{QW}}(z_i) + \frac{1}{2}\sum_{j\neq i} \frac{\mathrm{q}_{a(i)}\, \mathrm{q}_{a(j)}}{4\pi\varepsilon\varepsilon_o |\vec{\mathrm{r}}_i - \vec{\mathrm{r}}_j|}\right] \psi = E_\psi\, \psi\,, \tag{1.7}$$

where $T_{\{\mathbf{q}\}}$ is the kinetic energy operator of the internal in-plane motion. A full separation $\psi(\{\mathbf{q}\}, \{z\}) = \phi(\{\mathbf{q}\}) \prod_i \varphi_a(z_i)$ decomposes equation (1.7) into the subband Schrödinger equations (1.3) and the equation for the internal in-plane motion

$$\left[T_{\{\mathbf{q}\}} + \frac{1}{2}\sum_{\substack{i,j\\ i\neq j}} \tilde{U}_{ij}\right] \phi(\{\mathbf{q}\}) = E_\phi\, \phi(\{\mathbf{q}\}) \tag{1.8}$$

with the effective 2D QW Coulomb potentials

$$\tilde{U}_{ij}(\mathbf{r}_i - \mathbf{r}_j) = \frac{\mathrm{q}_{a(i)}\, \mathrm{q}_{a(j)}}{4\pi\varepsilon\varepsilon_o} \int dz_i\, dz_j\, \frac{|\varphi_{a(i)}(z_i)|^2\, |\varphi_{a(j)}(z_j)|^2}{\sqrt{(\mathbf{r}_i - \mathbf{r}_j)^2 + (z_i - z_j)^2}}\,, \tag{1.9}$$

where $\mathbf{r}_i$ are the individual single-particle in-plane coordinates. It holds $E_\psi = E_\phi + \sum_i E_a^{\mathrm{QW}}$ where E_ϕ is the internal energy of the in-plane motion of the complex in the unperturbated QW $V_a^{\mathrm{QW}}(z)$.

In chapter 6, however, a more general ansatz for the QW exciton is applied, which makes no full separation of the in-plane relative motion from the motion along the QW-axis. This method is well suited for the description of the system in the presence of polarization fields along the QW-axis, where electrons and holes are separated from each other to opposite sides of the QW. The approach is outlined in appendix A.2.

With exception of chapter 3, where the density functional formalism is applied to investigate the limit of strong in-plane localization, the above outlined approach is the general procedure how electron-hole states in QWs with disorder and polarization fields are treated throughout this work.

In the following, the description of QW potential and polarization entering the subband Schrödinger equation (1.3) via the QW terms $V_a^{\mathrm{QW}}(z)$ of the external single-particle potentials is given. The band edge energy discontinuities at well-barrier interfaces can be expressed as

$$V_a^{\mathrm{QW}} = \xi_a \, E_{\mathrm{g}} \quad (a = e, h)\,, \tag{1.10}$$

where $\xi_e = \Delta E_{\mathrm{c}}/\Delta E_{\mathrm{g}}$ and $\xi_h = \Delta E_{\mathrm{v}}/\Delta E_{\mathrm{g}} = 1 - \xi_e$ are the relative band offsets in the conduction and valence band, respectively. For the dependence of the band gap energy E_{g} of a ternary alloy (X,Y)Z on the content x of constituent X, the common interpolation formula

$$E_{\mathrm{g}}(x) = E_{\mathrm{g}}^{\mathrm{YZ}}\,(1-x) + E_{\mathrm{g}}^{\mathrm{XZ}}\,x - b\,x\,(1-x) \tag{1.11}$$

is used, where $E_{\mathrm{g}}^{\mathrm{XZ}}$ and $E_{\mathrm{g}}^{\mathrm{YZ}}$ are the band gap energies of the two binary compounds. The bowing parameter b phenomenologically accounts for the nonlinearity of the relation. The material parameters used in the calculations are listed in Tables placed at the end of the respective chapter.

The III-nitrides in wurtzite phase are known to have strong spontaneous (equilibrium) polarizations and large piezoelectric coefficients [165, 64, 17, 155]. The latter in turn give rise to strong strain-induced polarizations in pseudomorphically grown heterostructures with a lattice mismatch. These polarizations are oriented along the c-axis. The only ternary nitride alloy considered in this work is $\mathrm{In}_x\mathrm{Ga}_{1-x}\mathrm{N}$. Its total polarization can be written as a function of the indium content x

$$P(x) = e_{33}\,\epsilon_\perp(x) + 2\,e_{31}\,\epsilon_{||}(x) + P_{\mathrm{sp}}(x)\,, \tag{1.12}$$

where the first two terms describe the strain-induced (piezoelectric) part, oriented into [0001]-direction (due to the compressive strain state of (In,Ga)N grown pseudomorphically on relaxed GaN). The spontaneous contribution $P_{\mathrm{sp}}(x)$ is calculated by a linear interpolation between the binary compounds and points into $[000\bar{1}]$-direction [17]. e_{ij} are the coefficients of the piezoelectric tensor and

$$\epsilon_{||}(x) = \frac{a_{\mathrm{GaN}} - a(x)}{a(x)} \quad \text{and} \quad \epsilon_{\perp}(x) = \frac{\tilde{c}(x) - c(x)}{c(x)} \tag{1.13}$$

are the strain components parallel and perpendicular to the QW plane, respectively. The corresponding lattice constants are denoted as a and c. Vegard's law is assumed for calculating the relaxed lattice constants $a(x)$ and $c(x)$ of the ternary $\mathrm{In}_x\mathrm{Ga}_{1-x}\mathrm{N}$ alloy. The actual lattice constant $\tilde{c}(x)$ of the strained $\mathrm{In}_x\mathrm{Ga}_{1-x}\mathrm{N}$ QW is determined by the elastic constants C_{ij} of the material

$$\tilde{c}(x) = c(x)\left(1 - 2\,\frac{C_{13}}{C_{33}}\,\epsilon_{||}(x)\right). \tag{1.14}$$

Two possible orientations of the spontaneous polarization with respect to the growth direction have to be distinguished. The spontaneous polarization vector points towards the substrate in case of Ga-face polarity and towards the surface in case of N-face polarity.[70, 6] Both polarization types can be grown and will be compared in case they are yielding different results.

$P[x(\vec{\mathrm{r}})]$ varies with the coordinate $\vec{\mathrm{r}}$ via the variation of the indium content, and hence exhibits discontinuities at interfaces of materials with different total polarizations. These spatial variations of P give rise to the polarization charge density

$$\rho_{\mathrm{P}}(\vec{\mathrm{r}}) = -\frac{\partial}{\partial z}P[x(\vec{\mathrm{r}})]\,, \tag{1.15}$$

that in turn creates huge electric fields. The abrupt disappearance of the spontaneous polarization P_{sp} at the (0001)- or $(000\bar{1})$-surface of GaN causes a bare field as large as $|F_{\mathrm{sp}}| = |P_{\mathrm{sp}}/\varepsilon\varepsilon_o| \approx 3.5\,\mathrm{MV/cm}$. Inside a (In,Ga)N/GaN QW, the piezoelectric contribution dominates the polarization, because the spontaneous polarizations of GaN and InN do not differ noticeably. Depending on the indium content, the field in a QW caused by the strain-induced polarization of the (In,Ga)N well material can get even larger than the maximum spontaneous field at the GaN surface.

Energies and distances are often given in excitonic units: $a_{\mathrm{x}} = \hbar^2 4\pi\varepsilon\varepsilon_o/e^2\mu$ is the bulk exciton Bohr radius, where $\mu = m_e m_h/(m_e + m_h)$ is the reduced mass, and $Ry_{\mathrm{x}} = \hbar^2/(2\mu a_{\mathrm{B}}^2)$ is the bulk exciton Rydberg.

Chapter 2

Weak Localization of Biexcitons

2.1 Introduction

Localization of excitons due to alloy fluctuations and interface roughness is an inherent feature of QWs [29, 119, 94, 43, 75, 82, 47, 46]. The laser action in (Zn,Cd)Se/ZnSe QWs has early been related to localized excitons [47, 46]. The conjecture behind this statement is that the repulsive exchange interaction between two excitons in one localization site is much larger than the localization energy per exciton, excluding the localization of a second exciton. Meanwhile, it could be demonstrated that this assumption does not hold. Localized biexcitons have been observed in these structures [84, 85, 86, 141, 24, 25, 87], even providing optical gain up to elevated temperatures [84, 85, 86]. A common feature of these investigations is that the binding energy of a localized biexciton, defined as the separation of the biexciton and exciton photoluminescence lines

$$E_{\mathrm{xx}}^{\mathrm{b}} = 2E_{\mathrm{x}} - E_{\mathrm{xx}} = \hbar\omega_{\mathrm{x}} - \hbar\omega_{\mathrm{xx}}\,, \tag{2.1}$$

is substantially enhanced through the localization. Here, E_{x} and E_{xx} are the energies of an exciton and a biexciton, respectively, relaxed in a localization site. These findings have been related to calculations for strictly zero dimensional biexcitons in quantum dots with infinite barrier [73]. In the present case, however, the potential fluctuations are on the same scale as the biexciton binding energy, making a straightforward prediction about the change of the biexciton state under localization impossible. A density functional calculation in local density approximation indicated that the localized biexciton is approximately twice as stable as the localized exciton [141, 183]. However, a general uncertainty of the local density approximation is that it produces an artificial self-localization even when the external potential is removed. Therefore, a more elaborated treatment of the biexciton in the limit of weak localization avoiding this artifact is presented here.

The procedure is based on the assumption that localization of both exciton and biexciton can be treated in terms of a center-of-mass separation of the in-plane motion, as described in chapter 1. This method requires knowledge of the biexciton relative wavefunction for the ideal QW, for which three different approaches are used. The most advanced model consists in a numerical solution of the in-plane Schrödinger equation in real space by a combination of the Gauss-Seidel method with the inverse iteration technique, using a modified Coulomb interaction potential without a singularity. This method has been developed by V. A. Schweigert *et al.* [152, 143], who made a calculation of a QW biexciton relative wavefunction available for this work. To have alternative approaches with clearly less numerical expenditure, the results are compared to those obtained with two simpler models. A very simplified approach consists in the restriction to only one single degree-of-freedom, which reduces the four-particle-problem to an effective exciton Schrödinger equation [157]. Moreover, an adiabatic-like hole-hole separation model has been developed, based on the two-dimensional hydrogen molecule, extended towards finite hole masses and a finite well-width. The numerical calculations were executed with parameters appropriate to (Zn,Cd)Se/ZnSe QW structures, characterized by large biexciton binding energies of the order of 10 meV.

The chapter is organized as follows. Section 2.2.1 provides the actual procedure based on the general considerations given in chapter 1. The different models for the QW biexciton relative wavefunction are the subject of sections 2.2.2, 2.2.3, and 2.2.4. The treatment of the corresponding excitons is given in appendix A. The results are presented in section 2.3, where the weak localization behaviour is discussed and a comparison and an assessment of the different biexciton models is made. At the end of the chapter a summary is given.

2.2 Theory

2.2.1 General Proceeding

The localization of an exciton or biexciton in terms of the center-of-mass description is given by the solution of the effective one-particle Schrödinger equation (1.5). To calculate the localization energy $E_{\mathrm{loc}} = \sum_a E_a^{\mathrm{QW}} + E_\phi - E$ by solving (1.5), it is useful to express the center-of-mass potential as a sum over convolution integrals

$$V_{\mathrm{CM}}(\mathbf{R}) = \sum_i \int d^2s\, f_a(s) \int dz_i\, |\varphi_a(z_i)|^2\, \delta V_a(\mathbf{R}+\mathbf{s}, z_i) \qquad (2.2)$$

of the single-particle localization potential δV_a with a weight function

$$f_a(s) = \int d\{\mathbf{q}\}\, \phi^2(\{\mathbf{q}\})\, \delta\left[\mathbf{r}_i(\mathbf{R}, \{\mathbf{q}\}) - \mathbf{R} - \mathbf{s}\right] \qquad (2.3)$$

for each particle sort a. The weight functions are normalized via the normalization of the wavefunction ϕ. $\mathbf{r}_i(\mathbf{R}, \{\mathbf{q}\})$ are the individual in-plane coordinates of the particle i in terms of the center-of-mass and relative coordinates. Concluding so far, the localization energy E_{loc} can be calculated directly from the simple effective single-particle equation (1.5), if the weight functions $f_a(s)$—which are functions of only one scalar variable s, the distance from the center-of-mass—for the electrons and holes in the free excitonic complex in the QW are known.

In case of the single exciton, the relative wavefunction ϕ has the only coordinate

$\mathbf{q} = \mathbf{r}_e - \mathbf{r}_h$, so that $\mathbf{r}_a = \mathbf{R} \pm (\mu/m_a)\mathbf{q}$ with the reduced exciton mass $\mu = m_e m_h/(m_e + m_h)$. Consequently, the weight functions are simply [189, 10]

$$f_a(s) = \phi^2\left(\frac{m_a}{\mu}s\right) \quad (a = e, h)\,. \qquad (2.4)$$

In the next sections, three models for the biexciton relative wavefunction in the ideal QW are introduced.

2.2.2 The Quantum Well Biexciton Wavefunction I: Numerical Solution of the Finite-Difference Biexciton Schrödinger Equation

V. A. Schweigert *et al.* [152, 143] have developed a numerical method for calculating the ground-state of an interacting many-particle system. Instead of solving the four-particle Schrödinger equation (1.8) by a diagonalization of the Hamiltonian using an expansion of the wavefunction in a basis of product eigenfunctions of the single-particle Hamiltonian, the method outlined in Ref. [152, 143] directly solves equation (1.8) on a numerical real space grid with a finite-difference representation of the Laplacian. A combination of the Gauss-Seidel method with the inverse iteration technique is applied to find both the lowest eigenvalue and eigenvector.

The effective 2D QW Coulomb potential is approximated by [139, 186]

$$\tilde{U}_{ij}(\mathbf{r}_i - \mathbf{r}_j) \approx \frac{\mathrm{q}_{a(i)}\,\mathrm{q}_{a(j)}}{4\pi\varepsilon\varepsilon_o\sqrt{(\mathbf{r}_i-\mathbf{r}_j)^2 + (\alpha\, d_{\mathrm{QW}})^2}}\,, \tag{2.5}$$

avoiding the logarithmic singularities of the more rigorous expression (1.9). α is a fitting parameter, which is equal to 0.2 in case of infinitely high QW barriers and which depends on the width d_{QW} of the QW in case of finite barrier height. Choosing α such that the resulting QW exciton relative wavefunction approaches the one obtained by using the effective 2D QW Coulomb potential (1.9) as close as possible, we find $\alpha = 0.26$ for a 18 monolayer ($\approx 5.2\,\mathrm{nm}$) $\mathrm{Zn_{0.8}Cd_{0.2}Se/ZnSe}$ QW, for which the calculations in this chapter are executed (for material parameters see Table 2.4). Standard enumeration of the single exciton equation (see appendix A.1) yields an exciton binding energy of 32.7 meV, being in very good agreement with the value of 32.3 meV for the more accurate potential (1.9). Both potentials as well as exciton wavefunctions are plotted for comparison in Fig. 2.1. V. A. Schweigert *et al.* calculated the QW biexciton weight function (2.3) within the above mentioned numerical scheme, obtaining a biexciton binding energy of 3.81 meV for the ideal QW. This value is about three times smaller than experimental data [84, 85, 86, 141], emphasizing the role of localization in real QW structures.

The respective weight functions $f_a(s)$ for electrons and holes in the exciton and the biexciton are shown in Fig. 2.2. In the exciton, the hole weight function is stronger located at the center-of-mass compared to the electron weight function because of the larger hole mass. In contrast to that and as known for the protons in the hydrogen molecule, the hole weight function

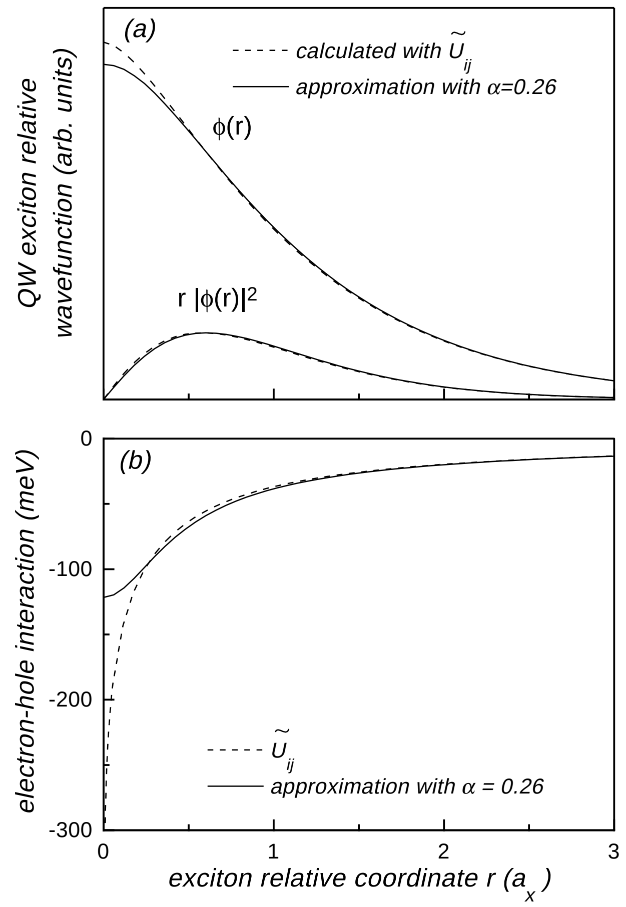

Figure 2.1: *QW exciton relative wavefunctions and probability densities (a), and effective 2D QW Coulomb potentials (b) for a 18 monolayer (≈ 5.2 nm) $Zn_{0.8}Cd_{0.2}Se/ZnSe$ QW. Dotted: potential $\tilde{U}_{ij}$, given by equation (1.9). Solid: approximation for $\tilde{U}_{ij}$, given by equation (2.5) with* $\alpha = 0.26$.

in the biexciton displays a local minimum at the center-of-mass, caused by the Coulomb repulsion of the holes together with their smaller kinetic energy compared to the electrons. The maximum of the electron probability density lies between the holes in the center-of-mass, screening the hole-hole repulsion and making the binding of the complex possible.

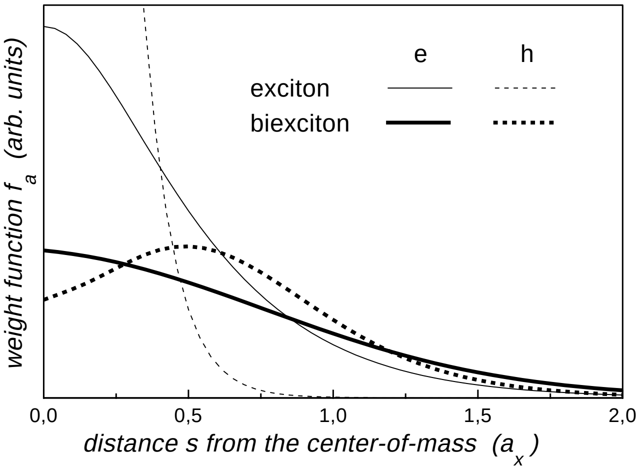

Figure 2.2: *Normalized weight functions $f_a(s)$ ($a = e, h$) for the exciton and the biexciton. The results are obtained by numerically solving the finite-difference Schrödinger equations. For the exciton (thin lines) see appendix A.1 and for the biexciton (thick lines) see section 2.2.2. As for the biexciton, the results for the exciton are calculated using equation (2.5) with* $\alpha = 0.26$.

2.2.3 The Quantum Well Biexciton Wavefunction II: Effective One-Degree-of-Freedom Model

An extremely simplified version of the QW biexciton relative wavefunction, suggested by Singh *et al.* [157], consists in the assumption that the four particles are arranged on the corners of a square, having all the same distance $s = |\mathbf{s}|$ from the center-of-mass, with equally charged particles aligned oppositely. This actually implies that the relative wavefunction includes δ-functions yielding singularities in the kinetic energy.

Using the following set of relative in-plane coordinates

$$\mathbf{r}_e = \mathbf{r}_{e2} - \mathbf{r}_{e1}\,, \qquad (2.6)$$

$$\mathbf{r}_h = \mathbf{r}_{h2} - \mathbf{r}_{h1}\,, \qquad (2.7)$$

$$\mathbf{r}_{eh} = \mathbf{r}_{e1} - \mathbf{r}_{h1}\,, \qquad (2.8)$$

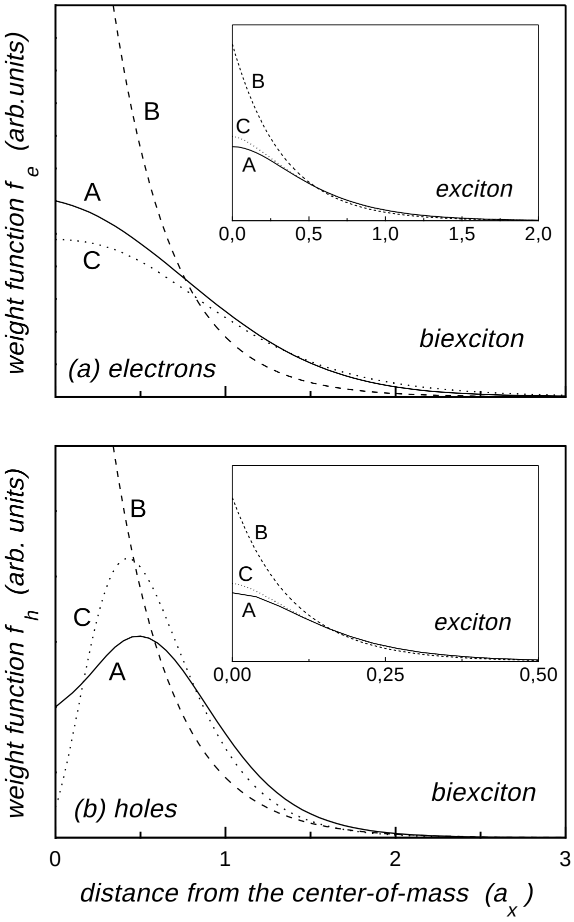

Figure 2.3: *Normalized weight functions $f_a(s)$ $(a = e, h)$ for three models of the QW biexciton relative wavefunction. A: Numerical solution of the finite-difference Schrödinger equation. B: Effective one-degree-of-freedom model (yields identical functions for electrons and holes). C: Hole-hole separation ansatz. Insets: Weight functions for the electron and the hole in the correspondingly described exciton (see appendix A).*

the kinetic part of the Hamiltonian transforms into

$$\sum_{\substack{i=e1,e2,\\h1,h2}} T_i = -\frac{\hbar^2}{4M}\Delta_{\mathbf{R}} - \frac{\hbar^2}{2\mu_{\rm xx}}\Delta_{\mathbf{s}}\,, \tag{2.9}$$

with the exciton total mass $M = m_e + m_h$, and the Coulomb energy reads

$$\sum_{\substack{i,j=e1,e2,h1,h2 \\ i \neq j}} U_{ij} = -\frac{e^2}{4\pi\varepsilon_{\mathrm{xx}}\varepsilon_o s}\,, \tag{2.10}$$

where s is now the only remaining internal degree-of-freedom. In this way, the four-particle-problem reduces to an effective exciton Schrödinger equation with reduced mass $\mu_{\mathrm{xx}} = 2/3\,\mu$ and dielectric constant $\varepsilon_{\mathrm{xx}} = \sqrt{2}/(4-\sqrt{2})\,\varepsilon \approx 0.547\,\varepsilon$. Therefore, the only difference between the exciton and the biexciton relative wavefunctions consists in a different length unit

$$a_{\mathrm{xx}} = \frac{\varepsilon_{\mathrm{xx}}}{\varepsilon}\frac{\mu}{\mu_{\mathrm{xx}}}\,a_{\mathrm{x}} \approx 0.82\,a_{\mathrm{x}}\,, \tag{2.11}$$

yielding an average spatial extension of the biexciton of $1.64\,a_{\mathrm{x}}$, where $a_{\mathrm{x}} = \hbar^2 4\pi\varepsilon\varepsilon_o/(e^2\mu)$ is the exciton Bohr radius in bulk material.

In order to consider the restriction of the system due to the confinement in a QW, the fractional-dimensional ansatz (FDA) [66, 160, 67, 68, 69] is adopted in Ref. [157]. The description of a QW exciton within the framework of the FDA is outlined in appendix A.3. According to Ref. [103], we obtain for a 18 monolayer ($\approx 5.2\,\mathrm{nm}$) $\mathrm{Zn_{0.8}Cd_{0.2}Se/ZnSe}$ QW a value of $\alpha_{\mathrm{FDA}} = 2.72$ for the fractional-dimensional parameter, which yields

$$\frac{a_{\mathrm{x}}^{\mathrm{FDA}}}{a_{\mathrm{x}}} = \left(\frac{Ry_{\mathrm{x}}^{\mathrm{FDA}}}{Ry_{\mathrm{x}}}\right)^{-1} = \left(\frac{\alpha_{\mathrm{FDA}}-1}{2}\right)^2 = 0.74\,, \tag{2.12}$$

where $a_{\mathrm{x}}^{\mathrm{FDA}}$ is the QW exciton Bohr radius [69] and $Ry_{\mathrm{x}}^{\mathrm{FDA}}$ and $Ry_{\mathrm{x}} = \hbar^2/(2\mu a_{\mathrm{x}}^2)$ are QW and the bulk exciton Rydberg, respectively.

The exponential weight function of this model is plotted in Fig. 2.3, labeled with B. Evidently, it deviates remarkably from the weight functions found by solving the finite-difference Schrödinger equation, labeled with A: there is no difference between electrons and holes and the spatial extension is much smaller. Regarding the weight functions of the exciton, the deviations between the models are distinctly less pronounced (see insets of Fig. 2.3).

2.2.4 The Quantum Well Biexciton Wavefunction III: Hole-Hole Separation Ansatz

To have an alternative approach to the QW biexciton wavefunction with clearly less numerical expenditure than the extensive numerical model, described in section 2.2.2, but with more realistic assumptions and results than the one-degree-of-freedom model, described in the previous section, a supplementary model has been developed. It is based on an adiabatic-like hole-hole separation ansatz, outlined in the following.

In the limit of large hole mass ($\sigma = m_e/m_h \ll 1$), a decoupling

$$\phi(\{\mathbf{q}\}) = \phi_{\mathrm{A}}(\{\mathbf{q}\}) \cdot F(h) \tag{2.13}$$

is well suited for constructing an in-plane biexciton relative wavefunction, where h denotes the hole-hole distance. An appropriate choice for the internal wavefunction is the variational ansatz

$$\phi_{\mathrm{A}} = \frac{\phi_{\mathrm{x}}(\gamma\, r_{e1h1})\phi_{\mathrm{x}}(\gamma\, r_{e2h2}) + \phi_{\mathrm{x}}(\gamma\, r_{e1h2})\phi_{\mathrm{x}}(\gamma\, r_{e2h1})}{\sqrt{2(1+S^2)}}\,, \tag{2.14}$$

where ϕ_{x} is the exciton relative wavefunction, depending on the electron-hole distance r_{ij} ($i = e1, e2$; $j = h1, h2$), S is the overlap integral, and γ is a variational parameter accounting for a compression of the exciton within the biexciton. Ansatz (2.13) yields the Schrödinger equation

$$\left[-\frac{\hbar^2}{M}\left(\frac{\partial^2}{\partial h^2} + \frac{1}{h}\frac{\partial}{\partial h}\right) + V(h)\right] F(h) = E_{\mathrm{xx}}\, F(h). \tag{2.15}$$

for the factor $F(h)$, where $M = m_e + m_h$ is the exciton total mass. For the sake of simplicity, instead of calculating the effective exciton-exciton potential $V(h)$ with the aid of equation (2.14) by extensive numerical efforts, this potential is approximated by

$$V(h) = V_{\mathrm{M}}(h) + \frac{e^2}{4\pi\varepsilon\varepsilon_o h}\,\mathrm{e}^{-h/b}\,, \tag{2.16}$$

with the Morse potential [79] $V_{\mathrm{M}}(h) = D \cdot \left[(1 - \mathrm{e}^{-a(h-h_o)})^2 - 1\right]$. The second term ensures the correct asymptotic behaviour for $h \to 0$, which consists of a screened Coulomb repulsion of the holes. For finding the parameters D, h_o, a, and b for a QW, an interpolation between the potentials of the hydrogen molecule in 2D (Ref. [187]) and 3D (Ref. [127]) is made. Since the mass M may be considered as infinite in this case, binding energy and hole-hole separation are directly given by the minimum of the potential curve. The respective parameters are summarized in Table 2.1. For a better comparison of the two potential curves, both plotted in Fig. 2.4, the space and energy coordinates in 2D and 3D are rescaled by the corresponding exciton radius

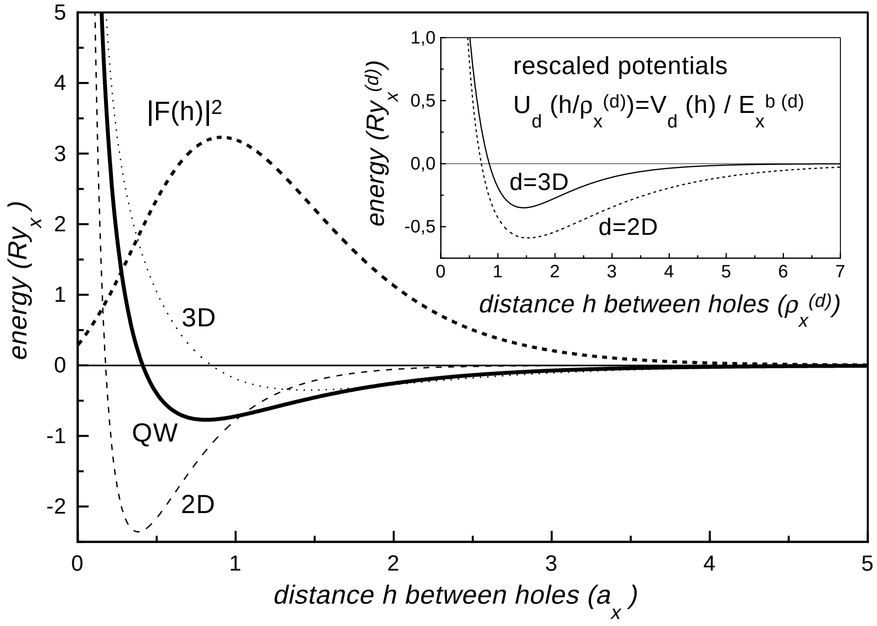

Figure 2.4: *Effective exciton-exciton interaction potentials $V(h)$. Thin dotted: 3D. Thin dashed: 2D. Thick solid: interpolation for a 18 monolayer ($\approx$ 5.2 nm) $Zn_{0.8}Cd_{0.2}Se/ZnSe$ QW. Thick dashed: probability distribution $|F(h)|^2$ for the QW case. Inset: Rescaled potentials $U_d(h/\rho_{\mathrm{x}}^{(d)})$ for the 2D and 3D cases.*

(most probable electron-hole distance) $\rho_{\mathrm{x}}^{(d)}$ (d =2D, 3D) and exciton binding energy $E_{\mathrm{x}}^{\mathrm{b}\,(d)}$, also listed in Table 2.1. Although the absolute values are markedly different, the minima of the resulting rescaled potentials

$$U_d(h/\rho_{\mathrm{x}}^{(d)}) = V_d(h)/E_{\mathrm{x}}^{\mathrm{b}\,(d)} \tag{2.17}$$

appear nearly at the same position $h/\rho_{\mathrm{x}}^{(d)} \approx 1.4$ (see inset of Fig. 2.4), indicating that the size of the molecule scales with the size of the atoms. Hence, it seems reasonable to assume that the same scaling rule holds for the QW. A linear interpolation between between the 2D and 3D potential

$$U_{\mathrm{QW}}(x) = \xi\, U_{\mathrm{2D}}(x) + (1-\xi)\, U_{\mathrm{3D}}(x)\,, \tag{2.18}$$

is used with $x = h/\rho_{\mathrm{x}}^{(\mathrm{QW})}$ and the interpolation parameter $\xi = (\rho_{\mathrm{x}}^{(\mathrm{QW})} - \rho_{\mathrm{x}}^{(\mathrm{3D})})/(\rho_{\mathrm{x}}^{(\mathrm{2D})} - \rho_{\mathrm{x}}^{(\mathrm{3D})})$, where $\rho_{\mathrm{x}}^{(\mathrm{QW})}$ is derived from the exciton wavefunction

Table 2.1: *Exciton binding energy* $E_{\mathrm{x}}^{\mathrm{b}\,(d)}$*, exciton radius (most probable electron-hole distance)* $\rho_{\mathrm{x}}^{(d)}$*, compression parameter* γ*, and the fitting parameters* D*,* h_o*,* a*,* b *for the potential (2.16) for* d *=2D, 3D, and for a 18 monolayer (*$\approx 5.2\,\mathrm{nm}$*)* $Zn_{0.8}Cd_{0.2}Se/ZnSe$ *QW.*

d	$E_{\mathrm{x}}^{\mathrm{b}\,(d)}$ $[Ry_{\mathrm{x}}]$	$\rho_{\mathrm{x}}^{(d)}$ $[a_{\mathrm{x}}]$	γ	D $[Ry_{\mathrm{x}}]$	h_o $[a_{\mathrm{x}}]$	a $[a_{\mathrm{x}}^{-1}]$	b $[a_{\mathrm{x}}]$
2D	4.0	0.25	1.275[a]	2.45	0.35	2.7	0.09
3D	1.0	1.0	1.166[b]	0.35	1.45	1.15	0.09
QW	1.57	0.54	1.227	linear interpolation according to (2.18)			

[a] Ref. [187]
[b] Ref. [56]

solving potential (1.9) (see appendix A.1). The resulting potential $V_{\mathrm{QW}}(h)$ is plotted in Fig. 2.4 together with the probability density $|F(h)|^2$ obtained from the solution of the hole-hole Schrödinger equation (2.15). It should be noted, that the choice for ξ is somewhat arbitrary, but other reasonable interpolations yielded only slightly different results in the numerical examples.

The calculation of the weight functions $f_a(s)$ additionally requires knowledge of the compression parameter γ in (2.14). For this purpose, an interpolation is made in the same way as for the potential U_{QW} between the two values for 2D (Ref. [187]) and 3D (Ref. [56]), listed in Table 2.1. Using an exponential trial function for ϕ_{x}, we find for the 18 monolayer ($\approx 5.2\,\mathrm{nm}$) $\mathrm{Zn_{0.8}Cd_{0.2}Se/ZnSe}$ QW the values $E_{\mathrm{x}}^{\mathrm{b}\,(\mathrm{QW})} = 31.6\,\mathrm{meV}= 1.57\,Ry_{\mathrm{x}}$, $\rho_{\mathrm{x}}^{(\mathrm{QW})} = 2.2\,\mathrm{nm} = 0.54\,a_{\mathrm{x}}$, $\gamma = 1.23$, and a biexciton binding energy $E_{\mathrm{xx}}^{\mathrm{b}} = 2E_{\mathrm{x}} - E_{\mathrm{xx}} = 4.68\,\mathrm{meV}$ with $\xi = 0.61$.

The derivation of the weight functions $f_a(s)$ (labeled as C in Fig. 2.3) from the adiabatic-like biexciton wavefunction (2.13) is outlined in appendix B. In contrast to model B, very good agreement between models A and C is found, concerning the qualitative behaviour of the weight functions as well as the spatial extension of the complex. The hole weight function of the hole-hole separation ansatz shows a sharper peak at equilibrium position and a smaller value for $s = 0$ than that of the finite-difference calculation. The latter might be caused by the different asymptotic behaviour of the particle-particle potentials for vanishing distance. Equation (1.9) underestimates the hole-hole repulsion by avoiding a singularity, whereas the screened $1/h$-potential in equation (2.16) diverges stronger than the logarithmic divergency of the true QW Coulomb potential. Despite of the various simplifications within this hole-hole separation ansatz, the results agree well with the advanced numerical solution, introduced in section 2.2.3.

2.3 Results

The exciton and biexciton localization is considered for cylindrical in-plane single-particle potentials[1]

$$\delta V_a(\vec{\mathrm{r}}_i) = \begin{cases} -\xi_a V_{\mathrm{box}} & \text{if} \quad -d_{\mathrm{QW}}/2 < z < d_{\mathrm{QW}}/2 \quad \text{and} \quad r_i \leq r_{\mathrm{box}} \\ 0 & \text{else} \end{cases} \tag{2.19}$$

of variable radius r_{box} and potential depth V_{box}, covering the full well width d_{QW} in z-direction (see inset of Fig. 2.5). This kind of quantum box (QB) represents an accumulation of material with smaller band gap, surrounded by material with larger band gap. The coefficient $\xi_a = \Delta E_a/\Delta E_{\mathrm{g}}$ denotes the relative conduction and valence band offset, respectively. As the localization potential (2.19) is axial-symmetric, the center-of-mass Schrödinger equation (1.5) is reduced to a one-dimensional problem, which is solved numerically. For the discretization of the radial part of the 2D Laplacian, the second-order representation [59]

$$(\Delta\Psi(R))_i = \frac{1}{\delta^2}\left(\frac{R_{i-1/2}}{R_i}\Psi_{i-1} - 2\Psi_i + \frac{R_{i+1/2}}{R_i}\Psi_{i+1}\right) \tag{2.20}$$

and

$$(\Delta\Psi(R))_0 = \frac{4}{\delta^2}\left(\Psi_1 - \Psi_0\right) \tag{2.21}$$

is used for $i \neq 0$ and $i = 0$, respectively. R_i is the center-of-mass coordinate on the numerical grid point i, and $\delta = R_{i+1} - R_i$ is the increment of the grid.

The explicite calculations are carried out for a set of parameters, appropriate to an 18 monolayer ($\approx 5.2\,\mathrm{nm}$) $\mathrm{Zn_{0.8}Cd_{0.2}Se/ZnSe}$ QW. The material parameters are listed in Table 2.4.

---

[1] In a more realistic treatment of the disorder potential [121], it turns out that localization sites of axial symmetry occur with very low probability. While this has important consequences for the exciton fine structure and spin relaxation, the localization energy itself is not very sensitive on in-plane asymmetries of the potential justifying the use of equation (2.19) in the present context.

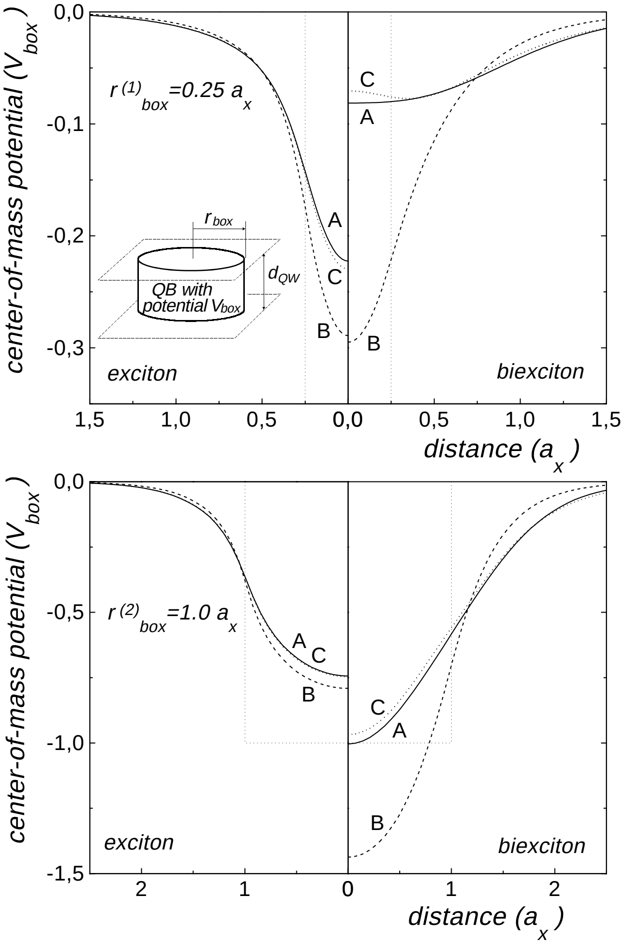

Figure 2.5: *Center-of-mass potentials V_{CM} of the exciton (left side) and the biexciton (right side) for the quantum box radii $r^{(1)}_{\mathrm{box}} = 0.25\ a_{\mathrm{x}}$ (upper layer) and $r^{(2)}_{\mathrm{box}} = 1.0\ a_{\mathrm{x}}$ (lower layer) for the three biexciton models: A: Numerical solution of the finite-difference Schrödinger equation. B: Effective one-degree-of-freedom model. C: Hole-hole separation ansatz. Thin dotted: The single-particle localization potentials δV_a.*

2.3.1 Increased Biexciton Localization

We start discussing the results obtained with the QW biexciton relative wavefunction calculated by solving the finite-difference Schrödinger equation (sec-

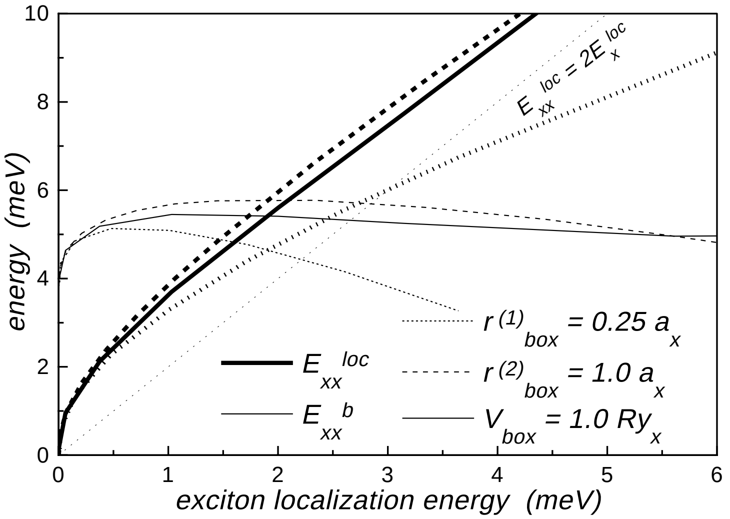

Figure 2.6: *Biexciton localization and binding energies* $E_{\mathrm{xx}}^{\mathrm{loc}}$ *and* $E_{\mathrm{xx}}^{\mathrm{b}}$ *as a function of the exciton localization energy* $E_{\mathrm{x}}^{\mathrm{loc}}$ *in a quantum box, embedded in a 18 monolayer* ($\approx 5.2\,\mathrm{nm}$) *Zn*$_{0.8}$*Cd*$_{0.2}$*Se/ZnSe QW. Dotted: Fixed radius* $r_{\mathrm{box}}^{(1)} = 0.25\ a_{\mathrm{x}}$ *and variable potential depth* V_{box}. *Dashed: Fixed radius* $r_{\mathrm{box}}^{(2)} = 1.0\ a_{\mathrm{x}}$ *and variable* V_{box}. *Solid: Fixed potential depth* $V_{\mathrm{box}} = 1\ Ry_{\mathrm{x}}$ *and variable* r_{box}. *The numerical solution of the finite-difference Schrödinger equation (model A) has been used for this calculation. The line with* $E_{\mathrm{xx}}^{\mathrm{loc}} = 2E_{\mathrm{x}}^{\mathrm{loc}}$ *marks the case of equal localization strength per exciton.*

tion 2.2.2). The respective center-of-mass potentials V_{CM} for two quantum box radii $r_{\mathrm{box}}^{(1)} = 0.25\ a_{\mathrm{x}}$ and $r_{\mathrm{box}}^{(2)} = 1.0\ a_{\mathrm{x}}$ are depicted in Fig. 2.5 (solid curves, labeled with A). While the shape of the potential curve is independent of the depth V_{box} of the single-particle potential δV_a, the groundstate energy levels $E_{\mathrm{x}}^{\mathrm{loc}}$ and $E_{\mathrm{xx}}^{\mathrm{loc}}$ as well as their position relative to each other depend sensitively on this parameter.

Conversely to the model parameters r_{box} and V_{box}, the exciton localization energy $E_{\mathrm{x}}^{\mathrm{loc}}$ is a quantity directly observable experimentally. Therefore, this energy, calculated at the corresponding level of approximations, is chosen as reference for measuring the degree of the biexciton localization and used for scaling the abscissa in the figures. In Fig. 2.6, biexciton localization and binding energies $E_{\mathrm{xx}}^{\mathrm{loc}}$ and $E_{\mathrm{xx}}^{\mathrm{b}} = 2E_{\mathrm{x}} - E_{\mathrm{xx}}$, respectively, are plotted versus $E_{\mathrm{x}}^{\mathrm{loc}}$, varying the parameters of the quantum box in two ways.

First, variation of $V_{\rm box}$ at the selected radii $r^{(1)}_{\rm box}$ and $r^{(2)}_{\rm box}$ demonstrates how the biexciton localizes when its spatial extension is approximately equal or distinctly smaller than the characteristic width of $V_{\rm CM}$ (dashed curves). Second, keeping the potential depth $V_{\rm box} = 1.0\ Ry_{\rm x}$ fixed, the radius $r_{\rm box}$ was varied (solid curves). As long as the localization is weak, the biexciton is found to have a larger localization energy per exciton than the single exciton, despite of its larger spatial extension. (Notice the dotted line with $E^{\rm loc}_{\rm xx} = 2E^{\rm loc}_{\rm x}$ in Fig. 2.6.) Decomposing the various contributions, it holds $E^{\rm b}_{\rm xx} = E^{\rm b\,QW}_{\rm xx} + (E^{\rm loc}_{\rm xx} - 2E^{\rm loc}_{\rm x})$, where $E^{\rm b\,QW}_{\rm xx} = 2E^{\rm QW}_{\rm x} - E^{\rm QW}_{\rm xx}$ is the binding energy of the ideal QW. The increased line separation in the experiment is hence a consequence of the increased biexciton localization, while the exciton-exciton interaction energy remains practically unchanged. This fact can also be understood as an increased biexciton binding energy compared to the free QW biexciton, for which the solution of the finite-difference Schrödinger equation yields $E^{\rm b}_{\rm xx} = 3.81$ meV.

The asymptotic behaviour for $E^{\rm loc}_{\rm x} \to 0$ can be shown to be universal and independent of the details of the potential and the relative wavefunction: For any particle with mass M localized in a weak 2D potential $V(\mathbf{r})$ ($|V| \ll \hbar^2/(Ma^2)$ where a^2 is the area where V is significantly different from zero), it holds [90]

$$|E| \approx \frac{\hbar^2}{Ma^2} \exp\left[-\hbar^2/(M \int d^2r\, |V(\mathbf{r})|)\right]. \tag{2.22}$$

Since the weight functions $f_a(s)$ are normalized, the integral of the biexciton center-of-mass potential $\int d^2r |V(\mathbf{r})|$ is two times that of the exciton, so that the biexciton has not only twice the mass, but experiences twice the potential strength compared to the exciton, resulting in

$$|E^{\rm loc}_{\rm xx}| \sim |E^{\rm loc}_{\rm x}|^{1/4}. \tag{2.23}$$

Beyond this limit, the trends for the biexciton localization are directly related to the respective weight functions. For a given $E^{\rm loc}_{\rm x}$, the larger width of the biexciton function causes a decrease of $E^{\rm loc}_{\rm xx}$ when $r_{\rm box}$ becomes smaller. Increasing $V_{\rm box}$ at fixed $r_{\rm box}$, $E^{\rm loc}_{\rm xx}$ crosses the line $E^{\rm loc}_{\rm xx} = 2E^{\rm loc}_{\rm x}$ at $V_{\rm box} = 150\,$meV ($E^{\rm loc}_{\rm x} = 3.0\,$meV) for $r^{(1)}_{\rm box} = 0.25\,a_{\rm x}$ and at $V_{\rm box} = 26\,$meV ($E^{\rm loc}_{\rm x} = 8.5\,$meV) for $r^{(2)}_{\rm box} = 1.0\,a_{\rm x}$, respectively, and the range of enhanced biexciton localization ends. On the other hand, for relatively shallow quantum boxes with $V_{\rm box} \lesssim 1.0\ Ry_{\rm x}$, no crossover is found in the range of reasonable values of

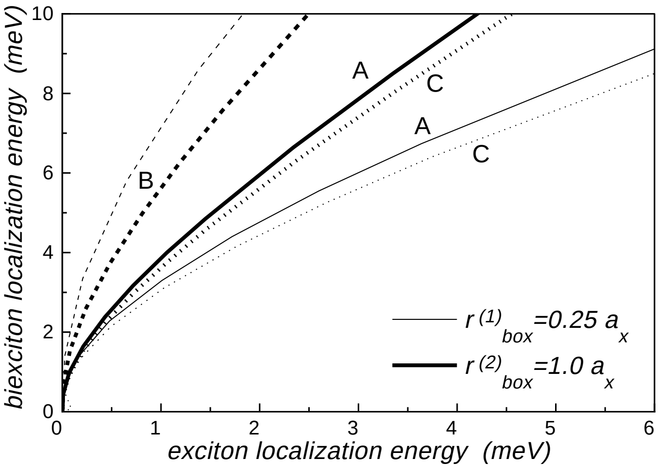

Figure 2.7: *Biexciton localization energies* $E_{\mathrm{xx}}^{\mathrm{loc}}$ *as functions of the exciton localization energy* $E_{\mathrm{x}}^{\mathrm{loc}}$ *in quantum boxes with* $r_{\mathrm{box}}^{(1)} = 0.25\,a_{\mathrm{x}}$ *and* $r_{\mathrm{box}}^{(2)} = 1.0\,a_{\mathrm{x}}$ *for the three biexciton models A, B, and C (see caption in Fig. 2.3).*

r_{box}. Evidently, the assertion that localization requires a particle size smaller than the characteristic potential extension, is incorrect.

Strictly speaking, the center-of-mass approach requires $E_{\mathrm{xx}}^{\mathrm{loc}} \ll E_{\mathrm{xx}}^{\mathrm{b}}$. It can be argued, however, that even the range $E_{\mathrm{xx}}^{\mathrm{loc}} \gtrsim E_{\mathrm{xx}}^{\mathrm{b}}$ can be covered in very good approximation. In the latter situation, the slight compression of the biexciton relative wavefunction caused by localization is compensated by the Coulomb repulsion of the equally charged particles so that its net change can be ignored.

2.3.2 Comparison of the Biexciton Models

Now we evaluate the two simplified versions of the QW biexciton relative wavefunction by comparing them with the rigorous treatment of the previous section. Figure 2.5 displays the respective exciton and biexciton center-of-mass potentials V_{CM} for the quantum box radii $r_{\mathrm{box}}^{(1)}$ and $r_{\mathrm{box}}^{(2)}$. As already demonstrated for the weight functions, the hole-hole separation ansatz introduced in section 2.2.4 reproduces the solution of the finite-difference Schrödinger equation very well. This is also true for the biexciton localization energies $E_{\mathrm{xx}}^{\mathrm{loc}}$ plotted versus $E_{\mathrm{x}}^{\mathrm{loc}}$ in Fig. 2.7. A qualitative deviation consists in a nonmonotonic behaviour of the potential curve for the narrower quantum box, caused by the sharper peak of the hole weight function f_h of this approximation. For $\sigma \ll 1$, V_{CM} is controlled by the shape of f_h. If the radius of the quantum box is now smaller than the effective hole radius in the free biexciton, given by the peak of f_h, the complex localizes with only one hole inside and the other hole outside the quantum box. While this is indeed the correct scenario for $\sigma \ll 1$, the finite-difference calculation demonstrates that the peak of f_h is less pronounced for the actual σ, and thus compensated by the contribution of the electron weight function.

The effective one-degree-of-freedom model yields results which differ substantially from the ones of the other approaches. While the failure of exponential weight functions is less severe for the single exciton, there are dramatic deviations in case of the biexciton (see Figs. 2.3 and 2.5). A consequence of the simplifications made by this model is an unrealistically strong constriction of the electrons and holes within the biexciton, yielding already a too large binding energy of $E^{\mathrm{b}}_{\mathrm{xx}} = 6.28\,\mathrm{meV}$ for the QW. The same holds for the localization energies, as can be seen in Fig. 2.7.

2.4 Summary

The above study has confirmed the localization of biexcitons. In the limit of weak localization, the localization energy is more than twice as large as for the single exciton because of the larger biexciton mass and the stronger center-of-mass potential. Therefore, with increasing temperature, first the excitons are removed from their localization sites, while localized biexcitons survive up to markedly higher levels. Weak localization of the biexciton significantly increases the biexciton binding energy, given by the separation of the exciton and biexciton PL features, without altering the exciton-exciton interaction energy. Stronger localization, as for instance in intentionally made quantum dots, does not necessarily mean that the stability of the biexciton is further enhanced. For the (Zn,Cd)Se/ZnSe model structure studied here, the Coulomb repulsion of the heavier holes becomes increasingly dominant in the inter-particle interaction, so that the biexciton binding energy starts to decrease. This case, where the center-of-mass approach begins to fail, is investigated in the next chapter. The adiabatic-like hole-hole separation ansatz turned out to provide a useful approximation scheme for calculating the QW biexciton state.

Table 2.2: *Calculation parameters for a $Zn_{0.8}Cd_{0.2}Se/ZnSe$ QW.*

Ry_{x} [meV]	20.3
a_{x} [nm]	4.0
m_e/m_o [a]	0.15
m_h/m_o [a]	0.5
ε [b]	8.8
ΔE_{g} [meV] [a]	260
$\Delta E_{\mathrm{c}}/\Delta E_{\mathrm{g}}$ [a]	0.75

[a] Ref. [97]

[b] Ref. [62]

Chapter 3

Localization in Strong Compositional Inhomogeneities

3.1 Introduction

The extreme difference in the photoluminescence linewidth between (Zn,Cd)Se/ZnSe and (In,Ga)N/GaN QWs raises the question about the character of the underlying potential fluctuations and the nature of the recombining excitonic complexes in these ternary QW materials. Assuming uncorrelated alloy fluctuations to be the only origin of localization, it can be demonstrated agreement with experimentally observed Stokes shifts and linewidths as well as biexciton binding energies only for (Zn,Cd)Se QWs, whereas for (In,Ga)N, the results are about one order of magnitude too small [183]. It is assumed that these large inhomogeneous broadenings are related to strong potential fluctuations produced by the compositional inhomogeneities found in spatially resolved investigations [119, 32, 106, 171, 48, 162, 55]. These nm-sized regions of phase-separated indium, resembling self-assembled quantum dots, may be capable of localizing more carriers than the potential fluctuation present in QWs made of other material systems.

In this chapter, a theoretical study of localized excitons, biexcitons, and higher exciton complexes with up to four electrons and holes is presented. The spectral width of the successive optical recombination spectrum of localized multi-excitons is considered to estimate the contribution to the total emission linewidth. To be able to investigate also the strong localization regime, where the procedure of separations described in chapter 1 is not applicable, the multi-particle Schrödinger equation (1.1) is treated in the framework of a two-component effective-mass density functional theory in local density approximation [141, 183]. To get a solution of the Kohn-Sham system of equations a special iteration technique is applied [77], incorporated in the finite volume simulation tool ToSCA [2].

3.2 Theory

In the density functional theory, the ground state energy of system (1.1) can be decomposed into four main contributions

$$E = T_{\mathrm{s}} + V_{\mathrm{s}} + E_{\mathrm{Coul}} + E_{\mathrm{xc}}\,. \tag{3.1}$$

The kinetic and potential single particle energies are

$$\begin{aligned} T_{\mathrm{s}} &= \int dV \sum_{a=e,h} \frac{\hbar^2}{2m_a} \sum_k f_{ak} \left|\nabla \psi_k^a(\vec{\mathrm{r}}\,)\right|^2 \quad \text{and} && (3.2)\\ V_{\mathrm{s}} &= \int dV \sum_{a=e,h} V_a(\vec{\mathrm{r}}\,) n_a(\vec{\mathrm{r}}\,)\,, && (3.3) \end{aligned}$$

respectively. k labels the set of quantum numbers. Here, the kinetic energy T_{s} as well as the particle densities

$$n_a(\vec{\mathrm{r}}\,) = \sum_k f_{ak} \left|\psi_k^a\,(\vec{\mathrm{r}}\,)\right|^2 \tag{3.4}$$

contain single-particle orbitals $\psi_k^a(\vec{\mathrm{r}}\,)$ and occupation numbers f_{ak}. The potentials $V_a(\vec{\mathrm{r}}\,)$ $(a = e, h)$ are the external single-particle potentials (1.2) comprising QW and localization potential. The Coulomb contribution to the total energy is

$$E_{\mathrm{Coul}} = \int dV \frac{\varepsilon\varepsilon_o}{2} \left(\nabla\phi(\vec{\mathrm{r}}\,)\right)^2 . \tag{3.5}$$

The electrostatic potential ϕ herein solves the Poisson equation

$$-\nabla\varepsilon\varepsilon_o\nabla\phi(\vec{\mathrm{r}}\,) = \sum_{a=e,h} q_a n_a(\vec{\mathrm{r}}\,). \tag{3.6}$$

ε is the relative dielectric constant of the semiconductor, and $\mathrm{q}_e = -e$ and $\mathrm{q}_h = +e$ is the charge of an electron and a hole, respectively.

For the exchange-correlation energy, the local density approximation is adopted

$$E_{\mathrm{xc}} = \int dV \epsilon^{\mathrm{xc}}(n_e(\vec{\mathrm{r}}), n_h(\vec{\mathrm{r}})), \tag{3.7}$$

where $\epsilon^{\mathrm{xc}}(n_e, n_h)$ denotes the exchange-correlation energy of a homogeneous electron-hole plasma with corresponding densities. The exchange contribution is

$$\epsilon^{\mathrm{x}}(n_e, n_h) = -3\left(\frac{3}{4\pi}\right)^{2/3} \sum_a \left(\frac{1}{\nu_a}\right)^{1/3} V_{\mathrm{x}}^{1/3}\, Ry_{\mathrm{x}}\, n_a^{4/3} \tag{3.8}$$

where $\nu_a = \min(2, N_a)$ is the number of spin components occupied by particle sort a, N_a is the total number of particle sort a, $V_{\mathrm{x}} = 4\pi a_{\mathrm{x}}^3/3$ is the exciton Volume, $a_{\mathrm{x}} = \hbar^2 4\pi\varepsilon\varepsilon_o/e^2\mu$ is the exciton Bohr radius, $Ry_{\mathrm{x}} = \hbar^2/(2\mu a_{\mathrm{B}}^2)$ is the exciton Rydberg, and $\mu = m_e m_h/(m_e + m_h)$ is the reduced mass. For the correlation contribution, no exact expression is available. We use

$$\epsilon^{\mathrm{c}}(n_e, n_h) = -\beta_e n_e^{7/6} - [\beta_{\mathrm{tot}} - \beta_e - \beta_h] \cdot (n_e n_h)^{7/12} - \beta_h n_h^{7/6}, \tag{3.9}$$

where

$$\beta_a = 0.1\, Ry_{\mathrm{x}}\, V_{\mathrm{x}}^{1/6}\, \nu_a^{1/3} \sqrt{\frac{m_a}{\mu}} \quad \text{and} \tag{3.10}$$

$$\beta_{\mathrm{tot}} = 0.756\, Ry_{\mathrm{x}}\, V_{\mathrm{x}}^{1/6} \left(0.8 + \sqrt{\frac{m_e^2 + m_h^2}{2 m_e m_h}}\right). \tag{3.11}$$

These formulae combine the analytic dependencies on the densities and effective masses used in Ref. [182] with the dependence on the numbers ν_a of spin components proposed in Ref. [181].

The Kohn-Sham equations are effective single-particle Schrödinger equations, the solutions of which are the single-particle orbitals ψ_k^a minimizing the total energy functional (3.1):

$$\left\{-\frac{\hbar^2}{2}\nabla\frac{1}{m_e}\nabla + V_e^{\mathrm{KS}}(\vec{\mathrm{r}})\right\}\psi_k^e(\vec{\mathrm{r}}) = \epsilon_k^e \psi_k^e(\vec{\mathrm{r}}) \tag{3.12}$$

$$\left\{-\frac{\hbar^2}{2}\nabla\frac{1}{m_h}\nabla + V_h^{\mathrm{KS}}(\vec{\mathrm{r}})\right\}\psi_k^h(\vec{\mathrm{r}}) = \epsilon_k^h \psi_k^h(\vec{\mathrm{r}}). \tag{3.13}$$

The Kohn-Sham potentials $V_a^{\mathrm{KS}}(\vec{\mathrm{r}})$ $(a = e, h)$ contain the external single-particle potentials $V_a(\vec{\mathrm{r}})$, the Coulomb potential $\phi(\vec{\mathrm{r}})$ and an exchange-correlation potential $V_a^{\mathrm{xc}}(\vec{\mathrm{r}})$

$$V_a^{\mathrm{KS}}(\vec{\mathrm{r}}) = V_a(\vec{\mathrm{r}}) + q_a\phi(\vec{\mathrm{r}}) + V_a^{\mathrm{xc}}(\vec{\mathrm{r}}) \qquad \text{with} \qquad V_a^{\mathrm{xc}}(\vec{\mathrm{r}}) = \frac{\partial \epsilon^{\mathrm{xc}}(n_e, n_h)}{\partial n_a}. \tag{3.14}$$

The occupation numbers can be obtained by filling the particles into the energetically lowest states (up to 2 particles per state due to spin degeneracy), until the given total particle number N_a is reached

$$\sum_k f_a(\epsilon_k^a) = N_a \qquad (a = e, h). \tag{3.15}$$

The shape of clusters with enhanced indium content in a (In,Ga)N/GaN QW is not known exactly and may vary considerably from site to site. For this calculation, the external single-particle potentials $V_a(\vec{\mathrm{r}})$ are again modeled by the cylindrical quantum box, used already in chapter 2 for the investigation of the weak localization limit. However, no separation of the motion along the z-direction is made here. A fully 3D calculation is necessary since the in-plane localization energy can now be in the same range like the subband level distance of the ideal QW confinement. Thus, no decomposition of the single-particle potentials in QW and remaining term is made:

$$V_a(\vec{\mathrm{r}}_i) = \begin{cases} -\xi_a V_{\mathrm{box}} & \text{if} \quad -d_{\mathrm{QW}}/2 < z < d_{\mathrm{QW}}/2 \quad \text{and} \quad r_i \le r_{\mathrm{box}} \\ 0 & \text{if} \quad -d_{\mathrm{QW}}/2 < z < d_{\mathrm{QW}}/2 \quad \text{and} \quad r_i > r_{\mathrm{box}} \\ \Delta E_a & \qquad\qquad\qquad \text{else} \end{cases}. \tag{3.16}$$

The surrounding QW material $\mathrm{In}_x\mathrm{Ga}_{1-x}\mathrm{N}$ is assumed to have an indium content of $x = 0.2$ (for further material parameters see Table 3.1). No polarization fields are considered in this calculation.

For a detailed introduction to the density functional theory see e.g. Refs. [53, 49, 130, 170].

3.3 Results

3.3.1 Exciton Localization

For the free exciton ($V_{\mathrm{box}} = 0$) in a 2 nm wide QW, the calculation yields a binding energy $E_{\mathrm{x}}^{\mathrm{b}} = 41\,\mathrm{meV}$. Since—in contrast to the model parameters r_{box} and V_{box}—the exciton localization energy $E_{\mathrm{x}}^{\mathrm{loc}} = E_{\mathrm{x}}(V_{\mathrm{box}} = 0) -$

$E_{\mathrm{x}}(V_{\mathrm{box}} \neq 0)$ is an observable quantity, it is chosen to be the relevant parameter for the description of dependencies on localization strength and therefore used for scaling the abscissa in the figures. Varying r_{box} and V_{box} between 0.6–3 nm and 0–1 eV (corresponding to the maximum gap difference between $\mathrm{In}_{0.2}\mathrm{Ga}_{0.8}\mathrm{N}$ and InN) respectively, exciton localization energies in the experimentally observed region between 100 and 300 meV are obtained (see abscissa in Fig. 3.1). Figure 3.1 a shows the influence of the quantum box confinement on the exciton binding energy $E_{\mathrm{x}}^{\mathrm{b}}$. As expected, the increase of $E_{\mathrm{x}}^{\mathrm{b}}(E_{\mathrm{x}}^{\mathrm{loc}})$ is steeper in case of a smaller box which restricts the spatial extension of the Kohn-Sham orbitals more effectively than a larger localization site with the same localization energy. The restriction of kinetic freedom results in a deeper state in the attractive electron-hole Coulomb potential, reflected in a higher binding energy. The same effect can be seen in Fig. 3.1 a for a decreasing width of the QW and a constant box radius.

3.3.2 Biexciton Localization

Concerning the biexciton, it can be seen in Fig. 3.1 b, that the dependence of the binding energy $E_{\mathrm{xx}}^{\mathrm{b}}$ on $E_{\mathrm{x}}^{\mathrm{loc}}$ varies drastically for different r_{box}. The commonly expected monotonic increase, which results from a dot-like confinement with infinite barriers, occurs only in case of large boxes with $r_{\mathrm{box}} > 1$ nm. If the quantum box is smaller, the biexciton binding becomes weaker first. This is caused by the Coulomb repulsion of the two holes, which prevents the hole state[1] from localizing as it does in a single exciton. However, this can occur only if $\sigma = m_e/m_h \neq 1$, because otherwise, electrons and holes would have identical orbitals, and the hole-hole repulsion would be screened completely by the electrons (see the dotted line with pearls in Fig. 3.1 b). The regime of very strong localization, where $E_{\mathrm{xx}}^{\mathrm{b}}$ saturates, is not reached for $V_{\mathrm{box}} < 1$ eV.

Inspecting closer the limit $V_{\mathrm{box}} \to 0$, it is found that the calculated particle densities remain concentrated in a finite region with dimensions of the order of the exciton Bohr radius. Because this self-localization is an artifact of the local density approximation, the weak localization limit was additionally investigated perturbatively using a center-of-mass separation ansatz. This is outlined in detail in chapter 2. As it can be seen in Fig. 3.2, this ap-

---

[1] Due to the spin degeneracy of the orbitals, there is only one hole orbital and one electron orbital even in case of a biexciton.

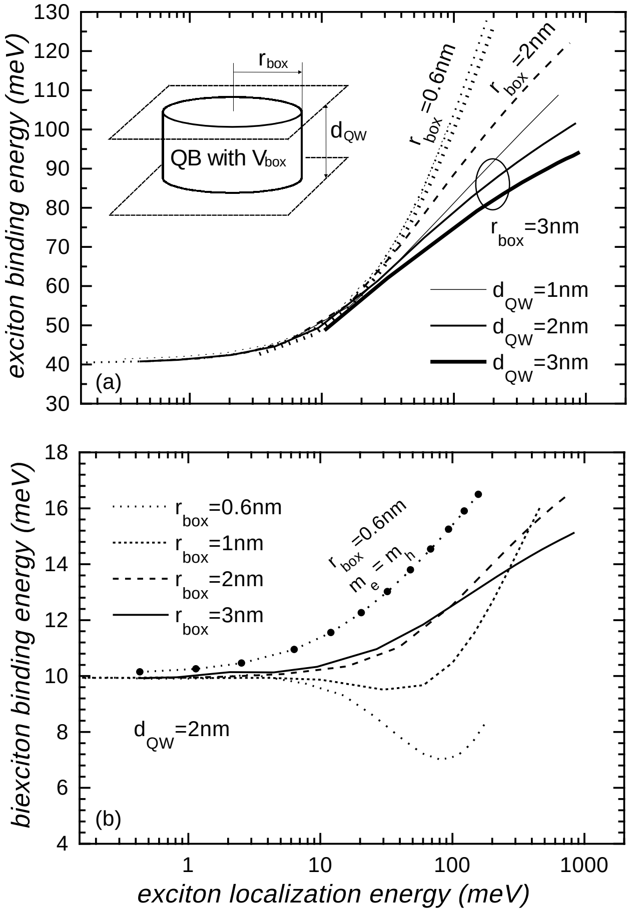

Figure 3.1: *Binding energy of a localized exciton (a) and biexciton (b) as a function of the exciton localization energy in a quantum box QB (see inset in Fig. a) within a $In_{0.2}Ga_{0.8}N/GaN$ QW of width d_{QW}. The doted line with pearls in Fig. b is the result for a biexciton with equal electron and hole masses in a small box (note the completely different behaviour in case of different masses).*

proach reveals enhanced biexciton localization with respect to the exciton in the weak localization limit. As already described in chapter 2, the reason for this is the universal behaviour of localization in weak 2D potentials [90], yielding $|E_{\mathrm{xx}}^{\mathrm{loc}}| \sim |E_{\mathrm{x}}^{\mathrm{loc}}|^{1/4}$. This result is not produced by the density functional calculation in local density approximation, which instead yields a

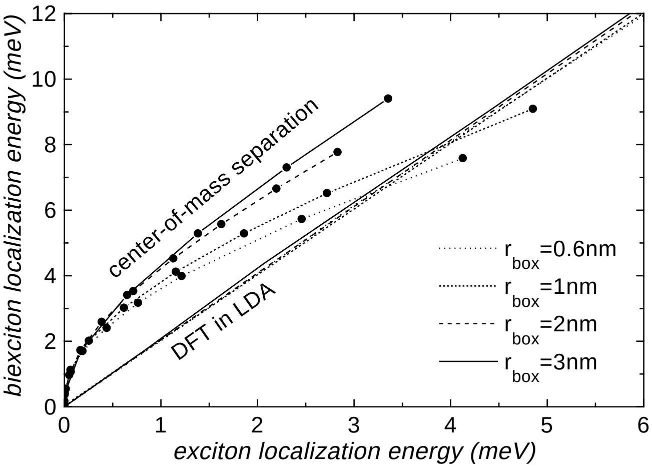

Figure 3.2: *Biexciton localization energy in dependence on the exciton localization energy for various box radii* r_{box} *in the weak localization regime. Comparison between the results of a DFT calculation in LDA and the center-of-mass separation ansatz, outlined in chapters 1 and 2.*

biexciton localization being always twice as large as the exciton localization due to the artificial self-localization effect of a free particle (see Fig. 3.2).

3.3.3 Multi-Exciton Localization

Quantum boxes with exciton localization energies of several hundred meV may be able to localize even higher exciton complexes $X_{n>2}$. For the calculation of complexes with more than two electrons or holes, the next higher Kohn-Sham orbitals ψ_k^a have to be filled. It turns out that those with one higher angular quantum number have lower energy than those with one higher radial quantum number. Consequently, for the complexes X_3 and X_4 the former have to be considered. Since the splitting between the uppermost valence subbands is small in this situation, a four-fold degenerated valence band is assumed. The calculation of the smallest energy required to remove at least one exciton from the complex indicates stability of multi-excitons X_3 and X_4 already for $E_{\text{x}}^{\text{loc}} \approx 50\,\text{meV}$. This is displayed in Fig. 3.3 a.

The optical transition energies, plotted in Fig. 3.3 b, lie below the single exciton transitions for all multi-excitons because selection rules allow only transitions between the lowest shells, leaving an excited final state behind.

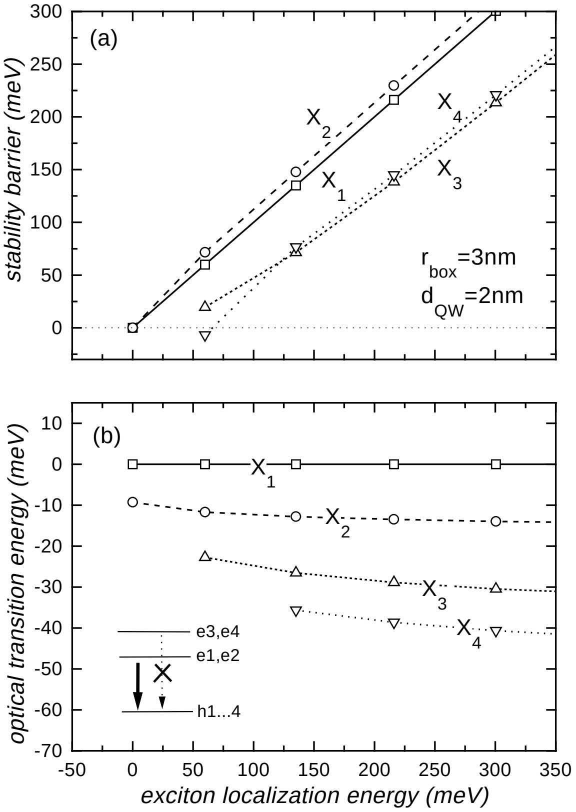

Figure 3.3: *Stability barrier (smallest energy required to remove at least one exciton from the complex) and optical transition energies (relative to the exciton transition) of localized multi-excitons $X_{n\leq 4}$ in dependence on the exciton localization energy.*

These excited final states have been calculated keeping lower orbitals unoccupied. Since the spectral distances between these transitions of about $10-15\,\mathrm{meV}$ are small compared to the linewidths experimentally observed in (In,Ga)N-based structures, it will be necessary to apply spatially resolved "single-dot" spectroscopy to resolve them in a high-excitation experiment.

3.4 Summary

In conclusion, a density functional calculation in local density approximation demonstrated that multi-exciton states at least up to X_4 may localize in nm-scale potential boxes caused by indium phase-separation in an (In,Ga)N/GaN QW. The successive recombination of a localized X_4 results in an emission spectrum of four lines separated by about $10 - 15\,\text{meV}$ in the example presented here.

Table 3.1: *Calculation parameters used in this chapter.*

Parameter	GaN	InN	$\text{In}_x\text{Ga}_{1-x}\text{N}$
E_g [eV]	3.4	1.95	
b (bowing) [eV] [a]			1.0
m_e/m_o [b]	0.2	0.2	
m_h/m_o [c]	0.8	0.8	
ε	9.5	9.5	
$\Delta E_\text{c}/\Delta E_\text{v}$ [d]			70/30

[a] Refs. [132, 153, 116, 126, 179]
[b] Refs. [80, 163, 98]
[c] Refs. [80, 163, 98, 185, 128, 40]
[d] Refs. [44, 174, 99]

Chapter 4

Polarization Charge Screening and Indium Surface Segregation in (In,Ga)N/GaN Quantum Wells

4.1 Introduction

The fact that the optical transition energy in (In,Ga)N/GaN QW structures can not be described as a function of only indium content and well width is reflected also in the large scatter of the value for the bowing parameter for the band gap energy of (In,Ga)N found in literature [132, 153, 116, 126, 154, 175, 145, 105, 166, 129]. The problem is either the lack of knowledge about the exact structure of the inhomogeneities and the mutual interaction with the strong polarization fields or the existence of further parameters influencing the transition energy but probably it is a result of even both aspects. It is hardly possible to disentangle the contributions of inhomogeneities on the one hand and polarization fields on the other hand to transition energy shifts observed when changing e.g. doping level or excitation density [110, 76]. In publications which investigate theoretically the influence of polarization fields on optical properties, a homogeneous composition of the (In,Ga)N alloy is usually assumed [110, 76, 165, 131, 64, 74, 150, 54, 149]. The method of solving self-consistently the Poisson-Schrödinger system of equations has been applied for various structures [131, 39, 150, 54, 149]. This method is able to qualitatively explain shifts of transition energy and modifications of carrier lifetime by screening of polarization charges in highly doped samples or under high excitation. However, the impact of the surface polarization charge on the transition energy, evident in the case of samples with a thin cap layer which are typically designed for optical excitation experiments, has not yet been discussed.

In this chapter, a detailed description and analysis of the overall situation of macroscopic polarization fields along the growth direction in (In,Ga)N/GaN SQWs and MQWs is given for various sample designs with a thin cap layer. Based on a self-consistent solution of the Schrödinger-Poisson system of equations, the dependence of optical transition energy and matrix element on several substantial sample parameters is systematically investigated under consideration of spontaneous and strain-induced polarization fields. In-plane inhomogeneities are neglected. The results demonstrate that optical transition energy and matrix element depend sensitively on the design of the structure. A mechanism for the occurrence of shoulders or side maxima in the optical transition spectrum of MQWs is discussed. The time dependence of decay and transition energy shift due to excitation-induced screening of the polarization fields under pulsed high excitation is calculated. Furthermore, the combined impact of polarization fields and indium surface segregation is investigated.

The chapter is organized as follows. The theoretical procedure and the range of parameters are given in section 4.2. The results of the self-consistent calculations for different segregation profiles of an otherwise fixed SQW are discussed in section 4.3. Section 4.4 follows with a detailed analysis of the electric field situation of SQWs and MQWs with a fixed representative segregation profile for various experimentally relevant geometries. Different physical situations are discussed with an emphasis on the screening of polarization fields. To allow simple estimates for a given sample, analytic approximations are derived for the field profile in all cases. At the end of section 4.4 the situation in MQWs is analysed and discussed. In section 4.5 higher excitation densities are simulated and the influence of the screening on the PL transient is investigated. A summary is given at the end of the chapter.

4.2 Theory

The mutual interaction of polarization fields and occupied electronic states can be described by the Schrödinger-Poisson system of equations. The energies ϵ_k^a and wave functions $\varphi_k^a(z)$ of the electron and hole subbands are determined from the single-particle effective-mass Schrödinger equations

$$\left[-\frac{\hbar^2}{2m_a}\Delta_z + \tilde{V}_a^{\mathrm{QW}}(z)\right]\varphi_k^a(z) = \epsilon_k^a\,\varphi_k^a(z) \quad (a = e, h) \tag{4.1}$$

with the potentials

$$\tilde{V}_a^{\mathrm{QW}}(z) = V_a^{\mathrm{QW}}(z) + q_a\,\phi(z)\,. \tag{4.2}$$

k labels the subbands, $q_e = -e$ and $q_h = +e$ denote the electron and hole charges, respectively. Here, $V_a^{\mathrm{QW}}(z)$ describes only the band edge discontinuities according to equation (1.10) without a contribution of the polarization. The electrostatic term $q_a\,\phi(z)$ comprises the polarization charges $\rho_{\mathrm{P}}(z)$ according to equation (1.15) and screening due to many particle effects. All charge densities of the system act as sources of the electrostatic potential $\phi(z)$ according to the Poisson equation

$$\Delta_z\phi(z) = -\frac{e\,[n_h(z) - n_e(z) + N_{\mathrm{D}}] + \rho_{\mathrm{P}}(z)}{\varepsilon\varepsilon_o}\,. \tag{4.3}$$

The particle densities are given by

$$n_a(z) = N_a^{\mathrm{2D}}\sum_k |\varphi_k^a(z)|^2 \ln\left(1 + e^{(E_{\mathrm{F}} - \epsilon_k^a)/kT}\right), \tag{4.4}$$

where E_{F} is the Fermi energy and $N_a^{\mathrm{2D}} = m_a\,kT/\pi\hbar^2$ is an effective 2D density of states. $T = 300\,\mathrm{K}$ is used in all calculations presented below, corresponding to device applications at room temperature. Some calculations have been redone for lower temperatures. Although the distribution of carriers among the subbands changed noticeably, the total sheet densities in the QWs were less sensitive and the global field profile changed only slightly.

As the densities depend in turn on the subband energies and wave functions, the basic equations (4.1) to (4.4) become coupled and have to be solved self-consistently. This calculation was performed iteratively, using the 1D Poisson-Schrödinger solver of G. Snider [3, 159, 167]. The polarization charges were simulated by additional, fully ionized dopants, discretized in 1 Å wide steps on the numerical space grid. The Schrödinger equation is solved only in a limited region that includes the cap layer, the QW stack, and some ten nanometers of the buffer. Vanishing of the wave function $\varphi(z)$ is used as boundary condition on both sides. The rest of the buffer layer is treated as a bulk material. There, only the Poisson equation is solved with the expression

$$n_a(z) = N_a^{\mathrm{3D}}\, \mathcal{F}_{1/2}\left(\frac{E_{\mathrm{F}} - \epsilon_a - q_a\phi}{kT}\right) \tag{4.5}$$

for the particle densities on the right hand side. $\mathcal{F}_{1/2}$ is the Fermi integral with index 1/2 and $N_a^{\mathrm{3D}} = 2(2\pi m_a kT/h^2)^{3/2}$. The buffer layer is assumed to be very thick compared with the heterostructure so that the influence of the substrate interface is negligible.

During the self-consistency run only sufficiently occupied subbands are accounted for. However, to obtain optical transition energies and overlap integrals $\int dz\, \varphi_e^*(z)\, \varphi_h(z)$, unoccupied states have to be considered, too. Therefore, these additional subband energies and wave functions were calculated by a post-processing procedure. Restricting ourselves to confined states only, the Schrödinger equation is solved for each QW separately using again the method of finite differences. This simulates only the situation of low excitation density, where the band edge alignment is not altered by photoexcited carriers. The calculation of the transition energy includes furthermore a perturbative correction due to exciton binding according to equation (A.12) [93, 133]. Above the Mott transition, the exchange contribution to the band gap renormalization (as a consequence of a high n-type doping) is considered as

$$\Delta E_e^{\mathrm{x}} = \int dz\, V_e^{\mathrm{x}}(n_e)|\varphi_e(z)|^2 \tag{4.6}$$

where $V_e^{\mathrm{x}}(n) = \partial\epsilon^{\mathrm{x}}/\partial n$ and $\epsilon^{\mathrm{x}}(n)$ is given by equation (3.8). The Mott transition is assumed to occur when the band gap renormalization in terms of ΔE_e^{x} equals the exciton binding energy.

In the following, wurtzite $\mathrm{In}_x\mathrm{Ga}_{1-x}\mathrm{N}$/GaN SQWs and MQWs with a thickness of $d_{\mathrm{QW}} = 3\,\mathrm{nm}$ are considered, as widely used in LEDs and LDs. The growth axis is the crystallographic c-axis. The QWs are assumed to be pseudomorphically grown on a relaxed GaN buffer and capped with a

GaN layer. Three representative indium concentrations $x = 0.05$, 0.1, and 0.2 will be compared. A constant donor concentration N_D throughout all layers is assumed. The cases of low, medium, and high doping are considered, represented by $N_\mathrm{D} = 5{\cdot}10^{16}\,\mathrm{cm}^{-3}$, $5{\cdot}10^{17}\,\mathrm{cm}^{-3}$, and $5{\cdot}10^{18}\,\mathrm{cm}^{-3}$, respectively.

4.3 Indium Surface Segregation

Due to the large difference between the free binding enthalpies of GaN and InN,[1] a strong tendency to indium surface segregation during the growth of (In,Ga)N is expected [81, 91, 122, 28, 50, 18, 88]. This effect is well investigated for comparable arsenide heterostructures [113, 114, 96, 115, 57, 102, 78, 177, 83, 134, 148, 60]. Segregation limits the indium incorporation and smoothes the structural transitions between well and barrier material. As a result, the profile of incorporated indium is not rectangularly shaped as usually assumed for calculating subband states and optical properties. Thereby, the segregation redistributes the polarization charge into a wider space region, so that the resultant electric field may be much different from that for ideal interfaces. It is however rather difficult to measure the actual distribution of indium along the growth direction [81, 50]. In most cases only the nominal integral indium content of one QW-barrier-period and the well and barrier thicknesses in a MQW are known from the growth process or from experiments like e.g. x-ray diffraction measurements. In this section, the consequences of non-rectangularly shaped indium profiles in the presence of polarization fields are discussed.

To model the indium profile, several suggestions have been made in literature [81, 113, 114, 96, 115, 57], most of them for arsenides [113, 114, 96, 115, 57]. Here, error-functions are used with segregation lengths L_si and L_sn for the inverted (InGaN-on-GaN) and the normal (GaN-on-InGaN) interface, respectively,

$$x(z_\mathrm{i} \pm \delta) = \begin{cases} 0 & \delta < 0 \\ x_o \,\mathrm{erf}\left(\frac{\delta}{L_\mathrm{si}}\right) & 0 \le \delta < d_\mathrm{QW} \\ x_o \,\mathrm{erf}\left(\frac{d_\mathrm{QW}}{L_\mathrm{si}}\right) \left[1 - \mathrm{erf}\left(\frac{\delta - d_\mathrm{QW}}{L_\mathrm{sn}}\right)\right] & d_\mathrm{QW} \le \delta \,, \end{cases} \tag{4.7}$$

---

[1] The difference between the free binding enthalpies of InN and GaN is about 10 kcal/mol [91], that is about 3 kcal/mol more than for the corresponding arsenides, where segregation is an already well investigated phenomenon.

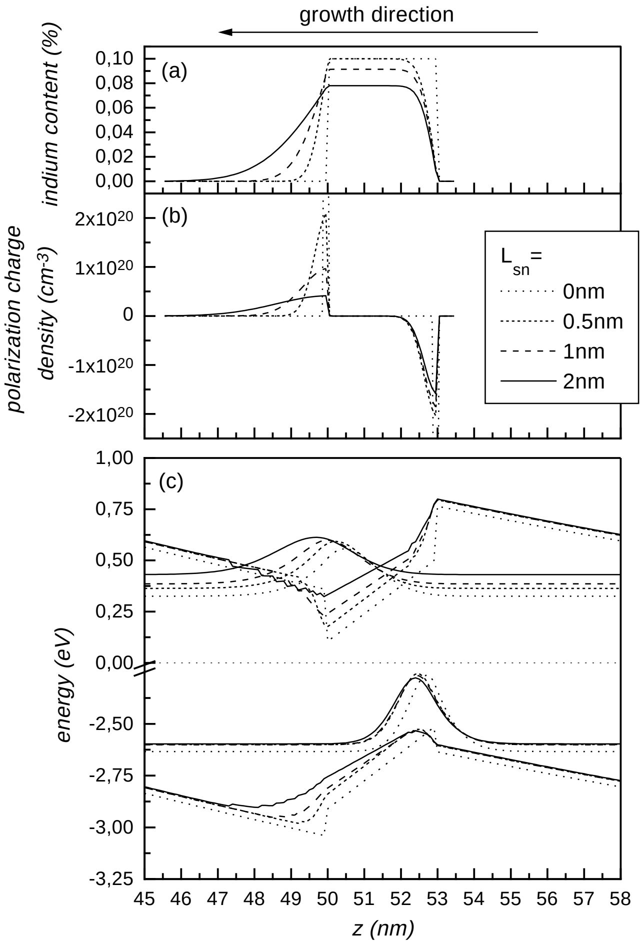

Figure 4.1: *(a) Indium profile, (b) polarization charge density, (c) self-consistently calculated band edge alignments and subband functions of a Ga-face grown 3 nm $In_{0.1}Ga_{0.9}N/GaN$ SQW with a background donor density of $N_D = 5 \cdot 10^{17}$ cm^{-3} and a 50 nm cap layer for different indium segregation profiles. The segregation length at the inverted interface is 0.5 nm, that at the normal interface is varied as indicated in the legend.*

where z_i denotes the position of the inverted interface and δ is the distance from z_i in growth direction. Accordingly, the positive sign on the left side holds for N-face material and the negative one for Ga-face material. This accounts for the different orientations of the z-axis, always chosen along the spontaneous polarization vector, i.e. in $[000\bar{1}]$-direction. The parameter x_0 is used to set the mean indium content $\int d\delta\, x(z_\mathrm{i} \pm \delta)/(d_\mathrm{QW} + d_\mathrm{B})$ to the desired value.

There is experimental indication for an asymmetry of the segregation length at the two interfaces with respect to growth direction [81, 88]. For arsenides, this is confirmed experimentally in several different ways [115, 57, 83, 134, 148, 60] and can be explained by a local equilibrium model for the growth process [115]. In general, the segregation length of the weaker bound III-component in ternary III-V-compounds is known to be a function of growth parameters like the III/V ratio and the substrate temperature [113, 114, 96, 115, 57, 102, 78, 177]. Since no values for L_si and L_sn for (In,Ga)N/GaN heterostructures are available from experiment, a reasonable choice was tried to be made, keeping L_si at 0.5 nm and varying L_sn from 0.5 nm to 2 nm (see Fig. 4.1 a). The integral indium content was kept fixed. The calculation was executed for a $d_\mathrm{QW} = 3\,\mathrm{nm}$ SQW, scanning the whole range of parameters given in section 4.2. As an example, indium profiles (a), polarization charge densities (b), self-consistently calculated band edge profiles and subband functions (c) for a Ga-face grown SQW with $x = 0.1$ and a 50 nm cap layer are displayed in Fig. 4.1.

In case of weak and symmetric segregation ($L_\mathrm{si} = L_\mathrm{sn} < d_\mathrm{QW}$), the polarization field inside the well remains nearly unchanged (dotted and short-dashed lines in Fig. 4.1 c are parallel inside the well) and the transition energies are only slightly changed. A small blueshift as well as redshift can occur, depending on the specific set of parameters. Electron and hole wavefunctions are somewhat shifted to growth direction, but the overlap is hardly modified.

A clear blueshift is obtained with increasing L_sn. It reaches about 30 meV, 60 meV, and 100 meV for the compositions $x = 0.05$, 0.1, and 0.2, respectively, in case of the largest segregation length $L_\mathrm{sn} = 2\,\mathrm{nm}$. This segregation-induced correction compensates up to one third of the corresponding quantum confined Stark shift of 90 meV, 210 meV, and 470 meV, respectively, for the rectangular QW with $N_\mathrm{D} = 5{\cdot}10^{16}\mathrm{cm}^{-3}$. Two combined effects contribute to this behaviour. First, the band gap energy within the QW increases because the indium profile becomes not only broader but also flatter in order to conserve the total amount of incorporated indium. Second, the flattening of the profile is accompanied by a reduction of the strain. Hence, the amount of polarization charges at the interfaces drops down. This effect is clearly observable in Fig. 4.1 b as a reduction of the amplitude of the charge density profile at the inverted interface. As a consequence, the field strength in the

QW decreases, reducing the quantum confined Stark shift.

For ideal interfaces, a reduced polarization field would also raise the electron-hole overlap. On the contrary, segregation results in a significant reduction of the overlap down to approximately a factor 0.2 for the highest investigated indium content of $x = 0.2$. Although the spatial extensions of the subband functions increase in the present case, the overlap is reduced due to a counteracting increase of the separation between electrons and holes. Because of the asymmetry of the segregation lengths at the two interfaces, the shift of the electron wavefunction towards the surface is larger than the shift of the hole wavefunction (see Fig. 4.1 c).

Concluding so far, the optical transitions are blueshifted with increasing indium surface segregation in the considered 3nm wide SQWs. This blueshift compensates up to one third of the redshift from the quantum confined Stark effect. It is accompanied by a further reduction of the oscillator strength due to the asymmetry of the segregation lengths. In the next section, different positions of SQW and MQW structures are considered. For reasons of practicability, the further calculations are carried out with a fixed choice of $L_{\mathrm{si}} = 0.5\,\mathrm{nm}$ for the inverted and $L_{\mathrm{sn}} = 1\,\mathrm{nm}$ for the normal interface, representing a lower limit of the segregation.

4.4 Polarization Charge Screening

The electric field generated by the polarization charges ρ_{P} is modified by fields caused by mobile carriers and dopant space charges according to the Poisson equation (4.3). Therefore, the optical properties of a QW do not only depend on its local composition but also on the global distribution of polarization and screening charges. In this section, the screening situation in different types of heterostructures is studied. Because III-nitrides tend to exhibit n-type conductivity, only this case is considered in the following.

4.4.1 Homogeneous GaN slab

It is useful to start with the most simple case, a layer of homogeneous, unstrained GaN. There, the spontaneous polarization causes surface charge densities of about $\pm 0.03\,\mathrm{C/m^2}$. Without screening, these charges would cause a voltage drop across a $1\,\mu\mathrm{m}$ thick layer as large as 350 V. However, it is well known that screening by mobile carriers reduces this voltage down to

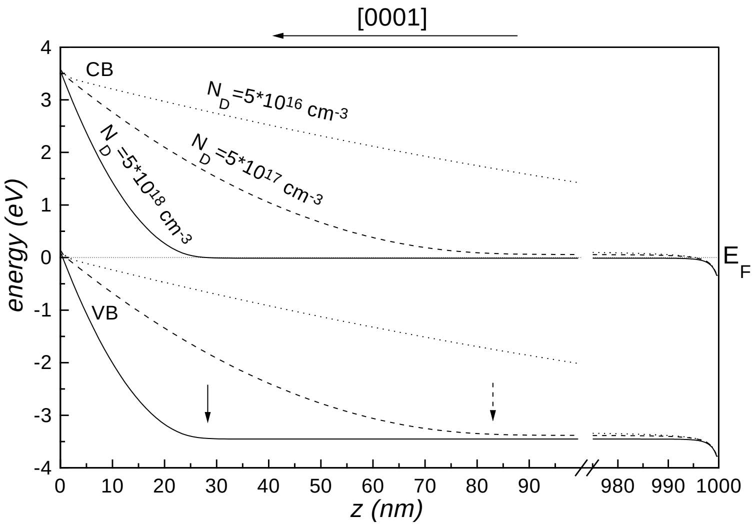

Figure 4.2: *Band edge alignment along the c-axis of a bare 1 μm thick GaN layer for several background donor densities. The Ga-face is at the origin of the abscissa and has a negative polarization charge, the N-face at the opposite side has a positive polarization charge. The arrows indicate the border of the depletion layer according to equation (4.9)*

approximately the gap voltage E_g/e. The self-consistently calculated band edge alignments, displayed in Fig. 4.2, show this behaviour for all considered doping concentrations. Three different types of screening charges appear.

i) Close to the N-face, the conduction band falls below the Fermi level. This is signature of an electron accumulation layer shielding the positive polarization charge at the surface. Beyond this layer, which is only few a nm wide, the field strength is practically zero.

ii) The valence band edge lies above the Fermi level just at the Ga-face. For the considered n-type material, this indicates an inversion layer. This layer is thinner than the electron accumulation layer at the N-face due to the larger density of states in the valence band.

iii) The inversion layer does not completely screen the surface polarization charge. The residual field drops to zero due to the space charge of the ionized impurities within an extended surface depletion layer.

Useful analytic approximations of some quantities can be found from device physics [164] when neglecting the finite width of the inversion layer and considering that the conduction band edge of the n-type GaN is practically at the Fermi level E_{F} in regions decoupled from surface polarization charges. Then the band edges in the surface depletion layer vary quadratically

$$\tilde{V}_e^{\mathrm{QW}}(z) = E_{\mathrm{F}} + E_{\mathrm{g}} \left(\frac{z}{w_{\mathrm{sur}}} - 1 \right)^2 . \tag{4.8}$$

The corresponding values for the width of the surface depletion layer

$$w_{\mathrm{sur}} = \sqrt{\frac{2E_{\mathrm{g}}\varepsilon\varepsilon_o}{e^2 N_{\mathrm{D}}}} \tag{4.9}$$

are indicated by arrows in Fig. 4.2. It can be seen, that formula (4.9) gives a good approximation to the fully self-consistent calculation. The electric field strength $F(z) = -\frac{\partial}{\partial z}(V_a(z)/\mathrm{q}_a)$ in the surface depletion layer decreases approximately linearly with z to zero,

$$F(z) = -\frac{eN_{\mathrm{D}}}{\varepsilon\varepsilon_o}(w_{\mathrm{sur}} - z). \tag{4.10}$$

The corresponding sheet charge density of the inversion layer at the Ga-face is given by

$$\sigma_{\mathrm{inv}} = P_{\mathrm{sp}} - \sqrt{2E_{\mathrm{g}} N_{\mathrm{D}} \varepsilon\varepsilon_o} . \tag{4.11}$$

All these estimates hold as long as w_{sur} remains smaller than the slab thickness D and the space charge $eN_{\mathrm{D}}w_{\mathrm{sur}}$ is smaller than P_{sp}. For realistic dopings and thicknesses, this is always the case and the top and the bottom of the slab are decoupled by a field-free bulk layer. Therefore, the field situation on top of the slab is independent of the substrate properties. In the less realistic limit of a vanishing doping density, the surface depletion layer would fill the whole slab with the constant residual field $F = E_{\mathrm{g}}/eD$. To summarize, a Ga-face grown n-type sample will exhibit a combined hole inversion and depletion layer at the surface, whereas the polarization charges on top of a N-face grown sample are screened by an electron accumulation layer.

Fermi level pinning by gap states at the surface may modify the situation. In this case positively charged surface states take over the role of the inversion layer, E_{g} has to be replaced in the above considerations by $V_e(z = 0) - E_{\mathrm{F}}$

at the surface, and the space charge region becomes accordingly thinner. However, Fermi level pinning requires that the density of these surface states is larger than the high number density of polarization charges of approximately $10^{13}\,\mathrm{cm}^{-2}$. Depending on the preparation of the samples, this may be the case, but there are not many investigations of this topic up to now [144, 16, 45, 58]. Therefore, this effect is not considered in the following.

4.4.2 Single-Quantum-Well

Now, a SQW with $d_{\mathrm{QW}} = 3\,\mathrm{nm}$, embedded in n-type GaN is considered. In Ga-face grown samples, the depletion layer can penetrate the QW and alter its properties. This is not the case in N-face grown material. To investigate this effect, N-face and Ga-face grown samples with two different cap layer thicknesses in each case are compared. The results of the calculations for the four geometries are summarized for $x = 0.1$ in Fig. 4.3. In the following, the differences between these four geometries are discussed in detail.

N-face sample with thick cap

The band profile of a N-face grown QW with 50 nm cap layer in the high doping case $N_{\mathrm{D}} = 5 \cdot 10^{18}\,\mathrm{cm}^{-3}$ is given by the solid line at the right side of Fig. 4.3 c. Within some nm above the negatively charged interface of the QW, the conduction band edge lies above the Fermi level. The electrons from this depletion layer have been transferred to the first electron subband in the QW, the band edge of which lies below the Fermi level. The voltage drop caused by the excess electrons in the QW and the space charges just compensates the voltage drop $F_{\mathrm{P}} \cdot d_{\mathrm{QW}}$ of the bare piezoelectric field F_{P} across the QW. As a consequence, the band edges become horizontal and equal to the bulk values on both sides sufficiently far from the QW. As long as this holds, the QW is not influenced by the surface and has its *intrinsic configuration*.

It is useful to obtain analytic estimates for the relevant quantities characterizing this configuration. For this purpose the excess electrons in the lowest subband are approximated by a negative charge sheet located at the positive interface of the *intrinsic* QW, and the space charge layer of width w_{int} is assumed to have abrupt borders. Now, standard device physics [164] can be applied again. Vanishing fields sufficiently far from the QW require $\sigma_e = -eN_{\mathrm{D}}w_{\mathrm{int}}$ for the sheet density of excess electrons. Furthermore, the

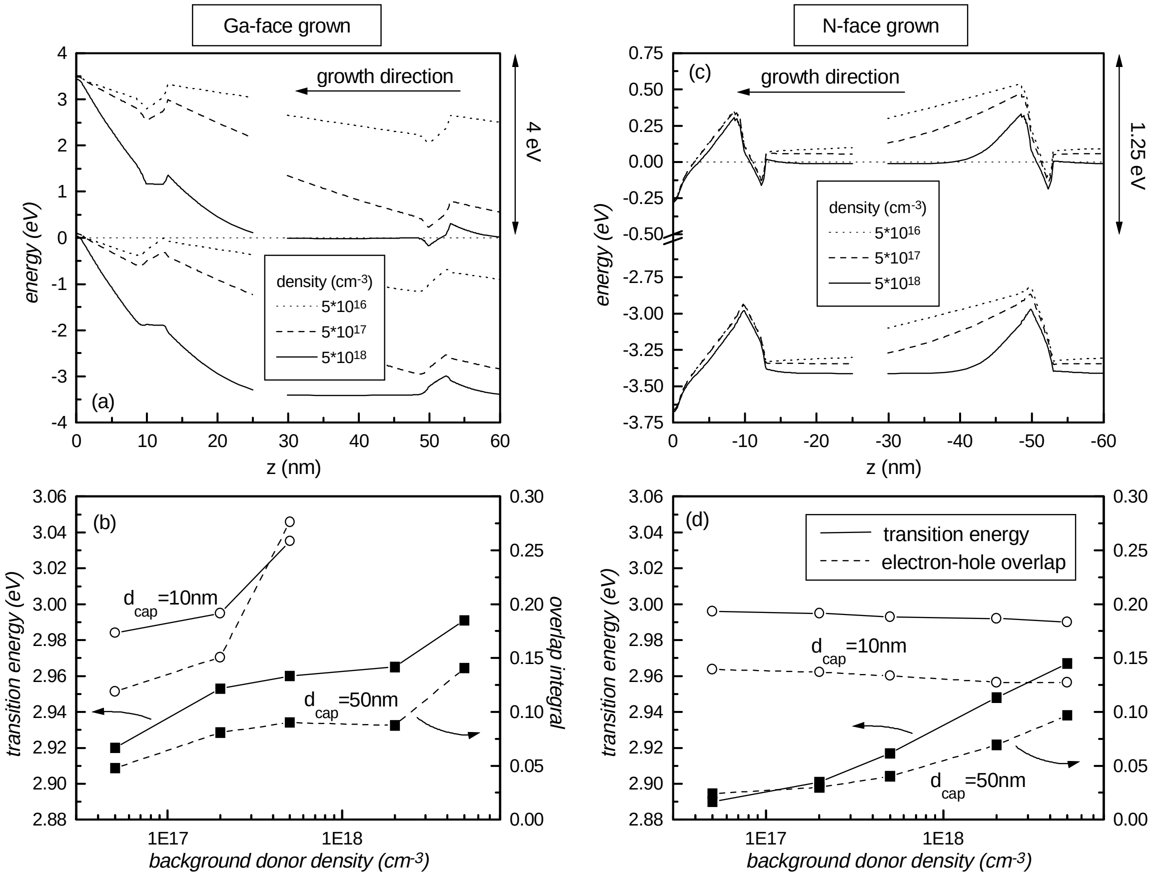

Figure 4.3: *(a), (c): Self-consistently calculated band edge alignments of Ga-face grown (a) and N-face grown (c) 3 nm $In_{0.1}Ga_{0.9}N/GaN$ SQWs for several background donor densities and for 10 nm and 50 nm cap layers. The z-axis is always oriented along the direction of the spontaneous polarization of relaxed GaN with the origin at the surface. The effect of indium surface segregation is included (see section 4.3). The surface is at the origin of the abscissa. (b), (d): Transition energy and electron-hole overlap integral as functions of the background donor density.*

voltage drop across all screening charges has to compensate the voltage drop

$F_\mathrm{P} \cdot d_\mathrm{QW}$ of the bare polarization field across the QW. This yields

$$w_\mathrm{int} = d_\mathrm{QW} \sqrt{\frac{2\sigma_\mathrm{P}}{eN_\mathrm{D} d_\mathrm{QW}}} \tag{4.12}$$

for the width of the depletion layer, measured from the positively charged interface of the QW. The field in this layer varies like

$$F(z) = -\frac{eN_\mathrm{D}}{\varepsilon\varepsilon_o}(z_\mathrm{i} + w_\mathrm{int} - z) + F_\mathrm{P}\Theta_\mathrm{QW}(z) \tag{4.13}$$

where z_i is the position of the positively charged inverted interface of the QW. The function $\Theta_\mathrm{QW}(z)$ is a projector to the well. It equals unity inside the QW and vanishes outside.

The transition energies (see Fig. 4.3 d) exhibit a blueshift by about 80 meV when increasing the donor concentration from $5 \cdot 10^{16}\mathrm{cm}^{-3}$ to $5 \cdot 10^{18}\mathrm{cm}^{-3}$. 40 meV and 150 meV blueshifts are obtained for the alternative compositions $x = 0.05$ and $x = 0.2$, respectively. The blueshift is accompanied by an increase of the electron-hole overlap (see again Fig. 4.3 d). This is the anticipated behaviour, commonly attributed to the increased screening of the polarization fields. Figure 4.3 c shows that the reduction of the field inside the well is however not sufficient for explaining the shift. In addition, the band edge alignment in the space charge layer of the barrier changes, which strongly affects the hole subband function and confinement energy. The combination of both effects is responsible for the total blueshift and the increase of the overlap.

N-face sample with thin cap

For the 10 nm cap layer, the space charge layer in the barrier is restricted by the electron accumulation layer at the surface for all doping concentrations investigated. The band profile of cap layer and QW becomes independent of N_D and, hence, transition energy and electron-hole overlap do as well (see left side of Fig. 4.3 c and open circles in Fig. 4.3 d).

Ga-face sample with thick cap

In Ga-face samples, the band edge profile of the QW is superimposed by the field in the depletion layer beneath the surface, so that transition energy and electron-hole overlap can be changed. The band profiles calculated for the sample with the 50 nm cap layer can be assigned to two cases (see right side of Fig. 4.3a). For the highest doping, the surface depletion layer is thinner than the cap and does not influence the QW, which remains in its *intrinsic configuration*, as already discussed above. The small difference in transition energy to the corresponding N-face case is caused by the asymmetry of the segregation profile. In case of the two smaller doping concentrations, the QW is located within the surface depletion layer, and the band edges are sufficiently far from the Fermi level so that the QW is not filled with carriers. The total potentials in the latter case are the superpositions of the respective QW potential (including the potential of the polarization charges) and the potential of the surface depletion layer, given by equation (4.8). The resulting net field inside the space charge layer is approximately given by

$$F(z) = -\frac{eN_\mathrm{D}}{\varepsilon\varepsilon_o}\left(\tilde{w}_\mathrm{sur} - z\right) + F_\mathrm{P}\Theta_\mathrm{QW}(z). \tag{4.14}$$

The width of the surface depletion layer increases to

$$\tilde{w}_\mathrm{sur} = w_\mathrm{sur}\sqrt{1 + \frac{eF_\mathrm{P}d_\mathrm{QW}}{E_\mathrm{g}}} \tag{4.15}$$

to keep the total potential drop at the GaN gap voltage E_g/e. Here w_sur is the width of the surface depletion layer without a QW, given by equation (4.9).

Now, the behaviour of the total polarization field inside the QW is discussed when increasing the background doping density N_D. The surface depletion contribution to $F(z)$ (first term) has the opposite sign of the polarization contribution, thus reducing the transition redshift via counteracting the quantum confined Stark effect. It vanishes for zero doping density, yielding the maximum field strength F_P and increases like $\sim \sqrt{N_\mathrm{D}}$ as long as the width $\tilde{w}_\mathrm{sur}$ of the surface depletion layer remains much larger than the thickness of the cap. The corresponding blueshift of the transition energies is depicted in Fig. 4.3 b. With further increase of N_D, the depletion contribution reaches a maximum for $\tilde{w}_\mathrm{sur} = 2d_\mathrm{cap}$, resulting in saturation of the blueshift. Beyond this value the depletion contribution decreases and vanishes again for $\tilde{w}_\mathrm{sur} \to d_\mathrm{cap}$, leaving behind the QW in its *intrinsic configuration*. However, a possibly related transition redshift does not occur. The dominant effect of the increasing hole confinement energy resulting from the steeper band edge alignment in the lower barrier yields a further blueshift of

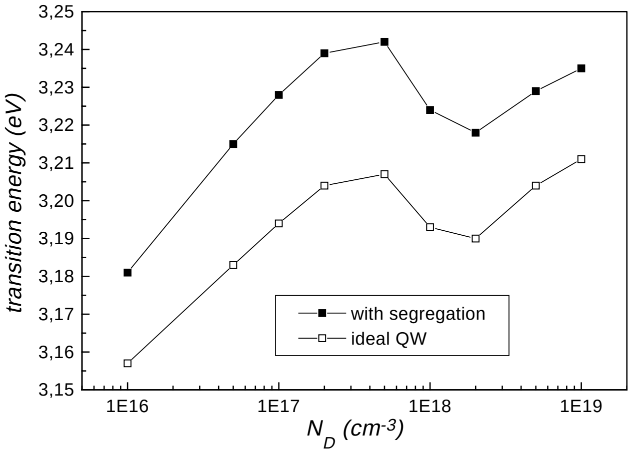

Figure 4.4: *Transition energy of a Ga-face grown 3 nm* $In_{0.05}Ga_{0.95}N/GaN$ *SQW with a 50 nm cap layer as a function of a homogeneous background donor density with and without the consideration of indium surface segregation.*

the transition energy, seen in Fig. 4.3 b. In addition, the screening effect from the successive filling of the electron groundstate subband with electrons from ionized donors contributes to the blueshift. Although the screening mechanisms are different, the total blueshift obtained when increasing N_{D} from $5 \cdot 10^{16}\,\mathrm{cm}^{-3}$ to $5 \cdot 10^{18}\,\mathrm{cm}^{-3}$ is approximately equal to the shift observed in case of the N-face QW with 50 nm cap (80 meV and 150 meV for x =0.1 and 0.2, respectively).

In case of the Ga-face grown QW with $x = 0.05$ and 50 nm cap layer, the interplay of the different screening mechanisms results in a non-monotonic behaviour of the transition energy with increasing N_{D}, displayed in Fig. 4.4. For a QW with smaller indium concentration, the filling of the electron subband appears at higher N_{D} due to the weaker confinement and the smaller unscreened field.

Ga-face sample with thin cap

The band profiles of a Ga-face sample with a 10 nm cap layer (left part of Fig. 4.3 a) show some new effects with respect to the above discussed cases. First, the net field in the QW vanishes for the highest donor concentration in accordance with equation (4.14). A highly blue shifted transition could be expected. However, due to the segregated indium profile and the strong field in the depletion layer, the hole barrier is reduced to an extremely small value and captured carriers will escape very fast. If the characteristic escape time is much smaller than the radiative lifetime, no radiative emission from this QW can be expected. Therefore, no transition energies and overlap integrals are plotted for high doping and small cap width.

Second, for weakest doping, the valence band maximum in the QW approaches the Fermi level so that the hole ground state becomes occupied, forming a further inversion layer. The former surface depletion layer is now shifted into the sample and a new thin surface depletion layer appears. Because of the relatively large density of states in the valence band, the band profile in QW and cap layer is nearly fixed by the requirement that the hole level is close to the Fermi energy. Thus, transition energy and electron-hole overlap remain nearly unchanged with increasing N_{D} until the occupation of the hole subband becomes negligible and the valence band edge comes off the Fermi level.

The blueshifted transition energies and larger overlaps with respect to the thicker cap layer are consequences of the field distribution in the surface depletion layer. The thinner the cap layer, the higher is the depletion field and the more pronounced the counteraction of the quantum confined Stark effect.

Summarizing the case of a SQW in n-type GaN, the following four qualitatively different situations have been found.

1. *Intrinsic configuration of the QW:* Sufficiently far from the surfaces, the polarization charges induce a thin electron accumulation layer at the positively charged interface in the QW and a rather thick space charge region extending into the opposite barrier. With increasing N_{D} the anticipated blueshift occurs.

2. *QW close to a N-terminated surface:* Band profile and transition energy are independent of N_{D}.

3. *QW in the surface depletion layer:* The transition energy is modified by the local electric field in the depletion layer and depends strongly on position and doping level.

4. *QW close to a Ga-terminated surface:* In case of low doping concentrations, band profile and transition energy are fixed by occupation of the

hole level in the QW. In case of high doping ($N_\mathrm{D} > 5 \cdot 10^{17}\,\mathrm{cm}^{-3}$) and low indium concentration ($x \leq 0.1$), carrier localization may be absent as a result of segregated interfaces and a high field in the surface depletion layer.

4.4.3 Multiple-Quantum-Well

In MQW structures, different QWs may experience different electric field situations. In case of a Ga-face grown MQW stack, the upper QWs reside within the surface depletion layer, whereas the lower QWs may be already below this region. This gives rise to a set of transition energies and an additional inhomogeneous broadening of the total optical transition spectrum. The self-consistent band profiles of a series of Ga-face grown MQW stacks with different numbers of QWs, donor concentrations, and compositions are discussed. The well width is $d_\mathrm{QW} = 3\,\mathrm{nm}$, the barriers and the cap layer are $d_\mathrm{B} = d_\mathrm{cap} = 8\,\mathrm{nm}$ wide.

Figure 4.5 shows the result for a 10 period structure with $x = 0.1$. In case of medium and high doping, $N_\mathrm{D} = 5 \cdot 10^{17}\,\mathrm{cm}^{-3}$ and $5 \cdot 10^{18}\,\mathrm{cm}^{-3}$, respectively, the situation is as expected. The band profile in the depletion layer is approximately given by the superposition of the potential of the MQW and the space charge potential. The resulting field strength $F(z)$ and the width $\tilde{w}_\mathrm{sur}$ of the depletion layer are still well described by equations (4.14) and (4.15) when the total width of all depleted QWs is used for d_QW. Below the depletion layer, the band profiles of the QWs are periodic. The interplay of segregation and a strong field in the surface depletion layer hinders the uppermost QW from confining carriers (see solid lines in Fig. 4.5).

For very high doping, the profile of every period of this stack equals the *intrinsic configuration* of a SQW, discussed in the previous section, and the fields of neighbouring QWs are decoupled and given by equation (4.13). Decreasing the doping level, a situation appears, where the available space charge is limited by the MQW period, and the screening of the polarization field in the QWs is reduced in comparison with a SQW. Using again the approximations and notations of the previous section, and demanding periodicity of the electrostatic potential, the electric field profile within one period now becomes

$$F(z) = -\frac{eN_\mathrm{D}}{\varepsilon\varepsilon_o}(z_\mathrm{i} + L - z) + F_\mathrm{P}\Theta_\mathrm{QW}(z) + F_0\,. \tag{4.16}$$

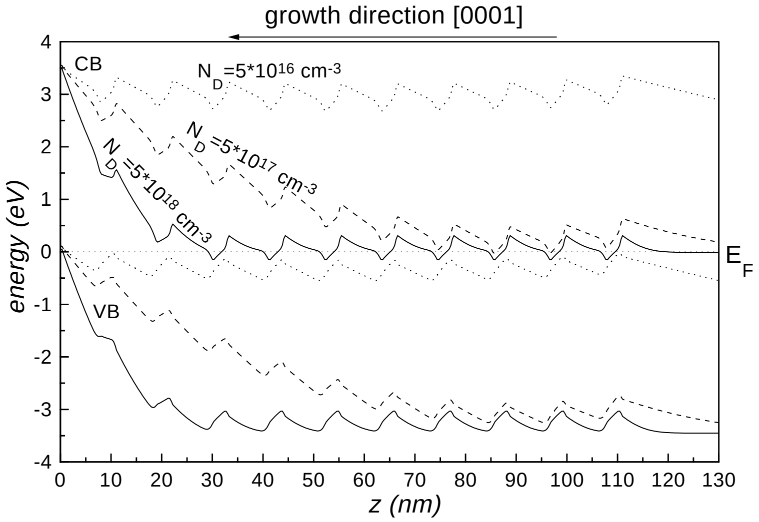

Figure 4.5: *Self-consistently calculated band edge alignment of Ga-face grown 3 nm (well)/8 nm (barrier) $In_{0.1}Ga_{0.9}N/GaN$ 10MQWs for several background donor densities. The surface is at the origin of the abscissa. The effect of indium surface segregation is considered (see section 4.3).*

Here z_{i} again denotes the position of the positively charged inverted interface of the respective QW, $\Theta_{\mathrm{QW}}(z)$ is again the domain function vanishing outside and being unity inside a QW, and $L = d_{\mathrm{QW}} + d_{\mathrm{B}}$ is the MQW period. The additional term $F_0 = eN_{\mathrm{D}}L/2\varepsilon\varepsilon_o - F_{\mathrm{P}}d_{\mathrm{QW}}/L$ is the residual field strength at the border $z = z_{\mathrm{i}} + L$ to the adjacent QW.

An unexpected band profile is obtained in the low doping case, $N_{\mathrm{D}} = 5 \cdot 10^{16}\,\mathrm{cm}^{-3}$. The valence band edge maxima of all QWs come close to the Fermi level, so that they are slightly populated with holes. This is the configuration of a MQW in p-type material. A closer inspection of the calculated charge and potential distributions shows (i) that the hole occupation in the QWs builds up at the expense of the surface inversion layer, (ii) that the occupation of the QWs is not strictly uniform but has maxima in the first and last QW, and (iii) that the depletion layer is shifted into the sample, now emerging beneath the deepest QW and having the width w_{sur} given by equation (4.9).

To finally get a measure of how the distribution of optical transition energies affects a transition spectrum, the transitions of all contributing QWs have been added in the form of phenomenologically broadened Gaussian curves, each positioned at the respective transition energy and equally weighed. In-plane inhomogeneities like compositional fluctuation and interface roughness are considered only implicitly by assuming a finite x-dependent linewidth for each transition (50 meV for $x = 0.05$, 80 meV for $x = 0.1$, and 100 meV for $x = 0.2$), accounting for the tendency of larger linewidth in case of higher indium content [124].

In Fig. 4.6, an additional broadening of the MQW transition spectra compared to the SQW transition can be seen, sensitively depending on the screening situation and the indium content. Especially for an indium concentration of $x \geq 0.1$ and a doping density of $N_\mathrm{D} \geq 5 \cdot 10^{17}\,\mathrm{cm}^{-3}$, when the width of the depletion layer is in the same range like the thickness of the MQW stack, this broadening effect is strong and can also lead to a deformation or even splitting of the spectrum. High energy features always stem from the last grown QWs directly under the sample surface. According to equation (4.10), there is the strongest depletion field, resulting in the strongest blueshift of the transition via counteracting the quantum confined Stark shift. The relative heights of a multi-peak spectrum as well as the details of an emission lineshape sensitively depend on the relative contributions of each QW. These are in turn a result of the mechanisms of absorption, relaxation, diffusion, transfer between the QWs, radiative and non-radiative recombination, which is beyond the scope of this investigation. The limit of dominant nonradiative recombination, when the emission of a QW becomes proportional to the electron-hole overlap, is displayed in Fig. 4.7. The stronger contribution of high-energetic transitions results from the increased overlap in case of a reduced field inside the well.

4.5 Screening by Excitation-Induced Carriers

All considerations up to this point are valid only within the limit of small excitation densities which do not significantly alter the equilibrium band edge alignment. To simulate higher excitation densities with the Poisson-Schrödinger program, which calculates only the equilibrium ground state, the band gap energy must be reduced in well and barrier by the same value. This value has to be large enough so that the lowest valence subband comes near or even crosses the Fermi energy, which is—in case of n-type material—near the conduction band. In this way, excess carriers are simulated by

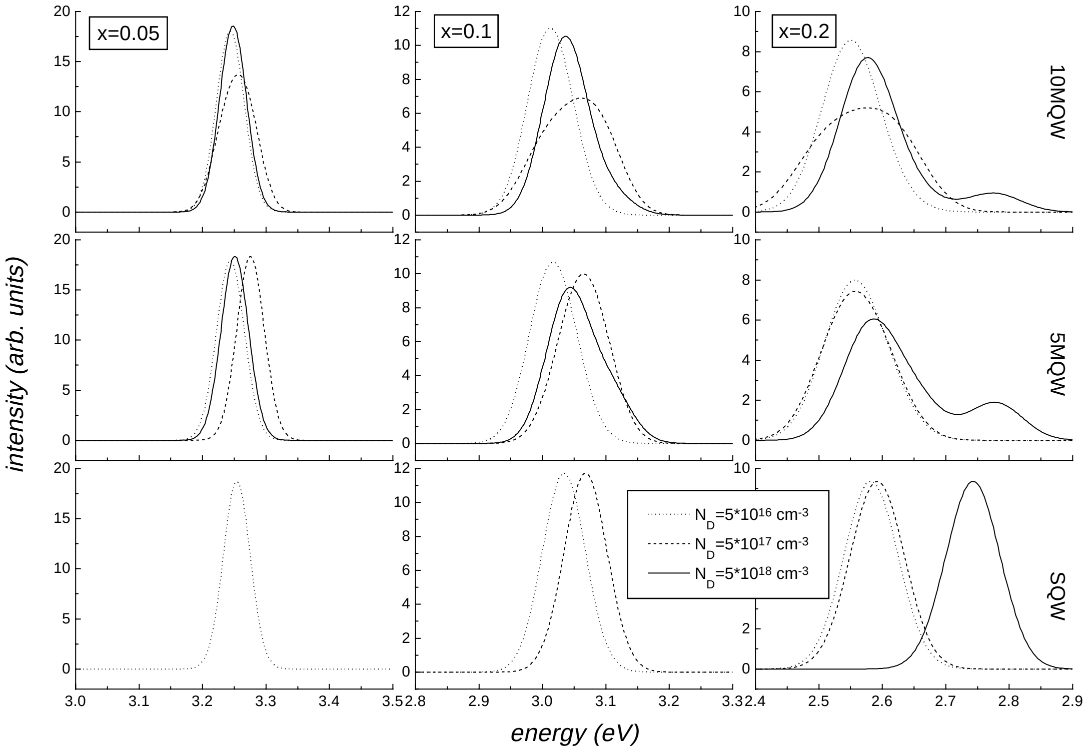

Figure 4.6: *Optical transition spectra of Ga-face grown 3 nm (well)/8 nm (barrier) $In_xGa_{1-x}N/GaN$ SQWs, 5MQWs and 10MQWs for several indium contents x and background donor densities N_{D}. The effect of indium surface segregation is considered (see section 4.3). In case of the SQW, no line is drawn if carrier confinement cannot be expected due to a strong field in the depletion layer and low tunneling barriers. For $x = 0.2$, all QWs contribute to the spectrum. For $x = 0.1$, the last grown QW of the 5MQW and 10MQW does not contribute if the background density $N_{\mathrm{D}} \geq 5 \cdot 10^{17}\,\mathrm{cm}^{-3}$. In case of $x = 0.05$, the same holds for the last two grown QWs, except for the 10MQW at $N_{\mathrm{D}} = 5 \cdot 10^{17}\,\mathrm{cm}^{-3}$, where only seven QWs contribute to the spectrum. Independent of the number of QWs contributing to the spectrum, the total intensities are normalized.*

usual, thermally excited carriers (see Fig. 4.8). Due to the field in the well the occupation of the valence subband occurs at the opposite side to where the electrons are located, and so the polarization charges at the interfaces

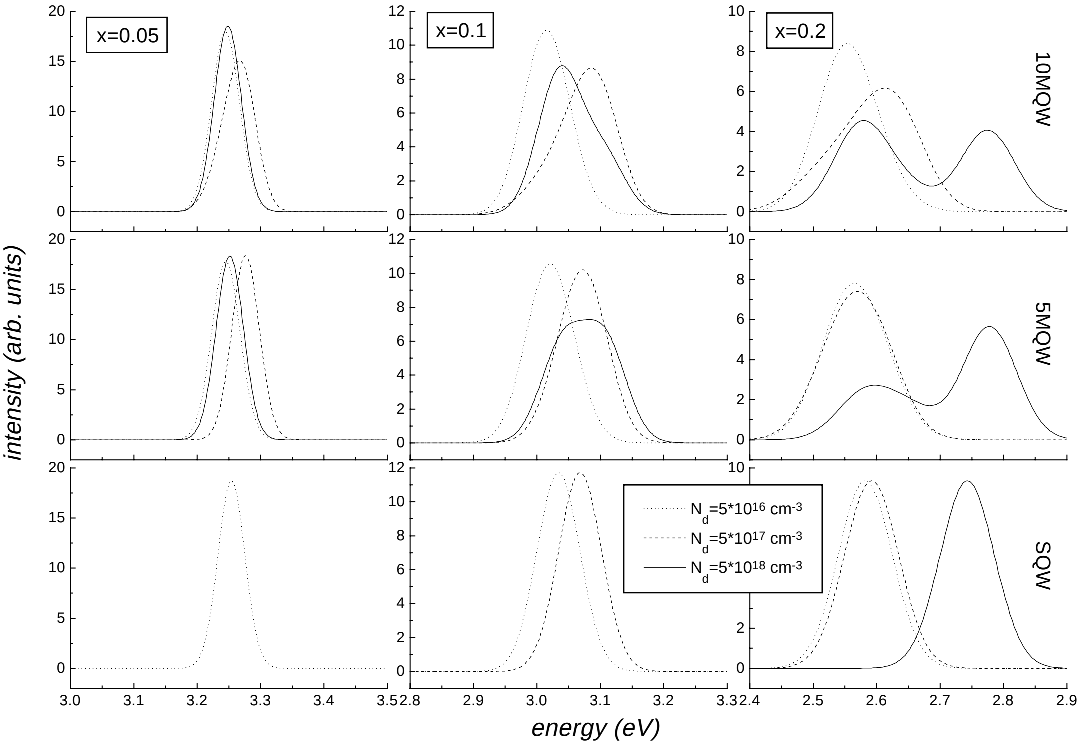

Figure 4.7: *The only difference to Fig. 4.6 is that the QW emissions are not equally weighed but with respect to the electron-hole overlap. This corresponds to the limit of dominant nonradiative recombination.*

are screened and the band edge inside the QW flattens. As it was shown in the previous sections, the absolute value of the band gap energy has major influence on the overall electrostatic situation in the sample. Therefore, this method is restricted to the consideration of a SQW in the *intrinsic configuration*, decoupled from its environment.

According to Fermi's Golden Rule, the recombination rate R is given by

$$R(p) = \frac{p}{\tau(p)} \sim p \left| \int dz \, \varphi_e^*(z) \, \varphi_h(z) \right|^2 , \tag{4.17}$$

if the minority carrier density is small compared to the majority carrier density, where p is the minority carrier (hole) density and τ is the carrier lifetime which is inverse proportional to the electron-hole overlap. Then, the transient

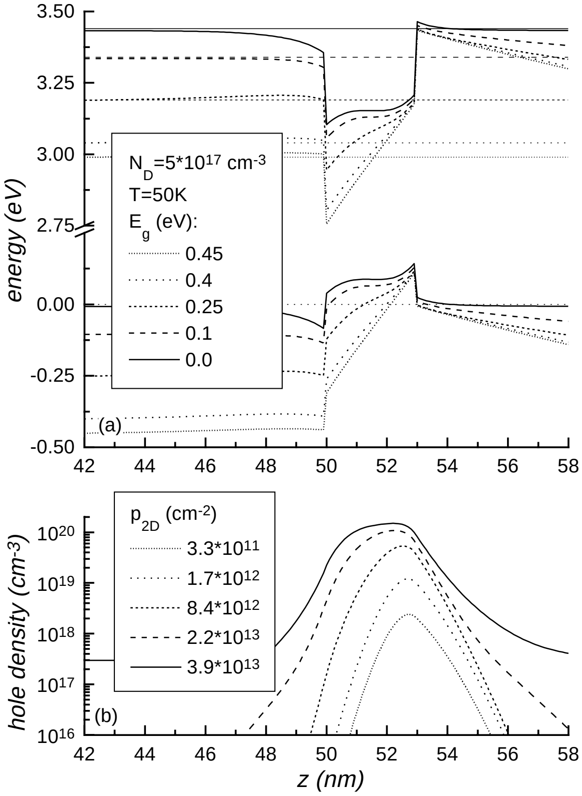

Figure 4.8: *(a) Self-consistently calculated band edge alignments of a 3 nm thick* $In_{0.1}Ga_{0.9}N/GaN$ *SQW for various values of the gap energy but constant band offsets. (b) Minority carrier (hole) densities.*

$\dot{p}(t) = dp(t)/dt = -R[p(t)]$, which is detected in a time-resolved photoluminescence experiment, and the time dependence of the transition energy can be easily calculated. It is shown later that the above made assumption, which is a good approximation if the influence of the subband overlap is predominantly compared to all other dependencies, is justified in the used range of parameters.

After calculating self-consistent band edge profiles for various values of the reduced gap energy (see Fig. 4.8 a), the minority carrier sheet densities

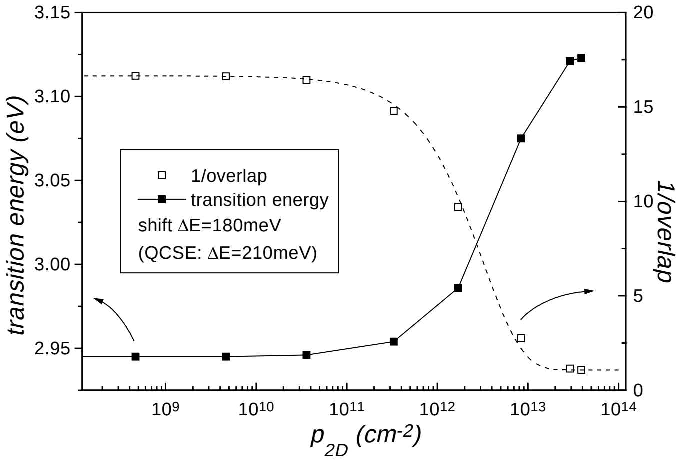

Figure 4.9: *Open symbols: inverse overlap* $\left|\int dz\, \varphi_e^*(z)\, \varphi_h(z)\right|^{-2}$ *as a function of the hole sheet density in the well. Dashed line: exponential fit according to equation (4.19). Solid symbols: transition energy as a function of the hole sheet density in the well.*

$p = p_{\mathrm{2D}}$ are calculated

$$p_{\mathrm{2D}} = \frac{m_h}{\pi\hbar^2} \int dE\, f(E) = \frac{m_h kT}{\pi\hbar^2} \ln\left(1 + \mathrm{e}^{(E_{\mathrm{F}} - \epsilon_h)/kT}\right) \tag{4.18}$$

where $f(E)$ is the Fermi function, E_{F} is the Fermi energy, and ϵ_h is the lowest valence subband level. The values obtained with formula (4.18) agree very well with those obtained by integrating the density profiles calculated by the Poisson-Schrödinger program and plotted in Fig. 4.8 b. The overlap as a function of the hole sheet density p can be fitted very well with an inverse exponential dependency (see open symbols and dashed line in Fig. 4.9), so that

$$R(p) \sim \frac{p}{1 + c\, \mathrm{e}^{-p/p_o}}\,, \tag{4.19}$$

where c and p_o are fitting parameters, depending on the sample configuration. With this approximation, the differential equation $\dot{p}(t) = -R[p(t)]$ can be solved analytically for the inverse function

$$t(p) \sim -\mathrm{Ei}(-p(t)/p_o) + \mathrm{Ei}(-p(0)/p_o) - \frac{1}{c} \ln(p(t)/p(0))\,, \tag{4.20}$$

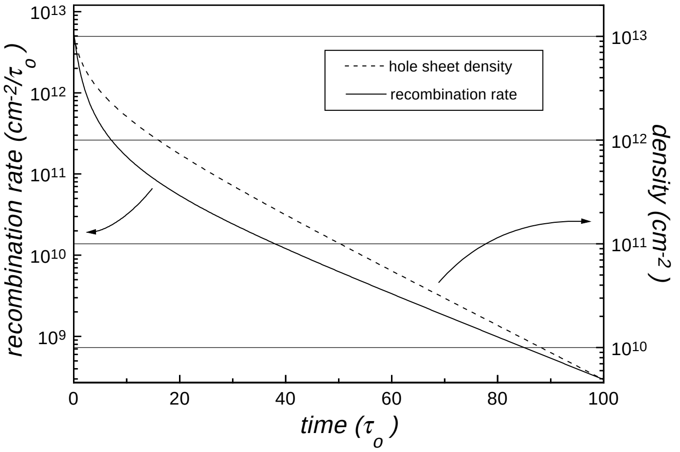

Figure 4.10: *Solid line: Transient $dp(t)/dt$ of a 3 nm wide $In_{0.1}Ga_{0.9}N/GaN$ SQW with a considered excitation density $p(t=0) = 1 \cdot 10^{13}\,cm^{-2}$. Dashed line: Corresponding minority carrier (hole) sheet density p in the well.*

where $\mathrm{Ei}(x) = \int_{-\infty}^{x} dt\, \mathrm{e}^t/t$ is the exponential integral.

The results for $\dot{p}(t)$ and $p(t)$ are plotted in Fig. 4.10 for a 3 nm wide $\mathrm{In_{0.1}Ga_{0.9}N/GaN}$ SQW for the starting condition $p(0) = 1 \cdot 10^{13}\,\mathrm{cm}^{-2}$. The result for $x = 0.3$ looks approximately the same. In the density range where the screening occurs ($1 \cdot 10^{11}\,\mathrm{cm}^{-2}$–$1 \cdot 10^{13}\,\mathrm{cm}^{-2}$), a clearly non-exponential decay curve can be observed. The corresponding screening-induced shift of the transition energy is plotted as a function of the density p in Fig. 4.9 (solid symbols). For a maximum density of $p = 1 \cdot 10^{13}\,\mathrm{cm}^{-2}$ we observe a shift of $\Delta E \approx 140\,\mathrm{meV}$ (310 meV for a QW with $x = 0.3$).

If the hole density p cannot be considered to be small compared to the electron density, p has to be replaced by $\int d^2k f_e(k)\, f_h(k)$ in equation (4.17), where $f_a(k)$ ($a = e, h$) are the Fermi occupation functions. By numerical evaluations of this expression it could be shown, that $p \sim \int d^2k f_e(k)\, f_h(k)$ is a very good approximation within the whole range of considered excitation densities. Above $p = 1 \cdot 10^{13}\,\mathrm{cm}^{-2}$, the occupation of higher subbands becomes more and more important, and this approximation becomes less reliable.

4.6 Summary

Energies and oscillator strengths of optical transitions in (In,Ga)N/GaN QW structures with thin cap layers were investigated theoretically. Based on a self-consistent solution of the Schrödinger-Poisson system of equations, the internal fields generated by spontaneous and piezoelectric polarization charges at surfaces and interfaces were systematically discussed for various sample configurations and under consideration of indium surface segregation. Background doping density, thickness of the cap layer, number of quantum wells, indium content, and polarity of the structure were varied.

Indium segregation was shown to result in a blueshift of the emission energy compensating up to one third of the respective quantum confined Stark shift. This blueshift is accompanied by a decrease of the electron-hole overlap compared to a rectangular indium profile with the same integral indium content due to the asymmetry of the segregation lengths at the interfaces.

It was shown that background doping influences transition energy and overlap not only via screening of the polarization charge at the material interfaces by quantum confined carriers, but also via ionized dopants in depletion layers. Therefore, the position of the QW in the sample with respect to an extended depletion layer—which was shown to exist in Ga-face grown material with n-type doping—severely affects transition energy and electron-hole overlap. The interplay of different screening effects can even result in a non-monotonic shift of the emission energy with increasing background donor density.

An optical transition spectrum of a Ga-face grown MQW can display shoulders or even a multiple-peak structure, sensitively depending on the background doping density and on the magnitude of inhomogeneous in-plane broadening. This effect is a consequence of the spatial variation of the field strength in the surface depletion layer in Ga-face grown structures with n-type doping.

Table 4.1: *Calculation parameters used in this chapter. The abbreviation lin. int. stands for linear interpolation.*

Parameter	GaN	InN	(In,Ga)N
$a\,[\mathrm{nm}]$ [a]	0.3189	0.354	lin. int.
$c\,[\mathrm{nm}]$ [a]	0.5185	0.570	lin. int.
$E_\mathrm{g}\,[\mathrm{eV}]$	3.4	1.8	
b (bowing) [eV] [b]			2.5
m_e/m_o [c]	0.2	0.2	
m_h/m_o [d]	1.0	1.0	
ε	9.5	12.0	lin. int.
$T[\mathrm{K}]$	300	300	
$\Delta E_\mathrm{c}/\Delta E_\mathrm{v}$ [e]			70/30
$P_\mathrm{sp}\,[\mathrm{C/m^2}]$ [f]	-0.029	-0.032	lin. int.
$e_{33}\,[\mathrm{C/m^2}]$ [f]	0.73	0.97	lin. int.
$e_{31}\,[\mathrm{C/m^2}]$ [f]	-0.49	-0.57	lin. int.
$C_{11}\,[\mathrm{GPa}]$ [g]	367	223	lin. int.
$C_{12}\,[\mathrm{GPa}]$ [g]	135	115	lin. int.
$C_{13}\,[\mathrm{GPa}]$ [g]	103	92	lin. int.
$C_{33}\,[\mathrm{GPa}]$ [g]	405	224	lin. int.

[a] Refs. [42, 161, 51]
[b] Refs. [154, 175, 145]
[c] Refs. [80, 163, 98]
[d] Refs. [80, 163, 98, 185, 128, 40]
[e] Refs. [44, 174, 99]
[f] Ref. [17]
[g] Ref. [178]

Chapter 5

Absorption Spectra in the Presence of Polarization Fields

Photoluminescence excitation (PLE) spectra of (In,Ga)N/GaN MQWs exhibit a smooth increase of the signal towards increasing excitation energy with an extended low-energetic tail (see Fig. 2) [33, 35, 15, 108, 37, 34, 38, 151, 101]. Of course, one reason for this consists in the strong compositional inhomogeneity, which results in the formation of strongly localized band-tail states. Apart from this, the macroscopic polarization fields arising from the charges at the well-barrier interfaces have an influence on the single-particle inter-subband absorption by changing drastically transition energies and optical matrix elements. This effect will be investigated in this chapter. As an approach to the signal detected in an PLE experiment with a MQW sample, the single-particle absorption spectrum of an ideal superlattice (SL) without in-plane inhomogeneities and with a periodic potential along the QW axis is calculated in the presence of internal polarization fields. Solutions of the Schrödinger-Poisson system of equations show that the band edge alignment of a MQW is approximately periodic in the limits of low and high doping densities (see Fig. 4.5) or in case of a thick cap layer.

In envelope function approximation, the absorption is in principle given by the sum over all inter-subband matrix elements [146]

$$\alpha(\hbar\omega) \sim \sum_{n,m,q} \left| \int dz\, \varphi^{e*}_{nq}(z)\, \varphi^{h}_{mq}(z) \right|^2 \Theta(\hbar\omega - E^e_n(q) + E^h_m(q)) \,, \tag{5.1}$$

where n and m are the subband quantum numbers in the conduction and valence band, respectively, and q is the quasi momentum for the motion along the SL axis. The diagonality in q is a consequence of the neglect of the photon momentum, which is justified since the wavelength of the light in the sample ($\approx$ 150 nm) is large compared to the SL period (= 8.6 nm). The Θ-function in (5.1) results from the summation over in-plane states and reflects the constant density of states in a QW. The subband functions are given by the Schrödinger equations

$$\left[-\frac{\hbar^2}{2m_a}\Delta_z + V_a^{\mathrm{SL}}(z)\right]\varphi_{nq}^a(z) = E_n^a(q)\,\varphi_{nq}^a(z) \quad (a=e,h) \tag{5.2}$$

with the periodic SL potentials

$$V_e^{\mathrm{SL}}(z) = \begin{cases} -eF_{\mathrm{B}}\,z + \Delta_e + c & -(d_{\mathrm{B}}+d_{\mathrm{QW}})/2 \le z < -d_{\mathrm{QW}}/2 \\ -eF_{\mathrm{QW}}\,z & -d_{\mathrm{QW}}/2 \le z \le d_{\mathrm{QW}}/2 \\ -eF_{\mathrm{B}}\,z + \Delta_e - c & d_{\mathrm{QW}}/2 < z \le (d_{\mathrm{B}}+d_{\mathrm{QW}})/2\,. \end{cases} \tag{5.3}$$

and

$$V_h^{\mathrm{SL}}(z) = \begin{cases} eF_{\mathrm{B}}\,z + \Delta_h - c & -(d_{\mathrm{B}}+d_{\mathrm{QW}})/2 \le z < -d_{\mathrm{QW}}/2 \\ eF_{\mathrm{QW}}\,z & -d_{\mathrm{QW}}/2 \le z \le d_{\mathrm{QW}}/2 \\ eF_{\mathrm{B}}\,z + \Delta_h + c & d_{\mathrm{QW}}/2 < z \le (d_{\mathrm{B}}+d_{\mathrm{QW}})/2\,. \end{cases} \tag{5.4}$$

F_{QW} and F_{B} are the polarization fields in the well and barrier, respectively, d_{B} is the barrier thickness, $c = (|F_{\mathrm{B}}| + |F_{\mathrm{QW}}|)\,d_{\mathrm{QW}}/2$, and Δ_a $(a=e,h)$ are the band offsets. The periodicity of the potential requires $F_{\mathrm{QW}}\,d_{\mathrm{QW}} + F_{\mathrm{B}}\,d_{\mathrm{B}} = 0$. Analogous to the Bloch problem of an electron in the periodic potential of a lattice, we make the ansatz

$$\varphi_{nq}(z) = v_{nq}(z)\,\mathrm{e}^{iqz} \quad \text{with} \quad v_{nq}(z + d_{\mathrm{QW}} + d_{\mathrm{B}}) = v_{nq}(z) \tag{5.5}$$

which yields

$$\left[-\frac{\partial^2}{\partial z^2} - i2q\frac{\partial}{\partial z} + \frac{2m_a}{\hbar^2}\,V_a^{\mathrm{SL}}(z)\right] v_{nq}^a(z) = \frac{2m_a}{\hbar^2}\left(E_n^a(q) - \frac{\hbar^2 q^2}{2m_a}\right) v_{nq}^a(z)\,. \tag{5.6}$$

Now we calculate numerically the subband functions and energies by discretizing real space and momentum space for $-\pi/(d_{\mathrm{B}}+d_{\mathrm{QW}}) \le q \le \pi/(d_{\mathrm{B}}+d_{\mathrm{QW}})$. In this way we obtain not only the absorption in arbitrary units, but also

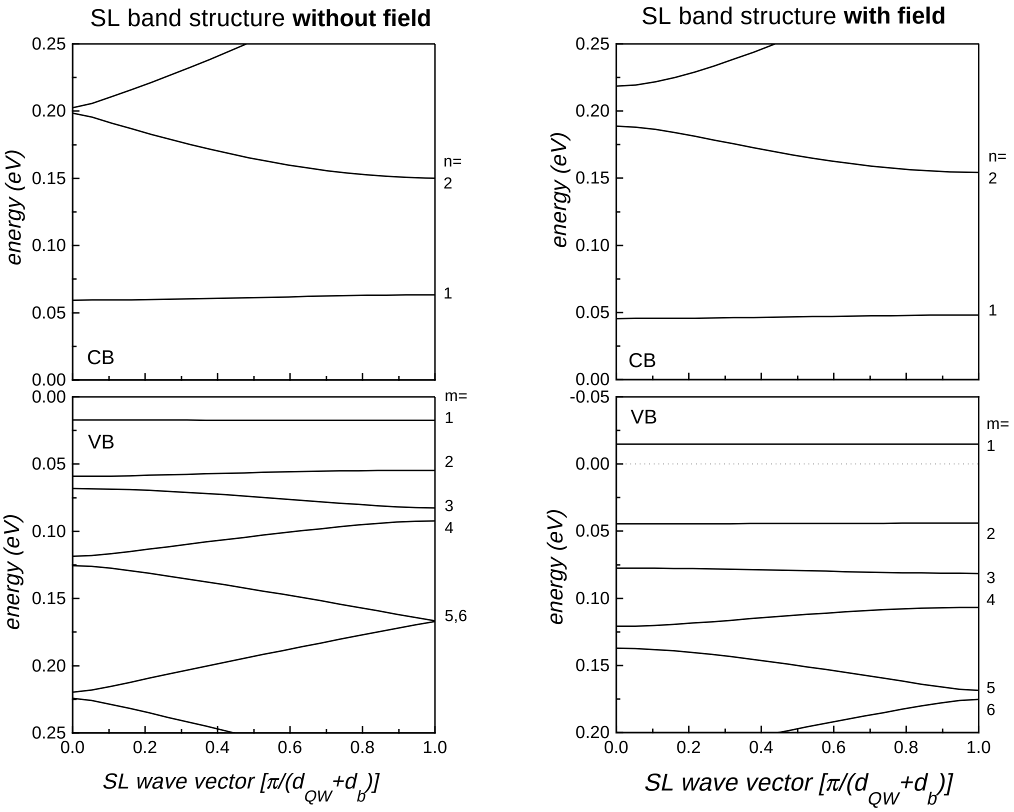

Figure 5.1: *Backfolded miniband structures of a* $In_{0.05}Ga_{0.95}N/GaN$ *SL with* $d_{\mathrm{QW}} = 3\,\mathrm{nm}$ *and* $d_{\mathrm{B}} = 5.6\,\mathrm{nm}$ *with (right side) and without (left side) the consideration of polarization fields along the SL axis. The zeros of the energetic scales are at the band edges in the middle of the well, corresponding to expressions (5.3) and (5.4). The offsets are approximately 140 meV and 60 meV in conduction band and valence band, respectively.*

the miniband structures, displayed as backfolded diagrams in Fig. 5.1 for a $\mathrm{In_{0.05}Ga_{0.95}N/GaN}$ SL with $d_{\mathrm{QW}} = 3\,\mathrm{nm}$ and $d_{\mathrm{B}} = 5.6\,\mathrm{nm}$. To fulfil the requirement of periodicity, the polarization fields in well and barrier must read

$$F_{\mathrm{QW}} = \frac{d_{\mathrm{B}}}{d_{\mathrm{B}} + d_{\mathrm{QW}}} \frac{P_{\mathrm{B}} - P_{\mathrm{QW}}}{\varepsilon\varepsilon_o} \tag{5.7}$$

$$F_{\mathrm{B}} = \frac{d_{\mathrm{QW}}}{d_{\mathrm{B}} + d_{\mathrm{QW}}} \frac{P_{\mathrm{QW}} - P_{\mathrm{B}}}{\varepsilon\varepsilon_o}\,, \tag{5.8}$$

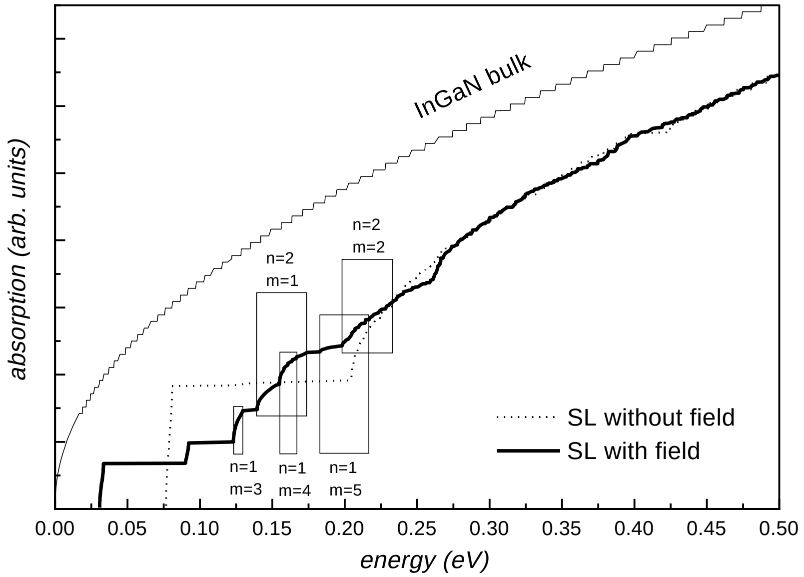

Figure 5.2: *Absorption of a* $In_{0.05}Ga_{0.95}N/GaN$ *SL with* $d_{\mathrm{QW}} = 3\,nm$ *and* $d_{\mathrm{B}} = 5.6\,nm$*. The calculation was executed with (solid line) and without (dashed line) polarization fields along the SL axis. The first two steps of the solid line arise from the transitions n=1/m=1 and n=1/m=2, where* n *and* m *denote the conduction and valence subband indices, respectively. Position and width of some further transitions are indicated by boxes. For comparison, the root-shaped absorption of* $In_{0.05}Ga_{0.95}N$ *bulk material is plotted, too. The little steps come from the numerical mesh.*

where the total polarizations P_{QW} and P_{B} (including spontaneous plus strain-induced contribution) have been taken from literature [17]. To obtain the polarization of the $\mathrm{In}_x\mathrm{Ga}_{1-x}\mathrm{N}$ alloy, a linear interpolation between the values for GaN and InN has been made.

Two effects of the polarization field can be extracted from Fig. 5.1. First, both lowest electron and hole level are shifted towards lower confinement energies yielding the well known transition energy redshift of the quantum confined Stark effect. The second result is the stronger confinement and thus weaker coupling of neighboured wells. This is reflected in the weaker dispersion of the lowest levels (smaller miniband width) and in the larger miniband gaps.

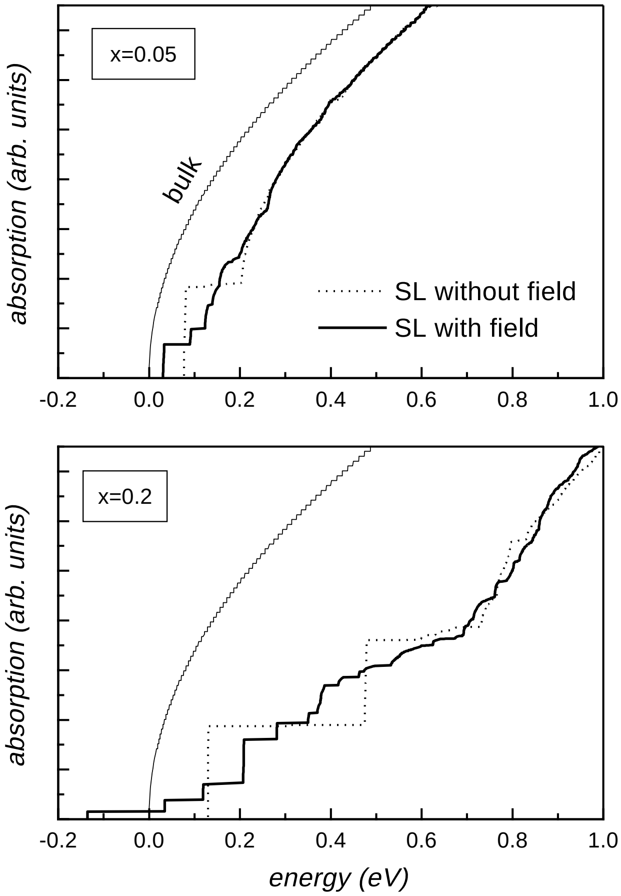

Figure 5.3: *Absorption of a* $In_xGa_{1-x}N$ */GaN SL with* $d_{\mathrm{QW}} = 3\,\mathrm{nm}$ *and* $d_{\mathrm{B}} = 5.6\,\mathrm{nm}$ *for* $x = 0.05$ *and* $x = 0.2$*. The calculations were executed with (solid line) and without (dashed line) polarization fields along the SL axis.*

By the comparison of the calculated absorption spectra with and without polarization fields in Fig. 5.2, the effect of a smoothing of the signal caused by the fields can be clearly seen. This results from the abolition of the nearly diagonal selection rule of inter-subband transitions by the asymmetry of shift and deformation of the subband functions with respect to conduction and valence band. Without fields (dotted line), the absorption is dominated by the oscillator strengths of the n=1/m=1-transition and the

n=2/m=2-transition. The polarization fields result in a more homogeneous redistribution of oscillator strength to all (also non-diagonal) inter-subband transitions. A similar calculation for the case of a SQW has been reported in literature which confirms this findings [65]. It furthermore shows that the onset of the absorption is virtually independent of the QW width.

Additionally, the dispersion of the SL miniband states contributes to the smoothing of the signal by rounding off the otherwise step-like increase of the absorption due to a transition. This effect is more pronounced for transitions between energetically higher minibands which have a larger width due to a stronger coupling between neighboured QWs. Now, if one considered additionally inhomogeneous broadening due to alloy and wellwidth fluctuations, the experimentally measured shape of the absorption could be qualitatively explained in this simple single-particle picture.

In Fig. 5.3 it can be seen that the effect of the smoothing of the absorption signal by internal polarization fields is stronger in case of higher indium contents, where more subbands are confined in the wells. For an indium content of $x = 0.2$, the lowest transition is shifted even below the gap energy of the $\mathrm{In}_x\mathrm{Ga}_{1-x}\mathrm{N}$ well material.

Table 5.1: *Calculation parameters used in this chapter.*

Parameter	GaN	InN	$\mathrm{In}_x\mathrm{Ga}_{1-x}\mathrm{N}$
E_g [eV]	3.4	1.9	
b (bowing) [eV] [a]			2.5
m_e/m_o [b]	0.2	0.2	
m_h/m_o [c]	1.0	1.0	
ε	9.77	9.77	
$\Delta E_\mathrm{c}/\Delta E_\mathrm{v}$ [d]			70/30

[a] Refs. [154, 175, 145]
[b] Refs. [80, 163, 98]
[c] Refs. [80, 163, 98, 185, 128, 40]
[d] Refs. [44, 174, 99]

Chapter 6

Influence of Polarization Fields on the Disorder Broadening of Excitons

6.1 Introduction

The universal relation between the exciton absorption linewidth and the photoluminescence Stokes shift found for a wide range of quantum well samples [184] does not apply to (In,Ga)N/GaN QWs. For this material-system, experimental data exhibit a very large Stokes shift and a strong inhomogeneous broadening of emission and excitation features, from which it is even difficult to extract the position of the band gap energy (see Fig. 2) [33, 110, 35, 15, 172, 132, 153, 116, 126, 154, 175, 145, 105, 166, 129]. The underlying mechanisms are discussed controversially. As one possible reason for both features, exciton localization in strong compositional fluctuations resulting from phase separation in (In,Ga)N has been proposed [172, 41, 119, 32, 101, 125, 120, 111]. On the other hand, strong polarization fields along the QW-axis can explain the large redshift of the PL line without resorting to localization effects [165, 131, 64, 74, 142]. Up to now, however, only few theoretical investigations have been made to quantify the individual contributions of shifting- and broadening-mechanisms.

In this chapter, the exciton center-of-mass separation ansatz, described in chapter 1, is applied to investigate the influence of polarization fields on the disorder broadening of excitons in (In,Ga)N/GaN QWs. It has to be clarified whether polarization fields can be the origin of an emission line broadening-mechanism, as it has been discussed in literature [124, 65]. As a measure for the spectral width of optical density of states, the spectral width of the QW exciton center-of-mass potential in terms of its standard deviation is calculated in dependence on an average polarization field in the well. Both uncorrelated alloy fluctuation (AF) and in-plane-correlated interface roughness (IR) of one monolayer (ML) in each interface are considered. Not only the fluctuation of the band edges, but also the fluctuation of the long-range polarization field of spontaneous and strain-induced dipole moments is taken into account.

6.2 Theory

6.2.1 General Proceeding

As outlined in chapter 1, the fundamental assumption for the application of the center-of-mass separation is that the energetic contribution of the potential fluctuations δV_a to the QW exciton state is small compared to the binding energy. In this limit, the spectral broadening of the exciton center-of-mass potential can be calculated by averaging the fluctuation over the exciton relative wavefunction [188, 189, 10, 11]. For this purpose, a QW exciton model is adopted which was developed by Leavitt and Little [93]. This model is well suited even in the presence of polarization fields where electrons and holes are separated from each other along the QW axis. It consists of an incomplete adiabatic decoupling

$$\Phi = \Psi(\mathbf{R})\,\phi(\mathbf{r}, z_e - z_h)\,\psi(z_e, z_h)\,, \tag{6.1}$$

of the in-plane motion from the one perpendicular to it. The method is introduced in detail in appendix A.2.

The calculation of the spectral width of the center-of-mass potential (1.6) requires the functions $\phi(r, Z)$ and $\psi(z_e, z_h) \approx \varphi_e(z_e)\varphi_h(z_h)$ (see appendix A.2) and assumptions about the statistics of the potential fluctuation δV_a. For the relative function $\phi(r, Z)$, the exponential ansatz (A.13) is used. To calculate the subband functions $\varphi_a(z)$, the following considerations are made.

From a self-consistent solution of the one-dimensional Schrödinger-Poisson problem, described in chapter 4, it can be observed that the assumption of flat band edges in unstrained barriers in the vicinity of the well

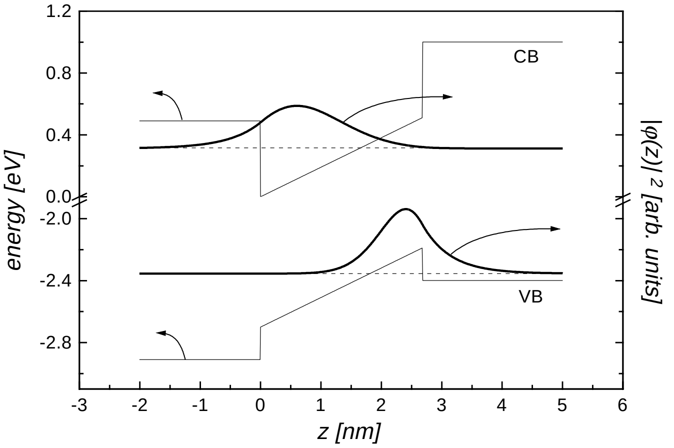

Figure 6.1: *Conduction- and valenceband alignment of a 10 monolayer ($\approx 2.6\,$nm) $\mathrm{In}_{0.2}\mathrm{Ga}_{0.8}\mathrm{N/GaN}$ QW with a piezoelectric constant for (In,Ga)N of $d_{31} = -0.9 \cdot 10^{-10}\,$cm/V (according to the formula $P = 2d_{31}(C_{11} + C_{12} - 2C_{13}^2/C_{33})\epsilon_{||}$ where $\epsilon_{||}$ is the (biaxial) strain component parallel to the QW plane)[64, 74] yielding $F_\mathrm{P} = 1.91\,$MV/cm. The electron and hole groundstate envelope subband functions are plotted at their respective energy positions.*

is justified if the cap layer is thick enough ($> 50\,$nm) and the background doping density is not too high ($< 2\cdot 10^{17}\,\mathrm{cm}^{-3}$). Thus, we use a QW potential (given here only for the conduction band)

$$V_e^{\mathrm{QW}}(z) = \begin{cases} \Delta_e & z < 0 \\ eF_\mathrm{P} z & 0 \le z < d_\mathrm{QW} \\ \Delta_e + eF_\mathrm{P} d & d_\mathrm{QW} \le z\,, \end{cases} \tag{6.2}$$

with a net polarization field F_P inside the well of width d_QW. The conduction band-offset is described by Δ_e. Consequently, the subband function of the confined groundstate is given by exponential functions in the barriers and Airy functions in the well:

$$\varphi_e(z) = \begin{cases} c_+\,\mathrm{e}^{\kappa_+ z} & z < 0 \\ a\,\mathrm{Ai}\left[(z - E_e^{\mathrm{QW}}/eF_\mathrm{P})\,\vartheta\right] + & \\ \quad b\,\mathrm{Bi}\left[(z - E_e^{\mathrm{QW}}/eF_\mathrm{P})\,\vartheta\right] & 0 \le z < d_\mathrm{QW} \\ c_-\,\mathrm{e}^{-\kappa_- z} & d_\mathrm{QW} \le z\,, \end{cases} \tag{6.3}$$

where

$$\begin{aligned}
\kappa_+ &= \sqrt{\frac{2m_e}{\hbar^2}\left(\Delta_e - E_e^{\mathrm{QW}}\right)}\,, \qquad (6.4)\\
\kappa_- &= \sqrt{\frac{2m_e}{\hbar^2}\left(\Delta_e - E_e^{\mathrm{QW}} + eF_{\mathrm{P}}d_{\mathrm{QW}}\right)}\,, \qquad (6.5)\\
\vartheta &= \left(\frac{2m_eF_{\mathrm{P}}}{\hbar^2}\right)^{1/3}\,. \qquad (6.6)
\end{aligned}$$

The QW potentials and subband functions are depicted in Fig. 6.1. To find the coefficients a, b, c_-, c_+ and energy E_e^{QW}, the continuity conditions for $\varphi_e(z)$ and $\frac{d}{dz}\varphi_e(z)$ at the two interfaces have to be written down. This is a system of four equations, including all unknowns. The additionally required condition is the normalization of the wavefunction. This problem was solved numerically by deriving an equation for E_e^{QW} and finding the roots with the Newton-Raphson method [137]. The coefficients are given by

$$\begin{aligned}
a &= 1 \qquad (6.7)\\
b &= -\left.\frac{\kappa_-\,\mathrm{Ai}(x) + \vartheta\,\mathrm{Ai}'(x)}{\vartheta\,\mathrm{Bi}'(x) + \kappa_-\,\mathrm{Bi}(x)}\right|_{x=\vartheta(d_{\mathrm{QW}}-E_e^{\mathrm{QW}}/F_{\mathrm{P}})} \qquad (6.8)\\
c_- &= a\,\mathrm{Ai}(-\vartheta\,E_e^{\mathrm{QW}}/F_{\mathrm{P}}) + b\,\mathrm{Bi}(-\vartheta\,E_e^{\mathrm{QW}}/F_{\mathrm{P}}) \qquad (6.9)\\
c_+ &= \mathrm{e}^{\kappa_-\,d}\left[a\,\mathrm{Ai}\left((d_{\mathrm{QW}} - E_e^{\mathrm{QW}}/F_{\mathrm{P}})\vartheta\right) + \right.\\
&\qquad \left. b\,\mathrm{Bi}\left((d_{\mathrm{QW}} - E_e^{\mathrm{QW}}/F_{\mathrm{P}})\vartheta\right)\right]\,. \qquad (6.10)
\end{aligned}$$

Now the function $\varphi_e(z)$ has to be normalized. The valence subband function can be found from analogy. The description of the potential fluctuation is given in the following section.

6.2.2 Fluctuation Statistics

To describe the disorder broadening of an excitonic resonance due to AF and IR in a QW without polarization fields, there is a well established standard theory [188, 189]. This model is extended here by also including the fluctuation of the long-range spontaneous and strain-induced polarization field, which is present in wurtzite phase GaN-based heterostructures. Both a value for the band gap energy and for the dipole moment is assigned to a InN or GaN unit. The width of the center-of-mass potential, reflected in the width of the exciton optical density of states, is obtained by an averaging procedure with respect to the subband functions and the exciton in-plane relative wavefunction.

First, we define two statistic variables

$$\eta_i = \begin{cases} 1 & \text{if cell } i \text{ is an InN cell} \\ 0 & \text{if not} \end{cases} \tag{6.11}$$

for the AF and

$$\zeta_i = \begin{cases} 1 & \text{if cell } i \text{ belongs to the well material} \\ 0 & \text{if not} \end{cases} \tag{6.12}$$

for the IR with expectation values

$$< \eta_i >_{\mathrm{QW}} = \bar{x} \quad \text{and} \quad < \zeta_i >_{\mathrm{ML}} = f_j \, . \tag{6.13}$$

In case of η_i the averaging comprises the whole QW material so that $\bar{x}$ is the mean indium content of the QW, and in case of ζ_i the averaging comprises only the monolayer which cell i belongs to ($j = j(i)$ is the index of this monolayer in the following). The AF is assumed to be uncorrelated

$$< \eta_i \, \eta_{i'} > = \bar{x}^2 + \delta_{ii'} \, \bar{x}(1-\bar{x}) \, , \tag{6.14}$$

and the IR is assumed to have a Gaussian in-plane correlation with correlation length L_{c}

$$\begin{aligned} < \zeta_i \, \zeta_{i'} > &= f_j \, f_{j'} + \delta_{jj'} \exp\left(-\frac{r_{ii'}^2}{2\,L_{\mathrm{c}}^2} \right) f_j \, (1-f_j) \\ &= f_j \, f_{j'} + \mathrm{C}_{ii'} \, , \end{aligned} \tag{6.15}$$

where $r_{ii'}$ is the distance between cell i and cell i', and $\mathrm{C}_{ii'}$ denotes the correlation function. The roughness at the two sides of the QW is assumed to be uncorrelated. Since an IR of only one monolayer in each interface is considered, there is no need to care about the correlation along the QW axis within the interface.

Now we can express the fluctuation of the band edges due to AF and IR

$$\begin{align} E_a(\mathbf{r}_i, x) &= \zeta_i \, [E_a(\bar{x}) + (\eta_i - \bar{x}) \, \partial_x E_a(x)|_{x=\bar{x}} \,] + (1-\zeta_i) \, E_a(x=0) \tag{6.16} \\ &= \, < E_a(\mathbf{r}_i, x) > + \, \delta E_a(\mathbf{r}_i, x) \quad (a = e, h) \tag{6.17} \end{align}$$

where

$$\begin{aligned} < E_a(\mathbf{r}_i, x) > &= E_a(x=0) + f_j\,\Delta E_a \qquad \text{and} && (6.18)\\ \delta E_a(\mathbf{r}_i, x) &= (\zeta_i - f_j)\,\Delta E_a + \zeta_i\,(\eta_i - \bar{x})\,\partial_x E_a(x)|_{x=\bar{x}} \\ &= \delta V_a^{\mathrm{R}}(\mathbf{r}_i, x) + \delta V_a^{\mathrm{A}}(\mathbf{r}_i, x)\,. && (6.19) \end{aligned}$$

$\Delta E_a = E_a(\bar{x}) - E_a(0)$ denotes the difference in band edge energy between $\mathrm{In}_{\bar{x}}\mathrm{Ga}_{1-\bar{x}}\mathrm{N}$ and GaN. In the following we use the abbreviation $\partial E_a := \partial_x E_a(x)|_{x=\bar{x}}$. The first term in equation (6.16) gives the band edge inside the QW material and the second term in the barrier material. The first term in equation (6.19) gives the fluctuation contribution of the IR and the second term of the AF. The autocorrelation of the band edge fluctuation is given by

$$\begin{aligned} < \delta E_a(\mathbf{r}_i)\,\delta E_b(\mathbf{r}_{i'}) > &= < \delta V_a^{\mathrm{R}}(\mathbf{r}_i)\,\delta V_b^{\mathrm{R}}(\mathbf{r}_{i'}) > + < \delta V_a^{\mathrm{A}}(\mathbf{r}_i)\,\delta V_b^{\mathrm{A}}(\mathbf{r}_{i'}) >= \\ &= \Delta E_a\,\Delta E_b\,\mathrm{C}_{ii'} + \partial E_a\,\partial E_b\,\delta_{ii'}\,\bar{x}(1-\bar{x})\,f_j\,. && (6.20) \end{aligned}$$

There are no mixed terms because AF and IR are assumed to be uncorrelated among each other.

Up to this point, the treatment of the fluctuation statistics for the description of the band edges in ternary materials has been developed and applied by others before [188, 189]. We now additionally consider the fluctuation of the polarization which arises from the difference in spontaneous and strain-induced polarization between GaN and strained InN. In analogy to the treatment of the band edges, a dipole moment which corresponds to the respective binary material is assigned to each III-N unit before averaging over the exciton wavefunction. Thus, the total polarization P can be written in the same way as the band edges as a function of the statistic variables

$$\begin{aligned} P(\mathbf{r}_i, x) &= \zeta_i\,[P(\bar{x}) + (\eta_i - \bar{x})\,\partial_x P(x)|_{x=\bar{x}}] + (1-\zeta_i)\,P(x=0) && (6.21)\\ &= < P(\mathbf{r}_i, x) > + \delta P(\mathbf{r}_i, x) && (6.22) \end{aligned}$$

where

$$\begin{aligned} < P(\mathbf{r}_i, x) > &= P(x=0) + f_j\,\Delta P \qquad \text{and} && (6.23)\\ \delta P(\mathbf{r}_i, x) &= (\zeta_i - f_j)\,\Delta P + \zeta_i\,(\eta_i - \bar{x})\,\partial_x P(x)|_{x=\bar{x}}\,. && (6.24) \end{aligned}$$

$\Delta P = P_{\mathrm{In}_{\bar{x}}\mathrm{Ga}_{1-\bar{x}}\mathrm{N}} - P_{\mathrm{GaN}}$ denotes the difference in polarization between $\mathrm{In}_{\bar{x}}\mathrm{Ga}_{1-\bar{x}}\mathrm{N}$ and GaN. If we assume a linear dependence of the polarization

$P(\bar{x})$ of $\mathrm{In}_{\bar{x}}\mathrm{Ga}_{1-\bar{x}}\mathrm{N}$ on the mean indium content $\bar{x}$, the derivative is independent of $\bar{x}$ and given by $\partial P := \partial_x P(x) = P_{\mathrm{InN}} - P_{\mathrm{GaN}}$. The polarization potential reads

$$\delta V_a^{\mathrm{P}}(\mathbf{r}_i, x) = \frac{V_{\mathrm{EC}}\, e_a}{8\pi\epsilon\epsilon_o} \sum_{i'} \frac{(z_i - z_{i'})\, \delta P(\mathbf{r}_i, x)}{|\mathbf{r}_i - \mathbf{r}_{i'}|^3}\,, \tag{6.25}$$

where V_{EC} is the volume of the elementary cell.

6.2.3 The Spectral Width of the Exciton Center-of-Mass Potential

The spectral width of the center-of-mass potential is calculated in terms of the standard deviation $\sigma =< V_{\mathrm{CM}}^2 >^{1/2}$ which can be regarded as an upper bound for the width of the exciton optical density because of the motional narrowing effect [188, 189]. This provides a measure for the dependence of the disorder broadening of an excitonic resonance on the strength of the average polarization field inside the QW. First we have to add all contributions to the potential fluctuation

$$\delta V_a = \delta V_a^{\mathrm{R}} + \delta V_a^{\mathrm{A}} + \delta V_a^{\mathrm{P}}\,. \tag{6.26}$$

δV_a^{R} and δV_a^{A} are defined in equation (6.19). δV_a^{P} is defined in equation (6.25) and comprises AF as well as IR. The center-of-mass potential (1.6) can be written as

$$V_{\mathrm{CM}}(\mathbf{R}) = \sum_{a=e,h} \int dz_a\, \varphi_a^2(z_a) \int d^2 r_a\, \tilde{g}_a(r_a, z_a)\, \delta V_a(\mathbf{R} + r_a, z_a) \tag{6.27}$$

where

$$\tilde{g}_a(r_a, z_a) = \beta_a^2 \int dz_b\, \varphi_b^2(z_b)\, \phi^2(\beta_a r_a, z_a - z_b) \quad (a, b = e, h; a \neq b)\,, \tag{6.28}$$

$r_a = r/\beta_a$, $\beta_a = m_a/\mu$, and ϕ is the exciton relative wavefunction according to expression (A.13). The square of the standard deviation can be written as a sum of three contributions

$$\sigma^2 =< V_{\mathrm{CM}}^2 >= \sigma_{ee}^2 + \sigma_{hh}^2 + 2\,\sigma_{eh}^2 \tag{6.29}$$

where

$$\sigma_{ab}^2 = \int dz_a \, dz_b \, \varphi_a^2(z_a) \, \varphi_b^2(z_b) \int d^2 r_a \, d^2 r_b \, \tilde{g}_a(r_a, z_a) \, \tilde{g}_b(r_b, z_b) < \delta V_a \, \delta V_b > \; . \tag{6.30}$$

Because of the three contributions in the potential fluctuation (6.26), each of the terms $< \delta V_a \, \delta V_b >$ comprises $3^2 = 9$ contributions two of which are zero because AF and IR are uncorrelated among each other. The expressions for the other terms are given here:

$$\begin{aligned}
\sigma^2_{\mathrm{A}_a\mathrm{A}_b} &= \partial E_a \, \partial E_b \, \bar{x}(1-\bar{x}) \frac{V_{\mathrm{EC}}}{2} \, 2\pi \int_0^\infty dr r \int_0^{d_{\mathrm{QW}}} dz \, \varphi_a^2(z) \, \varphi_b^2(z) \times \\
&\quad \times \tilde{g}_a(r,z) \, \tilde{g}_b(r,z) && (6.31) \\
\sigma^2_{\mathrm{R}_a\mathrm{R}_b} &= \Delta E_a \, \Delta E_b \, d^2_{\mathrm{ML}} \, 4\pi^2 \int_0^\infty dr r \int_0^\infty dr' r' \exp\left(-\frac{r^2 + r'^2}{2\,L_{\mathrm{c}}^2}\right) \mathrm{I}_0\left(\frac{r\,r'}{L_{\mathrm{c}}^2}\right) \times \\
&\quad \times \sum_{z_i = 0, d_{\mathrm{QW}}} f_{j(i)}(1 - f_{j(i)}) \, \varphi_a^2(z_i) \, \varphi_b^2(z_i) \, \tilde{g}_a(r, z_i) \, \tilde{g}_b(r', z_i) && (6.32) \\
\sigma^{2\,(\mathrm{AF})}_{\mathrm{P}_a\mathrm{P}_b} &= \frac{e_a e_b}{\kappa^2} \, (\partial P)^2 \, \bar{x}(1-\bar{x}) \, \frac{V_{\mathrm{EC}}}{2} \, d_{\mathrm{ML}} \, 2\pi \sum_{z_i \in \mathrm{QW}} \int_0^\infty dr r \, \tilde{q}_a(r, z_i) \, \tilde{q}_b(r, z_i) && (6.33) \\
\sigma^{2\,(\mathrm{IR})}_{\mathrm{P}_a\mathrm{P}_b} &= \frac{e_a e_b}{\kappa^2} \, (\Delta P)^2 \, d^2_{\mathrm{ML}} \, 4\pi^2 \sum_{z_i = 0, d_{\mathrm{QW}}} f_{j(i)}(1 - f_{j(i)}) \int_0^\infty dr r \, \tilde{q}_a(r, z_i) \times \\
&\quad \times \int_0^\infty dr' r' \exp\left(-\frac{r^2 + r'^2}{2\,L_{\mathrm{c}}^2}\right) \mathrm{I}_0\left(\frac{r r'}{L_{\mathrm{c}}^2}\right) \tilde{q}_b(r', z_i) && (6.34) \\
\sigma^{2\,(\mathrm{AF})}_{\mathrm{P}_a\mathrm{E}_b} &= \frac{e_a}{\kappa} \, \partial P \, \partial E_b \, \bar{x}(1-\bar{x}) \, \frac{V_{\mathrm{EC}}}{2} \, d_{\mathrm{ML}} \, 2\pi \sum_{z_i \in \mathrm{QW}} \varphi_b^2(z_i) \times \\
&\quad \times \int_0^\infty dr r \, \tilde{q}_a(r, z_i) \, \tilde{g}_b(r, z_i) && (6.35) \\
\sigma^{2\,(\mathrm{IR})}_{\mathrm{P}_a\mathrm{E}_b} &= \frac{e_a}{\kappa} \, \Delta P \, \Delta E_b \, d^2_{\mathrm{ML}} \, 4\pi^2 \sum_{z_i = 0, d_{\mathrm{QW}}} f_{j(i)}(1 - f_{j(i)}) \, \varphi_b^2(z_i) \int_0^\infty dr r \, \tilde{q}_a(r, z_i) \; \times \\
&\quad \times \int_0^\infty dr' r' \exp\left(-\frac{r^2 + r'^2}{2\,L_{\mathrm{c}}^2}\right) \mathrm{I}_0\left(\frac{r r'}{L_{\mathrm{c}}^2}\right) \tilde{g}_b(r', z_i) \, , && (6.36)
\end{aligned}$$

where d_{ML} is the thickness of a monolayer. The abbreviation

$$\tilde{q}_a(r,z) = \int_{-\infty}^{\infty} dz'\, \varphi_a^2(z')\,(z'-z) \int_0^{\infty} dr' r'\, \tilde{g}_a(r',z)\, \frac{4\sqrt{u+v}}{u^2-v^2}\, \mathrm{E}\left(\frac{2\,v}{u+v}\right) \tag{6.37}$$

was used, where $u = (z'-z)^2 + r'^2 + r^2$, $v = 2r'r$, and

$$\mathrm{E}(x) = \int_0^{\pi/2} d\alpha \sqrt{1 - x\sin^2\!\alpha} \tag{6.38}$$

is the complete elliptic integral of the second kind. Furthermore, it was used that

$$\int_0^{2\pi} d\varphi \exp\left(x\cos\varphi\right) = 2\pi\, \mathrm{I}_0(x) \tag{6.39}$$

where $\mathrm{I}_0(x)$ is the modified Bessel function of order zero. All integrals and summations in equations (6.31) to (6.37) are actual summations over III-N unit cells of volume $V_{\mathrm{EC}}/2 = \sqrt{3}\,a^2c/4$, where a and c are the lattice constants of the wurtzite lattice. Since all consideration are made only in envelope function approximation, the values of the functions should vary smoothly with respect to the spatial scale of the unit cell. If this holds, summations can be approximated by integrals. If not, the summations are executed after averaging the function over the unit cell (in case of divergency in the exciton relative wavefunction for $r \to 0$).

Some remarks on model and material parameters entering the calculation: To determine the strength of the polarization fields along the QW-axis in a (In,Ga)N/GaN QW structure, various estimates for the piezoelectric (or the electromechanic) coefficients as well as for the spontaneous polarizations of GaN and InN have been made [165, 64, 74, 17, 23, 100]. Because of the large scattering of values given in literature and because of the sensitive dependence of the net polarization field F_{P} in the QW on various sample parameters, as described in chapter 4, the following calculations are made as a function of F_{P}.

Another uncertainty concerns the band gap bowing parameter of $\mathrm{In}_x\mathrm{Ga}_{1-x}\mathrm{N}$ [132, 153, 116, 126, 154, 175, 145, 105, 166, 129, 179, 89, 14, 13]. Here, a value of 2.5 eV is assumed, obtained from recent optical transmission and photoreflectance experiments [154, 175, 145]. The calculation was executed for a 10 monolayer ($\approx$ 2.6 nm) $\mathrm{In}_{0.2}\mathrm{Ga}_{0.8}\mathrm{N}$/GaN QW. Further material parameters are listed in Table 6.1.

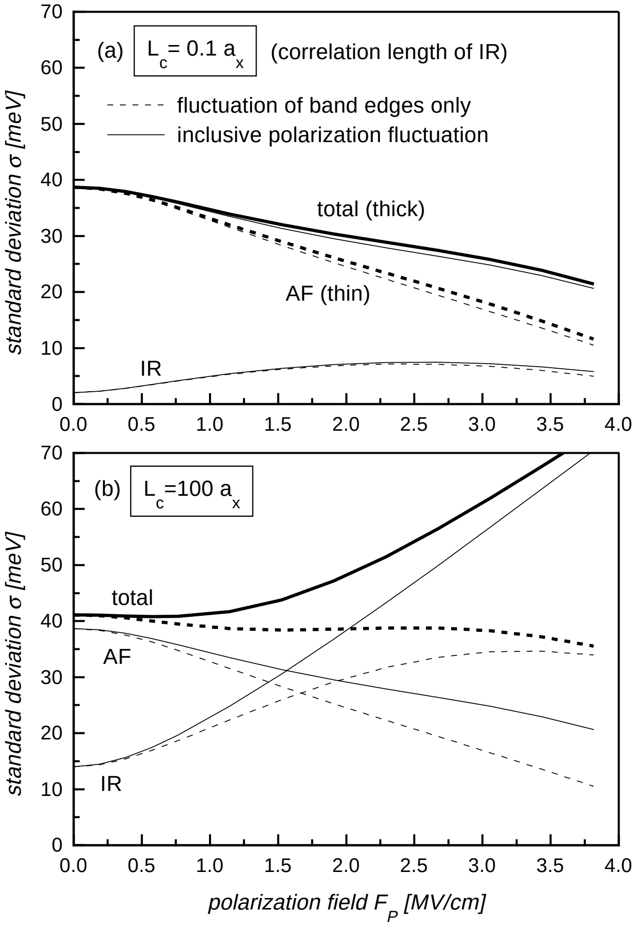

Figure 6.2: *Standard deviation σ of the QW exciton center-of-mass potential spectrum versus the net polarization field F_P inside the well for a 10 monolayer ($\approx 2.6\,\mathrm{nm}$) $In_{0.2}Ga_{0.8}N/GaN$ QW. AF: uncorrelated alloy fluctuation. IR: in-plane-correlated interface roughness with correlation length L_c. For fields larger than 4 MV/cm, the hole has no bound state in the QW anymore.*

6.3 Results

First, we discuss the results obtained when considering only the fluctuation of the band edges (6.19), given by the dashed curves in Fig. 6.2, where σ

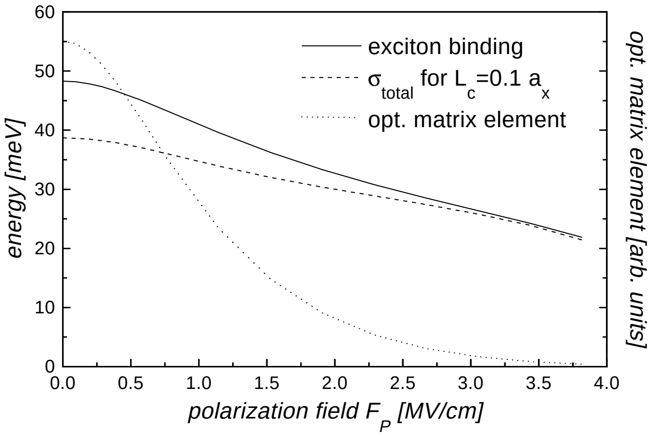

Figure 6.3: *Exciton binding energy and exciton optical matrixelement as a function of the net polarization field F_P in the QW.*

is plotted versus the net polarization field F_P for a short-range (a) and a long-range (b) correlation of the IR ($L_\mathrm{c} = 0.1\,a_\mathrm{x}$ and $L_\mathrm{c} = 100\,a_\mathrm{x}$, respectively, where $a_\mathrm{x} = \hbar^2 4\pi\varepsilon\varepsilon_o/(e^2\mu)$ is the bulk exciton Bohr radius). The total broadening, given by $\sigma_\mathrm{total} = \sqrt{\sigma_\mathrm{AF}^2 + \sigma_\mathrm{IR}^2}$, is only about 40 meV for zero field, which is much smaller than experimentally measured linewidths. The AF contribution further decreases with increasing F_P, because of an increasing exciton in-plane extension (and, thus, an increasing averaging volume), and because of the penetration of the particles into the binary barriers. This spatial separation of the carriers (mainly the one along the QW-axis) results also in a decrease of the binding energy and in a dramatic reduction of the exciton optical matrix element $g(0,0)^2|\int dz\varphi_e^*(z)\varphi_h(z)|^2$ with increasing polarization field F_P (see Fig. 6.3). Furthermore, it leads to an increasing IR broadening contribution, which sensitively depends on the correlation length L_c. For the chosen wellwidth, always a decreasing σ_total is obtained, even for a very large correlation length $L_\mathrm{c} \gg a_\mathrm{x}$. This result is in contradiction to the following consideration. In the limit $L_\mathrm{c} \to \infty$, the QW consists of extended regions of different constant well-widths. This leads to a decomposition of the spectrum into separate lines, a long known phenomenon in QWs like e.g. GaAs/(Al,Ga)As [27]. In the high field limit, the spectral separation of these lines—and thus σ—increases linearly with the field F_P.

This discrepancy can be resolved by additionally taking into account the potential fluctuations of the polarization (6.25). For $L_\mathrm{c} \ll a_\mathrm{x}$, the consideration of δV_a^P only smoothes the decrease of σ_AF but leaves σ_IR essentially unchanged (solid curves in Fig. 6.2 a). Up to a correlation length of $L_\mathrm{c} \approx a_\mathrm{x}$ the polarization field leads to a decrease of σ_total (see Fig. 6.4). In this case, the exciton volume is larger than the average scale of the IR and the integration over the exciton volume still smoothes the roughness. In the opposite case $L_\mathrm{c} \gg a_\mathrm{x}$, the polarization fluctuations yield indeed the expected linear increase of σ_IR with the field. The full spectrum consists of the superposition of three lines corresponding to $(n-1)$, n, and $(n+1)$ ML thick well regions, each of which is broadened by AF. Above about 2.4 MV/cm, the spectral separation of two neighbouring lines becomes larger than their full width at half maximum (FWHM).

To check the validity of the center-of-mass separation, we have to compare the results for σ_total in case of a short-range IR with the exciton binding energy. It is found that the rough criterion $\sigma < E_\mathrm{x}^\mathrm{b}$ (which comes from FWHM $\approx 2.35\,\sigma$ for a Gaussian spectrum and the assumption of a motional narrowing factor ≤ 0.5 [188]) is fulfilled although the data are close to the border of validity (see Fig. 6.3). Therefore it can be expected that the effects are qualitatively well described but without high quantitative accuracy.

6.4 Summary

It was demonstrated that the exciton center-of-mass potential experiences narrowing and splitting into individual lines as a consequence of a polarization field in case of uncorrelated alloy fluctuation and in-plane-correlated single monolayer interface roughness. However, none of these phenomena have been observed experimentally. Therefore, it must be concluded that other effects such as carrier localization by correlated compositional fluctuations have to be invoked for explaining the strong broadening effects in (In,Ga)N/GaN QWs.

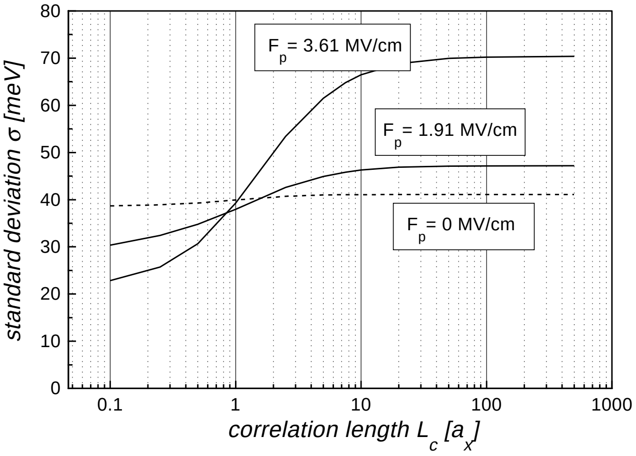

Figure 6.4: *Standard deviation σ of the QW exciton center-of-mass potential spectrum versus the in-plane correlation length L_{c} of the IR for two literature values[64, 17] for the net polarization field F_{P} in a 10 monolayer ($\approx 2.6\,\mathrm{nm}$) $\mathrm{In}_{0.2}\mathrm{Ga}_{0.8}\mathrm{N/GaN}$ QW.*

Table 6.1: *Calculation parameters used in this chapter.*

Parameter	GaN	InN	$\mathrm{In}_x\mathrm{Ga}_{1-x}\mathrm{N}$
E_{g} [eV]	3.4	1.9	
b (bowing) [eV] [a]			2.5
m_e/m_{o} [b]	0.2	0.2	
m_h/m_{o} [c]	1.0	1.0	
ε	9.5	9.5	
$\Delta E_{\mathrm{c}}/\Delta E_{\mathrm{v}}$ [d]			70/30

[a] Refs. [154, 175, 145]
[b] Refs. [80, 163, 98]
[c] Refs. [80, 163, 98, 185, 128, 40]
[d] Refs. [44, 174, 99]

Summary of Results

- A theoretical treatment of quantum well exciton and biexciton states in the limit of weak localization is presented, using a center-of-mass separation ansatz. It shows that the localization energy of the biexciton is more than twice as large as that of the exciton due to the universal behaviour of localization in weak two-dimensional potentials which is ruled only by the potential "volume" $\int d^2r|V(\mathbf{r})|$ and the mass of the localized particle. A useful simple model of the QW biexciton wavefunction is developed which provides good agreement with the results obtained with an extensive numerical solution.

- The limit of strong localization of QW excitons and higher exciton complexes $X_{n\geq 2}$ is investigated with a density functional calculation. It is demonstrated that states at least up to X_4 may localize in nm-scale potential boxes caused by indium phase separation in (In,Ga)N/GaN QWs. The successive recombination of a localized X_4 results in an emission spectrum of four lines separated by about $10-15\,\mathrm{meV}$ in the example presented here. Since the spectral distances between these transitions are small compared to the linewidths experimentally observed in (In,Ga)N-based structures, it will be necessary to apply spatially resolved "single-dot" spectroscopy to resolve them in a high-excitation experiment.

- A systematic investigation of the influence of the sample design of (In,Ga)N/GaN QW structures on optical transition energy and oscillator strength reveals the importance of space charge layers with regard to screening of polarization fields along the QW-axis. Based on a self-consistent solution of the Schrödinger-Poisson equations, the overall situation of the macroscopic spontaneous and piezoelectric polarization fields is discussed in dependence on various substantial sample parameters. It is found that the position of a QW in the sample with respect to an extended surface depletion layer—which is shown to exist in n-type Ga-face grown material—severely affects transition energy and electron-hole overlap. Due to the spatial variation of the field strength in this surface depletion layer, the optical transition spectrum of a Ga-face grown multiple-QW can display shoulders or even a multiple-peak structure.

- Indium surface segregation results in a blueshift of the transition energy compensating up to one third of the quantum confined Stark shift produced by the polarization field. This blueshift is accompanied by a decrease of the electron-hole overlap.

- Polarization fields in (In,Ga)N/GaN multiple-QWs result in a smoothing of the step-like single-particle absorption spectrum. Apart from the contribution of compositional fluctuations, the fields have significant influence on the shape of the spectrum via the abrogation of the nearly diagonality of inter-subband transitions and via the mini-band dispersion of higher coupled states in case of a periodic structure.

- A line broadening-mechanism due to polarization fields in (In,Ga)N/GaN QWs, as sometimes discussed in literature, could not be confirmed. Assuming uncorrelated (In,Ga)N alloy and in-plane-correlated interface roughness of one monolayer in each interface, the calculation of the spectral width of the QW exciton center-of-mass potential yields a narrowing with increasing average field. This is a result of the penetration of the carriers into the barriers and of an increasing exciton volume. In case of a long-range interface roughness, a splitting of the spectrum into individual lines can be predicted.

*

Appendix A

The Quantum Well Exciton

The restriction of the freedom of motion by the confining potential of a QW has a prominent effect on the exciton binding energy and the spatial extension of its relative wavefunction. Various theoretical models have been developed for studying low-dimensional excitons in QWs, quantum wires, or quantum dots [12, 61, 22, 52, 9]. In general, the more precise the results should be, the higher becomes the numerical expenditure of the model.

The relative wavefunction of a QW exciton is needed in chapter 2 to compare the localization behaviour of the QW biexciton with respect to a correspondingly described exciton. In chapter 6, the wavefunction is needed to calculate the disorder broadening in the presence of polarization fields. Here, we outline three simple methods to calculate the QW exciton wavefunction and binding energy, used in the mentioned chapters.

A.1 Isolated Subband Approximation and Center-of-Mass Separation

The first steps of this approach follow the procedure, described in chapter 1 for the case of only two particles, one electron and one hole. A full separation of the z-coordinates from the in-plane movement is made, so that the in-plane relative wavefunction $\phi(\mathbf{r})$ depends only on the electron-hole relative coordinate $\mathbf{r}$. Since the system is invariable to translation of the center-of-mass within the QW plane and to rotation of $\mathbf{r}$, the total wavefunction (1.4) can be rewritten as

$$\Phi = \mathrm{e}^{i\mathbf{QR}}\,\phi(r)\prod_{a=e,h}\varphi_a(z_a) \tag{A.1}$$

where $r = |\mathbf{r}_e - \mathbf{r}_h|$ is the in-plane inter-particle distance, $\mathbf{Q}$ is the in-plane center-of-mass momentum, and $\mathbf{R} = (m_e\mathbf{r}_e + m_h\mathbf{r}_h)/(m_e + m_h)$ is the in-plane center-of-mass coordinate. The plane-wave solution for the center-of-mass in-plane motion is a consequence of the translational symmetry of the problem.

Multiplying Schrödinger equation (1.1) with the complex conjugates of the envelope subband functions $\varphi_a(z_a)$ $(a = e, h)$ and integrating with respect to the z-coordinates yields

$$\left[-\frac{\hbar^2}{2\mu}\Delta_r + \tilde{U}_\mathrm{C}(r)\right]\phi(r) = \left(E - \sum_a E_a^\mathrm{QW}\right)\phi(r)\,, \tag{A.2}$$

where $\mu = m_e m_h/(m_e + m_h)$ is the reduced exciton mass and E_a^QW are subband levels. Due to the rod-like extension of the charge densities $\pm e\,|\varphi_a(z_a)|^2$ $(a = e, h)$ along the QW axis for small in-plane distances, the QW Coulomb potential

$$\tilde{U}_\mathrm{C}(r) = -\frac{e^2}{4\pi\varepsilon\varepsilon_o}\int dz_e\,dz_h\,\frac{|\varphi_e(z_e)|^2\,|\varphi_h(z_h)|^2}{\sqrt{r^2 + (z_e - z_h)^2}} \tag{A.3}$$

has a logarithmic singularity for $r \to 0$, in contrast to the $1/r$-singularity for the 3D bulk exciton.

After solving the subband Schrödinger equations (1.3), the QW Coulomb potential (A.3) can be evaluated numerically, and the in-plane relative Schrödinger equation (A.2) can be solved to obtain the QW exciton relative wavefunction and binding energy. This has been carried out with the numerical method of inverse vector iteration [138]. As an example, the binding energy of an exciton in a $\mathrm{Zn}_{1-x}\mathrm{Cd}_x\mathrm{Se}$ /ZnSe QW is plotted in Figs. A.1 (a), (b), and (c) as a function of the QW width d_QW for cadmium concentrations $x = 0.1$, 0.2, and 0.3, respectively (up triangles). As a consequence of the reduced kinetic freedom, the binding energy is enhanced compared to the 3D excitonic Rydberg of $Ry_\mathrm{x} = 20.3\,\mathrm{meV}$, indicated by arrows. In the limiting cases of a very narrow and a very wide QW, the extension of the subband functions along the QW axis is larger resulting in a more 3D character of the single-particle motion than in case of strongly localized functions.

A.2 The Method of Leavitt and Little

Leavitt and Little [93] have developed a method to estimate binding energy and relative wavefunction of the ground state of an exciton confined in an arbitrarily shaped heterostructure potential. This model is well suited even in the presence of polarization fields along the QW axis. It consists of an incomplete adiabatic decoupling of the in-plane motion from the one perpendicular to it. It considers the electron-hole relative motion not only within the QW plane but also perturbatively along the QW axis. Thus, this model also expresses in a better way the intermediate dimensionality of a QW between 2D and 3D.

To introduce this approach we again follow the procedure described in chapter 1. In contrast to the model in section A.1, the relative wavefunction now depends also on the distance $Z = z_e - z_h$ between the particles along the z-direction

$$\Phi = \mathrm{e}^{i\mathbf{QR}}\,\phi(r, Z)\,\psi(z_e, z_h)\,, \tag{A.4}$$

where $r = |\mathbf{r}_e - \mathbf{r}_h|$ is the in-plane inter-particle distance, $\mathbf{Q}$ is the in-plane center-of-mass momentum, and $\mathbf{R} = (m_e\mathbf{r}_e + m_h\mathbf{r}_h)/(m_e + m_h)$ is the in-plane center-of-mass coordinate. The plane-wave solution for the center-of-mass in-plane motion is a consequence of the translational symmetry of the problem. The separation of electron and hole coordinates concerning the motion along the QW axis in the function ψ is not formally introduced here, but will be actually possible later as an approximation. ψ depends on the absolute position of the carriers along the QW axis, ϕ depends on their relative motion. This approach was first used by Born and Oppenheimer [19] in order to describe a molecule by separating the electronic from the nuclear coordinates: the electronic motion is much faster than the nuclear motion. The ions are moving in an effective potential created by the average motion of the electrons. Here r, the in-plane relative motion, is associated to a fast motion and Z is associated to a slow motion. The function $\phi(r, Z)$ is the eigenfunction of a 2D Hamiltonian, describing the Coulomb interaction between an electron and a hole confined to the planes $z = z_e$ and $z = z_h$, respectively:

$$\left[-\frac{\hbar^2}{2\mu}\,\frac{1}{r}\frac{\partial}{\partial r}\left(r\,\frac{\partial}{\partial r}\right) - \frac{e^2}{\kappa\,\sqrt{r^2 + Z^2}}\right]\phi(r, Z) = -E^{(\mathrm{2D})}(Z)\,\phi(r, Z)\,, \tag{A.5}$$

where $\mu = m_e m_h/(m_e + m_h)$ is the reduced exciton mass. This radial Schrödinger equation depends parametrically on Z via the Coulomb potential and is independent of the potential shape along the QW axis. Therefore, also the eigenvalue $E^{(2\mathrm{D})}(Z)$ is independent of the QW potential. The function ϕ must be normalized for all values of Z:

$$\int d^2r \, |\phi(r, Z)|^2 = 1 \, . \tag{A.6}$$

To derive an effective Hamiltonian that acts on ψ only, we multiply the Hamiltonian of the base Schrödinger equation (1.1) for $\mathbf{Q} = 0$ from the left side with $\phi^*\psi^*$ and integrate with respect to the in-plane relative coordinate $\mathbf{r}$ and the z-coordinates. This yields

$$\begin{aligned} < H >= \int dz_e \, dz_h \Bigg\{ \int d^2r \sum_{a=e,h} -\frac{\hbar^2}{2m_a} \left(\frac{\partial}{\partial z_a} \, \phi \, \psi \right)^2 + \\ \left[\sum_{a=e,h} V_a^{\mathrm{QW}}(z_a) - E^{(2\mathrm{D})}(Z) \right] \psi^2 \Bigg\} \Big/ \int dz_e \, dz_h \, \psi^2 \, . \end{aligned} \tag{A.7}$$

This can be written as

$$\begin{aligned} < H >= \int dz_e \, dz_h \Bigg\{ \sum_{a=e,h} -\frac{\hbar^2}{2m_a} \left(\frac{\partial}{\partial z_a} \, \psi \right)^2 + \\ + \left[\sum_{a=e,h} V_a^{\mathrm{QW}}(z_a) - E^{(2\mathrm{D})}(Z) + W^{\mathrm{c}}(Z) \right] \psi^2 \Bigg\} \Big/ \int dz_e \, dz_h \, \psi^2 \end{aligned} \tag{A.8}$$

where

$$W^{\mathrm{c}}(Z) = \frac{\hbar^2}{2\mu} \, 2\pi \int_0^\infty dr \, r \, \left| \frac{\partial}{\partial Z} \, \phi(r, Z) \right|^2 \tag{A.9}$$

is the kinetic energy of the electron-hole relative motion along the QW axis described by $\phi(r, Z)$. It was used that

$$\int dz_a \, d^2r \, \phi^* \psi^* \left[-\frac{\hbar^2}{2m_a} \frac{\partial^2}{\partial z_a^2} \, (\phi \, \psi) \right] = \int dz_a \, d^2r \, \frac{\hbar^2}{2m_a} \left[\frac{\partial}{\partial z_a} \, (\phi \, \psi) \right]^2 \tag{A.10}$$

if $\phi^*\psi^* = \phi\,\psi$ and if $\int dz_e\,dz_h\,d^2r\;|\phi\,\psi|^2 = 1$ [107]. Now, we obtain an effective Schrödinger equation for the motion along the QW axis

$$\left[\sum_{a=e,h} -\frac{\hbar^2}{2m_a}\Delta_{z_a} + V_a^{\mathrm{QW}}(z_a) - E^{(\mathrm{2D})}(Z) + W^{\mathrm{c}}(Z)\right]\psi(z_e,z_h) = E_\psi\,\psi(z_e,z_h)\,. \tag{A.11}$$

If we are within the limit where the QW confinement in terms of the subband level separation is large compared to any other energetic contribution, the quantities $E^{(\mathrm{2D})}(Z)$ and $W^{\mathrm{c}}(Z)$ in equation (A.11) can be treated as perturbations. Then, $\psi(z_e,z_h) = \varphi_e(z_e)\,\varphi_h(z_h)$ separates and the unperturbated subband envelope functions $\varphi_a(z)$ and energies E_a^{QW} $(a = e,h)$ are given by equations (1.3).

The exciton binding energy is defined as the energy difference between the bottom of the electron-hole pair continuum and the lowest excitonic bound state

$$E_{\mathrm{x}}^{\mathrm{b}} = \int dz_e\,dz_h\,|\varphi_e(z_e)|^2\,|\varphi_h(z_h)|^2\left[E_1^{(\mathrm{2D})}(Z) + W_1^{\mathrm{c}}(Z) - W_{n\to\infty}^{\mathrm{c}}(Z)\right]\,. \tag{A.12}$$

The subscript at $E^{(\mathrm{2D})}$ and W^{c} denotes the quantum number of Schrödinger equation (A.5). (Note that $E_{n\to\infty}^{(\mathrm{2D})} = 0$ for all Z.) Any exciton binding energy calculated in the chapters 4 and 6 has been obtained using the fitting functions from Refs. [93, 133] (for $E^{(\mathrm{2D})}(Z)$) and Ref. [133] (for $W^{\mathrm{c}}(Z)$).

In chapter 6, the explicit form of the QW relative wavefunction ϕ is needed. For the sake of simplicity, we do not solve Schrödinger equation (A.5) for each value of Z, but use the reasonably accurate variational wavefunction suggested in Ref. [93] that gives correct results for both limiting cases $Z \to 0$ and $Z \gg a_o$:

$$\phi(r,Z) = \frac{N(\tilde{Z})}{a_o}\exp\left[\lambda(\tilde{Z})\left(\sqrt{\tilde{r}^2+\tilde{Z}^2} - \tilde{Z}\right)\right]\,, \tag{A.13}$$

where $\tilde{r} = r/a_o$, $\tilde{Z} = Z/a_o$, and $\lambda(\tilde{Z}) = 2/(1+2\sqrt{\tilde{Z}}\,)$.

$$N(\tilde{Z}) = \left[\frac{\pi}{\lambda}\left(\frac{1}{2\lambda} + \tilde{Z}\right)\right]^{-1/2} \tag{A.14}$$

is a norm conserving factor.

The exciton binding energy calculated with expression (A.12) is plotted in Figs. A.1 (a), (b), and (c) as a function of the QW width d_{QW} for cadmium concentrations $x = 0.1$, 0.2, and 0.3, respectively (down triangles). As a result of the consideration of the Coulomb correlation along the QW axis, neglected in the previous model, the binding energies of this model are larger than those of the previous one. It should be noted, that these results have not been obtained by an actual perturbation calculation, but with the help of fit formula (A.13) and fit formulae for $E^{\mathrm{2D}}(Z)$ [93, 133] and $W^{\mathrm{c}}(Z)$ [133].

A.3 Fractional-Dimensional-Ansatz

A popular and simple first approach to the QW exciton is the fractional-dimensional model [66, 160, 67, 68, 69, 103, 104]. The idea is to describe the restricted freedom of motion of particles in a QW by a reduced dimensionality between 2D and 3D. An anisotropic solid is treated as an isotropic, fractional-dimensional system, whose dimension is determined by the degree of anisotropy of interactions. The anisotropic interaction in an actual 3D space becomes isotropic in a fractional-dimensional space with lower dimensionality. The mathematical framework for this approach is the Hausdorff measure [66].

The exciton Schrödinger equation in an arbitrary non-integer dimensional space reads [160]

$$\left[-\frac{\hbar^2}{2\mu r^{\alpha-1}}\frac{\partial}{\partial r}\left(r^{\alpha-1}\frac{\partial}{\partial r}\right)+\frac{l^2}{2\mu r^2}-\frac{e^2}{\kappa r}\right]\phi = E\,\phi \tag{A.15}$$

where α $(1 < \alpha < 3)$ is the dimension of the system and l^2 corresponds to the angular momentum operator given by

$$l^2 = -\frac{\hbar^2}{\sin^{\alpha-2}\vartheta}\frac{\partial}{\partial\vartheta}\left(\sin^{\alpha-2}\frac{\partial}{\partial\vartheta}\right)\,. \tag{A.16}$$

Radial distance r $(0 \le r \le \infty)$ and related angle ϑ $(0 \le \vartheta \le \pi)$ measured relative to an axis passing through the origin are two coordinates describing the relative distance vector $\mathbf{r}$ in the αD space. Equation (A.15) is separable into a radial and an angular differential equation by $\phi = R_{nl}(r)\,\theta_l(\vartheta)$. The discrete bound state energies and orbital radii are given by

$$E_n = -\left(n + \frac{\alpha - 3}{2}\right)^{-2} Ry_{\mathrm{x}} \qquad \text{and} \tag{A.17}$$

$$a_n = \left(n + \frac{\alpha - 3}{2}\right)^{2} a_{\mathrm{x}}\,, \tag{A.18}$$

respectively, where $n = 1, 2, 3, ...$ is the principal quantum number, $Ry_{\mathrm{x}} = \hbar^2/(2\mu a_{\mathrm{x}}^2)$ and $a_{\mathrm{x}} = \hbar^2 4\pi\varepsilon\varepsilon_o/(e^2\mu)$ are the bulk exciton Rydberg and Bohr radius, respectively. The $1s$ relative wavefunction reads

$$R_{10}(r) = N(\alpha)\exp\left(-\frac{r}{\left(\frac{\alpha-1}{2}\right)a_{\mathrm{x}}}\right)\,, \tag{A.19}$$

where $N(\alpha)$ is a norm conserving factor. For excited states see Ref. [69].

A simple explicit relation between the QW geometry (width and depth) and the fractional dimension α has been suggested in Ref. [103]

$$\alpha = 3 - \exp\left(-\frac{\tilde{d}_{\mathrm{QW}}}{2a_{\mathrm{x}}}\right)\,, \tag{A.20}$$

where $\tilde{d}_{\mathrm{QW}}$ represents the spatial extension of the exciton motion along the QW axis, taking into account the spreading into the barriers by $\tilde{d}_{\mathrm{QW}} = 2/k_{\mathrm{B}} + d_{\mathrm{QW}}$, where $1/k_{\mathrm{B}}$ is the penetration length of the exciton into the barrier. If the electron and hole spreadings are very different, the more delocalized particle partially restores a 3D character. Consequently, the spreading of the complete exciton into the barriers may be written as $1/k_{\mathrm{B}} = 1/k_e + 1/k_h$, where k_e and k_h are taken from the solutions of the subband equations (1.3).

The resulting exciton binding energies are also plotted in Fig. A.1 (squares). It can be seen, that the fractional-dimensional ansatz yields binding energies which are up to 15% smaller than those obtained with the full separation ansatz. Of course, the latter already provides an upper bound for the true value of the total energy (lower bound for the binding energy) due to the neglect of Coulomb correlation along the QW axis. For comparison, the results of the variational ansatz [140]

$$\phi(r, z_e - z_h) = N\exp\left(-\frac{\sqrt{r^2 + \beta^2(z_e - z_h)^2}}{a}\right)\,, \tag{A.21}$$

(where N is a norm conserving factor, β and a are the variational parameters) are additionally plotted in Fig. A.1 (circles). The strongest deviation of the full separation ansatz from the more advanced variational ansatz (which is also an upper bound) appears for the limiting cases where the subband functions are more delocalized and the Coulomb correlation along the QW axis becomes more and more important.

For the sake of completeness it should be mentioned that there is at least one more sophisticated ansatz [104] to obtain a relation between the system geometry and the fractional dimension α. However, no explicit analytical expression can be given for this relation within this approach, but a variational calculation has to be executed.

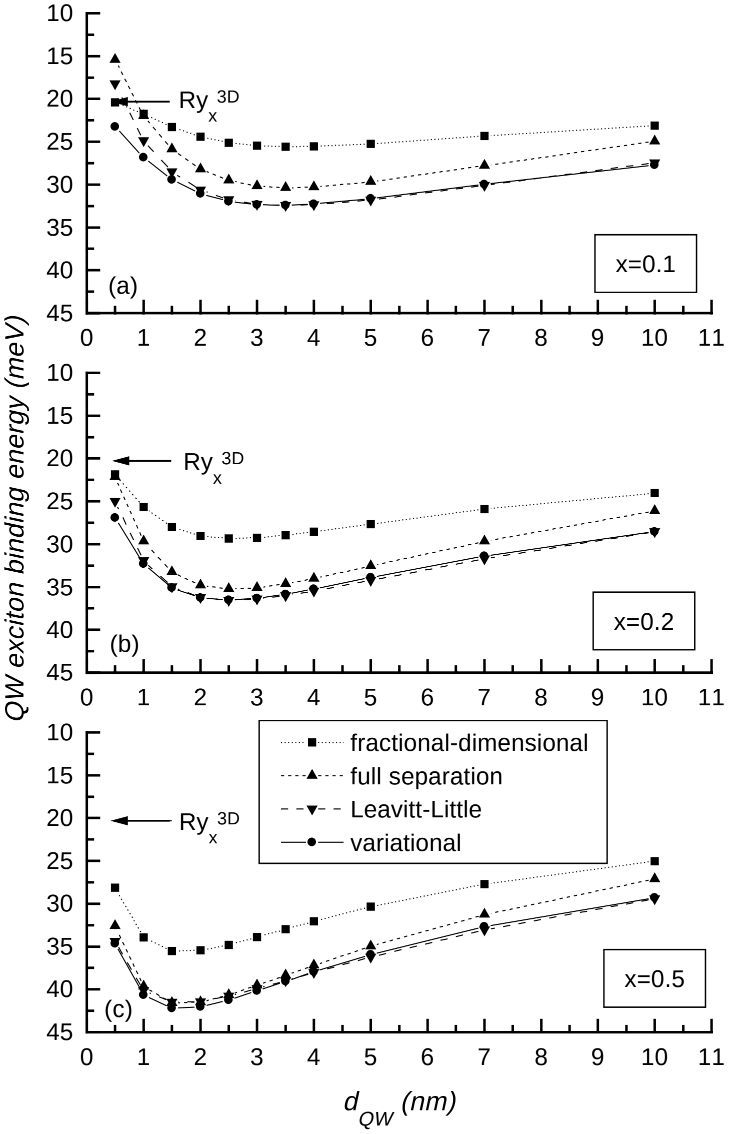

Figure A.1: *Exciton binding energy as a function of the QW thickness for* $Zn_{1-x}Cd_xSe$ */ZnSe QWs with cadmium concentrations (a)* $x = 0.1$, *(b)* $x = 0.2$, *and (c)* $x = 0.5$.

Appendix B

Weight Functions of the Hole-Hole Separation Ansatz

Here, it is outlined how to calculate the weight function $f_a(s)$ from the biexciton relative wave-function in case of the hole-hole separation model. Using exponential functions for the exciton relative wave-function ϕ_{x} in ansatz (2.14), we obtain for the adiabatic biexciton relative wave-function

$$\phi(\mathbf{r}_1, \mathbf{r}_2, \mathbf{h}) = \frac{2}{\pi\,\sqrt{2(1+S^2)}}\,\gamma^2\left(\mathrm{e}^{-\gamma r_1}\,\mathrm{e}^{-\gamma r_2} + \mathrm{e}^{-\gamma|\mathbf{r}_1-\mathbf{h}|}\,\mathrm{e}^{-\gamma|\mathbf{r}_2+\mathbf{h}|}\right)F(h)\,, \tag{B.1}$$

where

$$\begin{aligned} \mathbf{r}_1 &= \mathbf{r}_{e1} - \mathbf{r}_{h1}, && \text{(B.2)}\\ \mathbf{r}_2 &= \mathbf{r}_{e2} - \mathbf{r}_{h2}, && \text{(B.3)}\\ \mathbf{h} &= \mathbf{r}_{h2} - \mathbf{r}_{h1}\,, && \text{(B.4)} \end{aligned}$$

is the chosen set of relative coordinates and $\mathrm{F}(h)$ is the solution of the 2D inter-exciton Schrödinger equation (2.15). Inserting equation (B.1) into equation (2.3) yields

$$\begin{aligned} f_a(s) \;=\;& \frac{4\,\gamma^4}{\pi^2\,2(1+S^2)}\int d\,\mathbf{r}_1\,d\,\mathbf{r}_2\,d\,\mathbf{h}\;\delta(\mathbf{r}_a-\mathbf{R}-\mathbf{s})\,\times\\ &\times\left(\mathrm{e}^{-2\gamma r_1}\,\mathrm{e}^{-2\gamma r_2} + \mathrm{e}^{-2\gamma|\mathbf{r}_1-\mathbf{h}|}\,\mathrm{e}^{-2\gamma|\mathbf{r}_2+\mathbf{h}|} + \right.\\ &\quad\left. 2\,\mathrm{e}^{-\gamma r_1}\,\mathrm{e}^{-\gamma r_2}\,\mathrm{e}^{-\gamma|\mathbf{r}_1-\mathbf{h}|}\,\mathrm{e}^{-\gamma|\mathbf{r}_2+\mathbf{h}|}\right)\mathrm{F}^2(h)\\ &(a = e1, e2, h1, h2)\,, \end{aligned} \tag{B.5}$$

so that we finally receive for an electron

$$f_{ei}(s) = \mathrm{N} \int_0^\infty dh\, h\, \mathrm{F}^2(h) \left[\mathrm{I_z}(s,h) + \mathrm{J_{zz}}(s,h)\mathrm{G}(h)\right] \qquad (i = 1,2)\,, \tag{B.6}$$

with

$$\begin{aligned}
\mathrm{I_z}(s,h) &= \int_0^{2\pi} d\alpha_h\, \mathrm{e}^{-2\gamma\sqrt{s^2+(h/2)^2+sh\cos(\alpha_h)}}\,, && \text{(B.7)}\\
\mathrm{J_{zz}}(s,h) &= \int_0^{2\pi} d\alpha_h\, \mathrm{e}^{-\gamma\sqrt{s^2+(h/2)^2+sh\cos(\alpha_h)}} \times \\
&\quad \times \mathrm{e}^{-\gamma\sqrt{s^2+(h/2)^2-sh\cos(\alpha_h)}}\,, && \text{(B.8)}\\
\mathrm{G}(h) &= \frac{2}{\pi}\gamma^2 \int_0^\infty dr\, r\mathrm{e}^{-\gamma r} \int_0^{2\pi} d\alpha_r\, \mathrm{e}^{-\gamma\sqrt{r^2+h^2-2rh\cos(\alpha_r)}}\,, && \text{(B.9)}
\end{aligned}$$

and for a hole

$$f_{hi}(s) = \mathrm{N}\, \mathrm{F}(2s) \left[1 + \mathrm{I}^2_{\mathrm{zz}}(s)\right] \qquad (i = 1,2)\,, \tag{B.10}$$

with

$$\mathrm{I_{zz}}(s) = \frac{2}{\pi}\gamma^2 \int_0^\infty dr\, r\mathrm{e}^{-\gamma r} \int_0^{2\pi} d\alpha_r\, \mathrm{e}^{-\gamma\sqrt{r^2+4s^2+4rs\cos(\alpha_r)}}\,. \tag{B.11}$$

N is a normalization constant.

Bibliography

[1] Sample: P. Waltereit, O. Brandt, and K. H. Ploog, *Paul-Drude-Institut für Festkörperelektronik*, Berlin.
Meassurement: B. Rau, J. Puls, and F. Henneberger, *Humboldt-Universität zu Berlin.*

[2] ToSCA: *TwO-dimensional SemiConductor Analysis package*, Weierstraß-Institut für Angewandte Analysis und Stochastik, Berlin.

[3] http://www.nd.edu/˜gsnider/.

[4] Nitride news. *MRS Internet Journal Nitride Semiconductor Research.* See also http://www.mesh.ne.jp/nichia/index-e.htm.

[5] I. Akasaki and H. Amano. *J. Electrochem. Soc.* **141**, page 2266, 1994.

[6] O. Ambacher, J. Smart, J. R. Shealy, N. G. Weimann, K. Chu, M. Murphy, R. Dimitrov, L. Wittmer, M. Stutzmann, W. Rieger, and J. Hilsenbeck. *J. Appl. Phys.* **85**, page 3222, 1999.

[7] T. Araki, T. Minami, and Y. Nanishi. *phys. stat. sol. (a)* **176**, page 487, 1999.

[8] D. J. As and K. Lischka. *phys. stat. sol. (a)* **176**, page 475, 1999.

[9] L. Banyaj, I. Galbraith, C. Ell, and H. Haug. In R. Del Sole, A. D'Andrea, and A. Lapiccirella, editors, *Excitons in Confined Systems.* Springer-Verlag, Berlin, 1988.

[10] S. D. Baranovskii, U. Doerr, P. Thomas, A. Naumov, and W. Gebhardt. *Phys. Rev. B* **48**, page 17149, 1993.

[11] S. D. Baranovskii and A. L. Efros. *Fiz. Tekh. Poluprovodh.* **12**, page 2233, 1978.

[12] G. Bastard, E. E. Mendez, L. L. Chang, and L. Esaki. *Phys. Rev. B* **26**, page 1974, 1982.

[13] L. Bellaiche, T. Mattila, L.-W. Wang, S.-H. Wei, and A. Zunger. *Appl. Phys. Lett.* **74**, page 1842, 1999.

[14] L. Bellaiche and A. Zunger. *Phys. Rev. B* **57**, page 4425, 1998.

[15] E. Berkowicz, D. Gershoni, G. Bahir, E. Lakin, D. Shilo, E. Zolotoyabko, A. C. Abare, S. P. DenBaars, and L. A. Coldren. *Phys. Rev. B* **61**, page 10994, 2000.

[16] V. M. Bermudez. *J. Appl. Phys.* **80**, page 1190, 1996.

[17] F. Bernardini, V. Fiorentini, and D. Vanderbilt. *Phys. Rev. B* **56**, page R10024, 1997.

[18] P. Bogusławski, K. Rapcewicz, and J. J. Bernholc. *Phys. Rev. B* **61**, page 10820, 2000.

[19] M. Born and J. R. Oppenheimer. *Ann. Phys.* **84** (Leipzig), page 457, 1927.

[20] R. W. Brander and R. P. Sutton. *J. Phys. D: Appl. Phys.* **2**, page 309, 1969.

[21] O. Brandt, J. R. Müllhäuser, B. Yang, H. Yang, and K. H. Ploog. *Physica E* **2**, page 532, 1998.

[22] D. A. Broido and L. J. Sham. *Phys. Rev. B* **34**, page 3917, 1986.

[23] A. D. Bykhovski, V. V. Kaminski, M. S. Shur, Q. C. Chen, and M. A. Khan. *Appl. Phys. Lett.* **68**, page 818, 1996.

[24] L. Calcagnile, D. Cannoletta, R. Cingolani, M. Lomascolo, M. Di Dio, L. Vanzetti, L. Sorba, and A. Franciosi. *Phys. Rev. B* **55**, page R13413, 1997.

[25] L. Calcagnile, D. Greco, G. Coli', R. Cingolani, M. Lomascolo, M. Di Dio, L. Sorba, and A. Franciosi. *Superlatt. Microstruc.* **21**, page 119, 1997.

[26] A. N. Cartwright, P. M. Sweeney, T. Prunty, D. P. Bour, and M. Kneissl. *MRS Internet J. Nitride Semicond.* **4**, page 12, 1999.

[27] H. Castella and J. W. Wilkins. *Phys. Rev. B* **58**, page 16186, 1998.

[28] H. Chen, A. R. Smith, R. M. Feenstra, D. W. Greve, and J. E. Northrup. *MRS Internet J. Nitride Semicond. S1, G9.5*, 1999.

[29] S. Chichibu, T. Azuhata, T. Sota, and S. Nakamura. *Appl. Phys. Lett.* **69**, page 4188, 1996.

[30] S. Chichibu, T. Azuhata, T. Sota, and S. Nakamura. *Appl. Phys. Lett.* **70**, page 2822, 1997.

[31] S. Chichibu, D. A. Cohen, M. P. Mack, A. C. Abare, P. Kozodoy, M. Minsky, S. B. Fleischer, S. Keller, J. E. Bowers, U. K. Mishra, L. A. Coldren, D. R. Clarke, and S. P. DenBaars. *Appl. Phys. Lett.* **73**, page 496, 1998.

[32] S. Chichibu, K. Wada, and S. Nakamura. *Appl. Phys. Lett.* **71**, page 2346, 1997.

[33] S. F. Chichibu, A. C. Abare, M. S. Minsky, S. Keller, S. B. Fleischer, J. E. Bowers, E. Hu, U. K. Mishra, L. A. Coldren, and S. P. DenBaars. *Appl. Phys. Lett.* **73**, page 2006, 1998.

[34] S. F. Chichibu, H. Marchand, M. S. Minsky, S. Keller, P. T. Fini, J. P. Ibbertson, S. B. Fleischer, J. S. Speck, J. E. Bowers, E. Hu, U. K. Mishra, S. P. DenBaars, T. Deguchi, T. Sota, and S. Nakamura. *Appl. Phys. Lett.* **74**, page 1460, 1999.

[35] S. F. Chichibu, T. Sota, K. Wada, S. P. DenBaars, and S. Nakamura. *MRS Internet J. Nitride Semicond.* 4S1, G2.7, 1999.

[36] Y.-H. Cho, G. H. Gainer, A. J. Fischer, J. J. Song, S. Keller, U. K. Mishra, and S. P. DenBaars. *Appl. Phys. Lett.* **73**, page 1370, 1998.

[37] Y.-H. Cho, J. J. Song, S. Keller, M. S. Minsky, E. Hu, U. K. Mishra, and S. P. DenBaars. *Appl. Phys. Lett.* **73**, page 1128, 1998.

[38] Y.-H. Cho, J. J. Song, S. Keller, U. K. Mishra, and S. P. DenBaars. *Appl. Phys. Lett.* **73**, page 3181, 1998.

[39] R. Cingolani, A. Botchkarev, H. Tang, H. Moroç, G. Traetta, G. Coli, M. Lomascolo, A. Di Carlo, F. Della Sala, and P. Lugli. *Phys. Rev. B* **61**, page 2711, 2000.

[40] R. D. Cunningham, R. W. Brander, N. D. Kbee, and D. K. Wickenden. *J. Lumin.* **5**, page 21, 1972.

[41] J. Dalfors, J. P. Bergman, P. O. Holtz, B. E. Sernelius, B. Monemar, H. Amano, and I. Akasaki. *Appl. Phys. Lett.* **74**, page 3299, 1999.

[42] R. F. Davis. *Proc. IEEE* **79**, page 702, 1991.

[43] M. D. Dawson and G. Duggan. *Phys. Rev. B* **47**, page 12598, 1993.

[44] C. G. Van de Walle and J. Neugebauer. *Appl. Phys. Lett.* **70**, page 2577, 1997.

[45] S. S. Dhesi, C. B. Stagarescu, K. E. Smith, D. Doppalapudi, R. Singh, and T. Moustakas. *Phys. Rev. B* **56**, page 10271, 1997.

[46] J. Ding, M. Hagerott, T. Ishibara, H. Jeon, and A. V. Nurmikko. *Phys. Rev. B* **47**, page 10528, 1993.

[47] J. Ding, H. Jeon, T. Ishibara, M. Hagerott, A. V. Nurmikko, H. Luo, N. Samarth, and J. Furdyna. *Phys. Rev. Lett.* **69**, page 1707, 1992.

[48] D. Doppalapudi, S. N. Basu, K. F. Ludwig, Jr. and T. D. Moustakas. *J. Appl. Phys.* **84**, page 1389, 1998.

[49] R. M. Dreizler and E. K. U. Gross. *Density Functional Theory.* Springer-Verlag, Berlin, Heidelberg, 1990.

[50] N. Duxbury, U. Bangert, P. Dawson, E. J. Trush, W. Van der Stricht, K. Jacobs, and I. Moerman. *Appl. Phys. Lett.* **76**, page 1600, 2000.

[51] J. H. Edgar, editor. *Properties of Group III Nitrides.* INSPEC, IEE, London, 1994.

[52] U. Ekenberg and M. Altarelli. *Phys. Rev. B* **35**, page 7585, 1987.

[53] H. Eschrig. *The Fundamentals of Density Functional Theory, Teubner-Texte zur Physik Band 32.* Teubner Verlagsgesellschaft, Stuttgart, Leipzig, 1996.

[54] V. Fiorentini, F. Bernardini, F. Della Sala, A. Di Carlo, and P. Lugli. *Phys. Rev. B* **60**, page 8849, 1999.

[55] P. Fischer, J. Christen, M. Zacharias, V. Schwegler, C. Kirchner, and M. Kamp. *Appl. Phys. Lett.* **75**, page 3440, 1999.

[56] S. Flügge. *Rechenmethoden der Quantentheorie.* Springer-Verlag, 1993.

[57] J.-M. Gerard and J.-Y. Marzi. *Phys. Rev. B* **45**, page 6313, 1992.

[58] O. Gfrörer, C. Gemmer, J. Off, J. S. Im, F. Scholz, and A. Hangleiter. *phys. stat. sol. (b)* **216**, page 405, 1999.

[59] S. Glutsch, D. S. Chemla, and F. Bechstedt. *Phys. Rev. B* **54**, page 11592, 1996.

[60] C. Gourdon, I. V. Mashkov, P. Lavallard, and R. Planel. *Phys. Rev. B* **57**, page 3955, 1998.

[61] L. R. Greene, K. K. Bajaj, and D. E. Phelps. *Phys. Rev. B* **29**, page 1807, 1984.

[62] H. E. Gumlich, D. Theis, and D. Tschierse. *Numerical Data and Functional Relationship in Science and Technology,* Landolt-Börnstein, New Series, Group III, Vol. 17, Pt. a. Springer-Verlag, Berlin, 1982.

[63] M. Haase, J. Qui, J. DePuydt, and H. Cheng. *Appl. Phys. Lett.* **59**, page 1272, 1991.

[64] A. Hangleiter, J. S. Im, H. Kollmer, S. Heppel, J. Off, and F. Scholz. *MRS Internet J. Nitride Semicond.* **3**, page 15, 1998.

[65] A. Hangleiter, J. S. Im, J. Off, and F. Scholz. *phys. stat. sol. (b)* **216**, page 427, 1999.

[66] F. Hausdorff. *Ann. Math.* **79**, page 157, 1918.

[67] X. F. He. *Solid State Comm.* **75**, page 111, 1990.

[68] X. F. He. *Phys. Rev. B* **42**, page 11751, 1990.

[69] X. F. He. *Phys. Rev. B* **43**, page 2063, 1991.

[70] E. S. Hellmann. *MRS Internet J. Nitride Semicond.* **3**, page 11, 1998.

[71] J. Holst, A. Hoffmann, I. Broser, D. Rudloff, F. Bertram, T. Riemann, J. Christen, T. Frey, D. J. As, D. Schikora, and K. Lischka. *phys. stat. sol. (b)* **216**, page 471, 1999.

[72] I hsiu Ho and G. B. Stringfellow. *Appl. Phys. Lett.* **69**, page 2701, 1996.

[73] Y. Z. Hu, M. Lindberg, and S. W. Koch. *Phys. Rev. B* **42**, page 1713, 1990.

[74] J. S. Im, H. Kollmer, J. Off, A. Sohmer, F. Scholz, and A. Hangleiter. *Phys. Rev. B* **57**, page R9435, 1998.

[75] U. Jahn, S. H. Kwok, M. Ramsteiner, R. Hey, H. T. Grahn, and E. Runge. *Phys. Rev. B* **54**, page 2733, 1996.

[76] H. Jiang, M. Minsky, S. Keller, E. Hu, J. Singh, and S. P. DenBaars. *IEEE J. Quantum Electron.* **35**, page 1483, 1999.

[77] H.-Chr. Kaiser and J. Rehberg. *Nonlinear Analysis* **41**, page 33, 2000.

[78] Y. C. Kao, F. G. Celii, and H. Y. Liu. *J. Vac. Sci. Technol. B* **11***(3)*, page 1023, 1993.

[79] I. A. Karp and S. A. Moskalenko. *Fiz. Techn. Poluprov.* **8**, page 285, 1974.

[80] K. Kim, W. R. L. Lambrecht, B. Segall, and M. van Schilfgaarde. *Phys. Rev. B* **56**, page 7363, 1997.

[81] C. Kisielowski, Z. Liliental-Weber, and S. Nakamura. *Jpn. J. Appl. Phys.* **36**, page 6932, 1997.

[82] H.-C. Ko, D.-C. Park, Y. Kawakami, S. Fujita, S. Fujita, and Y.-S. Kim. *Appl. Phys. Lett.* **73**, page 1388, 1998.

[83] B. Koiller and R. B. Capaz. *Phys. Rev. B* **60**, page 1787, 1999.

[84] F. Kreller, M. Lowisch, J. Puls, and F. Henneberger. *Phys. Rev. Lett.* **75**, page 2420, 1995.

[85] F. Kreller, J. Puls, and F. Henneberger. *Appl. Phys. Lett.* **69** *(16)*, page 2406, 1996.

[86] F. Kreller, H.-J. Wünsche, J. Puls, and F. Henneberger. *J. Cryst. Growth* **184/185**, page 614, 1997.

[87] G. Kuang, W. Gebhardt, E. Griebl, K. Sube, M. Kastner, M. Wörz, and T. Reisinger. *Appl. Phys. Lett.* **70**, page 2717, 1997.

[88] H. Lakner, G. Brockt, C. Mendorf, A. Radefeld, F. Scholz, V. Härle, J. Off, and A. Sohmer. *J. Electron. Mater.* **26**, page 1103, 1997.

[89] W. R. L. Lambrecht. *Solid-State Electron.* **41**, page 195, 1997.

[90] L. D. Landau and E. M. Lifschitz. *Lehrbuch der Theoretischen Physik*, volume III, page 45. Springer-Verlag.

[91] Landoldt-Börnstein. *New Series III/17a Semiconductors: Physics of Group IV Elements and III-V Compounds.* Springer-Verlag, 1982.

[92] R. Langer, J. Simon, V. Ortiz, N. T. Pelekanos, A. Barski, R. André, and M. Godlewski. *Appl. Phys. Lett.* **74**, page 3827, 1999.

[93] R. P. Leavitt and J. W. Little. *Phys. Rev. B* **42**, page 11774, 1990.

[94] P. Lefebvre, J. Allègre, B. Gil, A. Kavokine, H. Mathieu, W. Kim, A. Salvador, A. Botchkarev, and Hadis Morkoç. *Phys. Rev. B* **57**, page R9447, 1998.

[95] M. Leroux, N. Grandjean, J. Massies, B. Gil, P. Lefebvre, and P. Bigenwald. *Phys. Rev. B* **60**, page 1496, 1999.

[96] B. Lita, R. S. Goldman, J. D. Phillips, and P. K. Bhattacharya. *Appl. Phys. Lett.* **75**, page 2797, 1999.

[97] H. J. Lozykowski and V. K. Shastri. *J. Appl. Phys.* **69**, page 3235, 1991.

[98] J. A. Majewski, M. Städele, and P. Vogl. In T. Moustakas, B. Monemar, I. Akasaki, and F. Ponce, editors, *MRS Symposia Proceedings No. 449: III-V Nitrides*, page 887, Pittsburgh, 1997. Material Research Society.

[99] C. Manz, M. Kunzer, H. Obloh, A. Ramakrishnan, and U. Kaufmann. *Appl. Phys. Lett.* **74**, page 3993, 1999.

[100] G. Martin, A. Botchkarev, A. Rockett, and H. Morkoç. *Appl. Phys. Lett.* **68**, page 2541, 1996.

[101] R. W. Martin, P. G. Middleton, K. P. O'Donnell, and W. van der Stricht. *Appl. Phys. Lett.* **74**, page 263, 1999.

[102] J. Massies, F. Turco, A. Saletes, and J. P. Contour. *J. Cryst. Growth* **80**, page 307, 1987.

[103] H. Mathieu, P. Lefebvre, and P. Christol. *Phys. Rev. B* **46**, page 4092, 1992.

[104] A. Matos-Abiague, L. E. Oliveira, and M. de Dios-Leyva. *Phys. Rev. B* **58**, page 4072, 1998.

[105] M. D. McCluskey, C. G. Van de Walle, C. P. Master, L. T. Romano, and N. M. Johnson. *Appl. Phys. Lett.* **72**, page 2725, 1998.

[106] M. D. McCluskey, L. T. Romano, B. S. Krusor, D. P. Bour, N. M. Johnson, and S. Brennan. *Appl. Phys. Lett.* **72**, page 1730, 1998.

[107] A. Messiah. *Quantenmechanik 2*, page 270. Walter de Gruyter, Berlin, 3 edition, 1990.

[108] M. S. Minsky, S. Chichibu, S. B. Fleischer, A. C. Abare, J. E. Bowers, E. L. Hu, S. Keller, U. K. Mishra, and S. P. DenBaars. *Jpn. J. Appl. Phys.* **37**, page L1362, 1998.

[109] M. S. Minsky, S. B. Fleischer, A. C. Abare, J. E. Bowers, E. L. Hu, S. Keller, and S. P. DenBaars. *Appl. Phys. Lett.* **72**, page 1066, 1998.

[110] B. Monemar, J. P. Bergman, J. Dalfors, G. Pozina, B. E. Sernelius, P. O. Holtz, H. Amano, and I. Akasaki. *MRS Internet J. Nitride Semicond.* **4**, page 16, 1999.

[111] O. Moriwaki, T. Someya, K. Tachibana, S. Ishida, and Y. Arakawa. *Appl. Phys. Lett.* **76**, page 2361, 2000.

[112] H. Morkoç and S. N. Mohammad. *Science Vol.* **267**, page 51, 1995.

[113] K. Muraki, S. Fukatsu, Y. Shiraki, and R. Ito. *Appl. Phys. Lett.* **61**, page 557, 1992.

[114] K. Muraki, S. Fukatsu, Y. Shiraki, and R. Ito. *J. Cryst. Growth* **127**, page 546, 1993.

[115] J. Nagle, J. P. Landesman, M. Larive, C. Mottet, and P. Bois. *J. Cryst. Growth* **127**, page 550, 1993.

[116] S. Nakamura. *J. Vac. Sci. Technol. A* **14**, page 705, 1994.

[117] S. Nakamura and G. Fasol. *The Blue Laser Diode.* Springer-Verlag, Berlin, 1997.

[118] Y. Narukawa, Y. Kawakami, S. Fujita, and S. Nakamura. *Phys. Rev. B* **59**, page 10283, 1999.

[119] Y. Narukawa, Y. Kawakami, M. Funato, S. Fujita, S. Fujita, and S. Nakamura. *Appl. Phys. Lett.* **70**, page 981, 1997.

[120] Y. Narukawa, K. Sawada, Y. Kawakami, S. Fujita, S. Fujita, and S. Nakamura. *J. Cryst. Growth* **189/190**, page 606, 1998.

[121] H. Nickolaus, H.-J. Wünsche, and F. Henneberger. *Phys. Rev. Lett.* **81**, page 2586, 1998.

[122] J. E. Northrup, L. T. Romano, and J. Neugebauer. *Appl. Phys. Lett.* **74**, page 2319, 1999.

[123] A. V. Nurmikko and R. L. Gunshor. *IEEE J. Quantum Electron.* **30**, page 619, 1994.

[124] K. P. O'Donnell, T. Breitkopf, H. Kalt, W. van der Stricht, I. Moerman, P. Demeester, and P. G. Middleton. *Appl. Phys. Lett.* **70**, page 1843, 1997.

[125] K. P. O'Donnell, R. W. Martin, and P. G. Middleton. *Phys. Rev. Lett.* **82**, page 237, 1999.

[126] K. Osamura, S. Naka, and Y. Murakami. *J. Appl. Phys.* **46**, page 3432, 1975.

[127] G. Otter and R. Honecker. *Atome – Moleküle – Kerne*, volume II. Teubner-Verlag, 1996.

[128] J. I. Pankove, S. Bloom, and G. Harbeke. *RCA Rev.* **36**, page 163, 1975.

[129] C. A. Parker, J. C. Roberts, S. M. Bedair, M. J. Reed, S. X. Liu, N. A. El-Masry, and L. H. Robins. *Appl. Phys. Lett.* **75**, page 2566, 1999.

[130] R. G. Parr and W. Yang. *Density Functional Theory of Atoms and Molecules.* Oxford University Press, New York, 1989.

[131] L.-H. Peng, C.-W. Chuang, and L.-H. Lou. *Appl. Phys. Lett.* **74**, page 795, 1999.

[132] P. Perlin, C. Kisielowski, V. Iota, B. A. Weinstein, L. Mattos, N. A. Shapiro, J. Kruger, E. R. Weber, and J. Yang. *Appl. Phys. Lett.* **73**, page 2778, 1998.

[133] P. Peyla, R. Romestain, Y. Merle d'Aubign, G. Fishman, A. Wasiela, and H. Mariette. *Phys. Rev. B* **52**, page 12026, 1995.

[134] L. Pfeiffer, K. W. West, H. L. Stormer, and K. W. Baldwin. *Appl. Phys. Lett.* **55**, page 1888, 1989.

[135] F. A. Ponce. Structural defects and material performence of the iii-v-nitrides. In B. Gil, editor, *Group III Nitride Semiconductor Compounds: Physics and Applications*, page 128. Oxford Science Publications, New York, 1998.

[136] F. A. Ponce and D. P. Bour. *Nature* **386**, page 351, 1997.

[137] W. H. Press, B. P. Flannery, S. A. Teukolsky, and W. T. Vetterling. *Numerical Recipes*, page 254. Cambridge University Press, 1989.

[138] W. H. Press, B. P. Flannery, S. A. Teukolsky, and W. T. Vetterling. *Numerical Recipes*, page 377. Cambridge University Press, 1989.

[139] Rodney Price, Xuejun Zhu, S. DasSarma, and P. M. Platzman. *Phys. Rev. B* **51**, page 2017, 1995.

[140] J. Puls. *Humboldt-Universität zu Berlin.*

[141] J. Puls, H.-J. Wünsche, and F. Henneberger. *Chem. Phys.* **210**, page 235, 1996.

[142] P. Riblet, H. Hirayama, A. Kinoshita, A. Hirata, T. Sugano, and Y. Aoyagi. *Appl. Phys. Lett.* **75**, page 2241, 1999.

[143] C. Riva, K. Varga, V. A. Schweigert, and F. M. Peeters. *phys. stat. sol. (b)* **210**, page 689, 1998.

[144] A. Rizzi and H. Lüth. *Il Nuovo Cimento D* **20**, page 1039, 1998.

[145] L. T. Romano, B. S. Krusor, M. D. McCluskey, D. P. Bour, and K. Nauka. *Appl. Phys. Lett.* **73**, page 1757, 1998.

[146] G. A. Sai-Halasz, L. L. Chang, J.-M. Welter, C.-A. Chang, and L. Esaki. *Solid State Commun.* **27**, page 935, 1978.

[147] T. Saito and Y. Arakawa. *Phys. Rev. B* **60**, page 1701, 1999.

[148] T. Sajoto, M. Santos, Heremans J. J, and K. W. Baldwin. *Appl. Phys. Lett.* **54**, page 840, 1989.

[149] F. Della Sala, A. Di Carlo, , P. Lugli, F. Bernardini, V. Fiorentini, R. Scholz, and J.-M. Jancu. *Appl. Phys. Lett.* **74**, page 2002, 1999.

[150] J. L. Sánchez-Rojas, J. A. Garrido, and E. Mu noz. *Phys. Rev. B* **61**, page 2773, 2000.

[151] T. J. Schmidt, Y.-H. Cho, G. H. Grainer, J. J. Song, S. Keller, U. K. Mishra, and S. P. DenBaars. *Appl. Phys. Lett.* **73**, page 1892, 1998.

[152] V. A. Schweigert and F. M. Peeters. *Finite-difference multi-particle Schrödinger equation: binding energy of a biexciton.* (unpublished), April 1996.

[153] W. Shan, B. D. Little, J. J. Song, Z. C. Feng, M. Schurman, and R. A. Stall. *Appl. Phys. Lett.* **69**, page 3315, 1996.

[154] W. Shan, W. Walukiewicz, E. E. Haller, B. D. Little, J. J. Song, M. D. McCluskey, N. M. Johnson, Z. C. Feng, M. Schurman, and R. A. Stall. *J. Appl. Phys.* **84**, page 4452, 1998.

[155] K. Shimada, T. Sota, and K. Suzuki. *J. Appl. Phys.* **84**, page 4951, 1998.

[156] J. Simon, R. Langer, A. Barski, and N. T. Pelekanos. *Phys. Rev. B* **61**, page 7211, 2000.

[157] J. Singh, D. Birkedal, V. G. Lyssenko, and J. M. Hvam. *Phys. Rev. B* **53**, page 15909, 1996.

[158] H. Sixl, H. Schenk, and N. Yu. *Phys. Bl.* **54**, page 225, 1998.

[159] G. L. Snider, I.-H. Tan, and E. L. Hu. *J. Appl. Phys.* **68**, page 2849, 1990.

[160] F. H. Stillinger. *J. Math. Phys.* **18**, page 1224, 1977.

[161] S. Strite and H. Morkoç. *J. Vac. Sci. Technol. B* **10**, page 1237, 1992.

[162] T. Sugahara, M. Hao, T. Wang, D. Nakagawa, Y. Naoi, K. Nishino, and S. Sakai. *Jpn. J. Appl. Phys.* **37**, page L1195, 1998.

[163] M. Suzuki, T. Uenoyama, and A. Yanase. *Phys. Rev. B* **52**, page 8132, 1995.

[164] S. M. Sze. *Physics of Semiconductor Devices*, chapter 7.2.2, page 372f. John Wiley & Sons, USA, 2 edition, 1981.

[165] T. Takeuchi, S. Sota, M. Katsuragawa, M. Komori, H. Takeuchi, H. Amano, and I. Akasaki. *Jpn. J. Appl. Phys.* **36**, page L382, 1997.

[166] T. Takeuchi, H. Takeuchi, S. Sota, H. Sakai, H. Amano, and I. Asaki. *Jpn. J. Appl. Phys.* **36**, page L177, 1997.

[167] I.-H. Tan, G. L. Snider, L. D. Chang, and E. L. Hu. *J. Appl. Phys.* **68**, page 4071, 1990.

[168] K. L. Teo, J. S. Colton, P. Y. Yu, E. R. Weber, M. F. Li, W. Liu, K. Uchida, H. Tokunaga, N. Akutsu, and K. Matsumoto. *Appl. Phys. Lett.* **73**, page 1697, 1998.

[169] S. Tnaiguchi, T. Hino, S. Itho, K. Nakano, N. Nakayama, A. Ishibashi, and M. Ikeda. *Electron. Lett.* **32**, page 552, 1996.

[170] S. B. Trickey, editor. *Density Functional Theory of Many-Fermion Systems, Vol. 21 of Advances in Quantum Chemistry*, San Diego, 1990. Academic Press Inc.

[171] A. Vertikov, A. V. Nurmikko, K. Doverspike, G. Bulman, and J. Edmond. *Appl. Phys. Lett.* **73**, page 493, 1998.

[172] T. Wang, D. Nakagawa, M. Lachab, T. Sugahara, and S. Sakai. *Appl. Phys. Lett.* **74**, page 3128, 1999.

[173] T. Wang, D. Nakagawa, J. Wang, T. Sugahara, and S. Sakai. *Appl. Phys. Lett.* **73**, page 3571, 1998.

[174] S.-H. Wei and A. Zunger. *Appl. Phys. Lett.* **72**, page 2011, 1998.

[175] C. Wetzel, T. Takeuchi, S. Yamaguchi, H. Katoh, H. Amano, and I. Asaki. *Appl. Phys. Lett.* **73**, page 1994, 1998.

[176] N. Wieser, O. Ambacher, H.-P. Felsl, L. Görgens, and M. Stutzmann. *Appl. Phys. Lett.* **74**, page 3981, 1999.

[177] M. D. Williams, T. H. Chiu, and F. G. Storz. *J. Vac. Sci. Technol. B* **13***(2)*, page 692, 1995.

[178] A. F. Wright. *J. Appl. Phys.* **82**, page 2833, 1997.

[179] A. F. Wright and J. S. Nelson. *Appl. Phys. Lett.* **66**, page 3051, 1995.

[180] X. H. Wu, C. R. Elsass, A. Abare, M. Mack, S. Keller, P. M. Petroff, S. P. DenBaars, J. S. Speck, and S. J. Rosner. *Appl. Phys. Lett.* **72**, page 692, 1998.

[181] H.-J. Wünsche. *phys. stat. sol. (b)* **96**, page 379, 1979.

[182] H.-J. Wünsche and K Henneberger. *phys. stat. sol. (b)* **91**, page 331, 1979.

[183] H.-J. Wünsche, S. Renisch, and F. Henneberger. In W. Chow and M. Osinski, editors, *SPIE-Proceedings*, volume 2994, page 102, 1997.

[184] F. Yang, M. Wilkinson, E. J. Austin, and K. P. O'Donnell. *Phys. Rev. Lett.* **70**, page 323, 1993.

[185] Y. C. Yeo, T. C. Chong, and M. F. Li. *J. Appl. Phys.* **83**, page 1429, 1998.

[186] F. C. Zhang and S. DasSarma. *Phys. Rev. B* **33**, page 2903, 1986.

[187] Jia-Lin Zhu, Xi Chen, and Jia-Jiong Xiong. *J. Phys. Condens. Matter* **3**, page 9559, 1991.

[188] R. Zimmermann and E. Runge. *J. Luminescence* **60** *&* **61**, page 320, 1994.

[189] R. Zimmermann, E. Runge, and F. Große. In M. Scheffler and R. Zimmermann, editors, *Proceedings of the 23rd ICPS 1996*, volume 3, page 1935, Berlin, 1996.

Danksagung

Ganz besonders herzlich bedanken möchte ich mich bei Ede Wünsche für viel Geduld, Engagement und Inspiration bei der Betreuung des Autors dieser Arbeit und für Großzügigkeit hinsichtlich der Teilnahme an Konferenzen.

Herzlicher Dank für freundliche Unterstützung, Diskussionsbereitschaft und fruchtbare Zusammenarbeit ergeht an folgende Mitarbeiter und Freunde:
Oliver Brandt,
Fritz Henneberger,
Sabine Czaja,
Joachim Puls,
Timur Flissikowski,
Andreas Hundt,
Sven Schwertfeger,
Martin Lowisch,
Michael Rabe,
Philipp Kratzert,
Frank Kreller,
Holger Nickolaus,
Björn Rau,
Diethard Wruck,
Ingo Dudeck,
Patrick Waltereit,
Andreas Thamm,
Roland Zimmermann,
Erich Runge,
Axel Esser,
Clara Riva,
V. A. Schweigert,
F. M. Peeters,
Angela Rizzi,
Roberta Lanthier,
Michaela Haberkorn,
und
Renate.

Lebenslauf

NAME	Oliver Maria Mayrock
ADRESSE	Raumerstraße 41, D-10437 Berlin
TELEFON	++49 30 4479938 (privat) ++49 30 2093-7649 (Universität)
EMAIL	oliver.mayrock@physik.hu-berlin.de
GEBURTSDATUM	2.9.70
GEBURTSORT	Regensburg
FAMILIENSTAND	ledig

Akademischer Werdegang

08/97 – 08/00	Promotion in Theoretischer Physik (Arbeitsgruppe Photonik, Humboldt-Universität Berlin)
03/96 – 05/97	Diplomarbeit in Theoretischer Physik (Arbeitsgruppe Halbleiter-Theorie, Universität Regensburg)
05/97	Diplom
11/91 – 05/97	Physikstudium an der Universität Regensburg

Zivildienst

07/90 – 10/91	Individuelle Schwerbehindertenbetreuung, Diakonie Regensburg

Schulausbildung

06/90	Abitur
09/85 – 06/90	Gymnasium Neutraubling (bei Regensburg)
09/81 – 07/85	Gymnasium Olching (bei München)
03/78 – 07/81	Grundschule Graßlfing (bei München)
09/77 – 03/78	Grundschule Großberg (bei Regensburg)

Berlin, 13. August 2000

Oliver Mayrock

Publications

- *Double-layered quantum dots in a magnetic field: Ground state and far-infrared response*
  O. Mayrock, S. A. Mikhailov, T. Darnhofer, and U. Rössler, Phys. Rev. B **56**, 15760 (1997).

- *Observability of the acoustic plasma mode in double-layered quantum dots*
  O. Mayrock, S. A. Mikhailov, O. Steffens, and U. Rössler, Physica E **1**, 232 (1997).

- *Weak localization of biexcitons in quantum wells*
  O. Mayrock, H.-J. Wünsche, F. Henneberger, C. Riva, V. A. Schweigert, and F. M. Peeters, Phys. Rev. B **60**, 5582 (1999).

- *Influence of internal polarization fields on the disorder broadening of excitons in (In,Ga)N/GaN quantum wells*
  O. Mayrock, H.-J. Wünsche, and F. Henneberger, O. Brandt, phys. stat. sol. (b), **216** (1999).

- *Optical properties of heavily doped GaN/(Al,Ga)N multiple quantum wells grown on 6H-SiC(0001) by reactive molecular beam epitaxy*
  A. Thamm, O. Brandt, A. Trampert, J. Ringling, K. H. Ploog, O. Mayrock, H.-J. Wünsche, and F. Henneberger, Phys. Rev. B **61**, 16025 (2000).

- *Polarization charge screening and indium surface segregation in (In,Ga)N/GaN single- and multiple quantum wells*
  O. Mayrock, H.-J. Wünsche, and F. Henneberger, Phys. Rev. B **62**, 16870 (2000).

Conference Contributions

- Jahrestagung der Deutschen Physikalischen Gesellschaft 1997, Münster, Germany

- 24th International Conference on the Physics of Semiconductors 1998, Jerusalem, Israel

- 3rd International Conference on Nitride Semiconductors 1999, Montpellier, France
- Jahrestagung der Deutschen Physikalischen Gesellschaft 2000, Regensburg, Germany
- International Workshop on Nitride Semiconductors 2000, Nagoya, Japan

Selbständigkeitserklärung

Hiermit erkläre ich, die vorliegende Arbeit selbständig ohne fremde Hilfe verfaßt zu haben und nur die angegebene Literatur und Hilfsmittel verwendet zu haben.

14. August 2000

Oliver Mayrock